Surface mass balance of the Ross Ice Shelf from stable water isotopes, ground penetrating radar, and back trajectory analyses

---

Marcus Arnold

Gateway Antarctica

College of Science

University of Canterbury

This thesis is submitted for the degree of Master of Antarctic Studies

October 2016

To my childhood dog, Buddy, whom I lost the day prior to moving to New Zealand to begin my career in polar science. I still think about you every day, big guy.

"A man who keeps company with glaciers comes to feel tolerably insignificant by and by. The Alps and the glaciers together are able to take every bit of conceit out of a man and reduce his self-importance to zero if he will only remain within the influence of their sublime presence long enough to give it a fair and reasonable chance to do its work"

– Mark Twain.

DECLARATION

This dissertation is the result of my own work and includes nothing, which is the outcome of work done in collaboration except where specifically indicated in the text. It has not been previously submitted, in part or whole, to any university of institution for any degree, diploma, or other qualification.

Signed: 

Date: 10th October, 2016.

Marcus Arnold

ABSTRACT

Precipitation in Antarctica, described by the surface mass balance (SMB), is the largest positive constituent of ice sheet mass balance, thus plays a key role in the Antarctic, hence global climate. Due to spatial and temporal scarcity of ground-based observations, there remain many unknowns about the precipitation regimes in Antarctica. This thesis investigates the temporal and spatial variability of SMB over a ~500km^2 area near the middle of the Ross Ice Shelf (RIS), and explores the climatic and non-climatic controls behind displayed variability.

Annual net accumulation was determined by means of analysing seasonal variations in stable isotopes $\delta^{18}O$ and $\delta^{2}H$ from a 16m firn core. A 32 year time series was derived at annual resolution, representing average annual net accumulation of ~220 $\pm$ 100mm water equivalent (w.e.) yr^{-1} – approximately double that of previous estimates. As the firn core was spatially limiting, the use of Ground Penetrating Radar (GPR) allowed for expanding the ground truth to a wider area.

~150km of GPR profiles were used to derive spatial variations in snow accumulation. Spatial variability was an order of magnitude smaller than temporal variability, and is likely controlled by active flow features on the ice shelf. These features can be traced back to the grounding line, and are likely preserved due to differential flow of the ice shelf. With temporal variability being far greater than spatial variability, an investigation into the climatic controls of precipitation was required.

To understand the climatic controls on temporal variations in net snow accumulation, an atmospheric back trajectory and cluster analysis was undertaken using the Hybrid Single Particle Lagrangian Integrated Trajectory (HYSPLIT) model. A total of 20 distinct synoptic pathways were identified, with pathways originating in Ross Sea accounting for the majority of precipitation on the RIS. I find that the frequency of Ross Sea air mass trajectories is modulated by the El Niño-Southern Oscillation, represented by the Southern Oscillation Index (SOI), and suggest that both the SOI and back trajectory analyses show potential to be used as proxies for accumulation in this region.

Together, these studies form the basis and justification for future work in this region. They show that the current estimates of snowfall on the RIS may be largely underestimated, which has important implications for the input parameters of numerical models simulating the future behaviour of the Ross Ice Shelf.

ACKNOWLEDGEMENTS

Since moving to New Zealand to embark on a career in polar science, the support that I've received has been astounding.

Specifically, I would first like to thank the benevolent Drs. Wolfgang Rack and Heather Purdie for their continuous support, teaching, and enthusiasm. Your passion and knowledge of glaciology coupled with your patience and willingness to provide feedback on chapters has been invaluable. Aside from your consistent academic support, you have been excellent friends and I look forward to future involvements together.

A huge thank you is owed to Prof. Travis Horton for his support and guidance throughout the stable isotope analysis. Your enthusiasm for the results and insight into stable isotope hydrology and spectroscopy has unquestionably enhanced my understanding on the topic.

I would like to thank Prof. Peyman Zawar-Reza and Dr. Marwan Katurji for their insight into the realm of meteorology and climate modelling, and specifically in helping me understand the precipitation regime in the Ross Sea region.

I am forever in debt to the entities that have enabled me to complete this research in the first place. I would like to thank the Christchurch City Council, the University of Canterbury Alumni foundation, and the New Zealand Antarctic Research Institute (NZARI) for their generous scholarship support. I would also like to thank Antarctica New Zealand for logistical support and Heritage Expeditions for enabling me to visit the Sub-Antarctic Islands.

Thank you to Nick Key and Justin Harrison for their help in preparing equipment for fieldwork. The band saw rig was incredible!

To the entire Ross Ice Shelf fieldwork team – you were a phenomenal group of people to work with, and even on the days where it was horrible weather and everyone was tired, you maintained high morale, which I am forever grateful for. A particular acknowledgement is owed to Prof. Christina Hulbe, as the PI for the Ross Ice Shelf project. Your 'behind the scenes' work that has gone into the project is greatly appreciated, and has not gone unnoticed.

Gateway Antarctica has been an extraordinary environment to work in. Thank you to all of my office mates here, who have been excellent friends and colleagues and provided a huge amount of support.

On a more personal note, I would like to acknowledge the over-and-above support from PhD candidate Christian Wild, for a) having to spend over a year at a desk next to mine,

b) aiding me with manifold meteorological problems, and c) being an overall great friend to me. I have enjoyed our various adventures into the amazing landscapes of New Zealand. Keep your ears stiff and beard fluffy, and my best wishes for the final stages of your PhD!

Dr. Kurt Joy has also provided an enormity of support through his magical editing abilities, GIS wizardry, helpful advice in poster design, useful academic and life coaching, and overall hilarity with just about any phrase.

Thank you to Dr. Oliver Marsh for your helpful advice for my academic work and spending the time to help me understand various aspects of my work.

To the staff of Gateway – Bryan, Ursula, Vicki, Daniella, Michelle R. F., Regina, and fellow students not aforementioned – Michelle R., Gemma, Andrea, Ephaphrus, Gabriela, Ekki & Rachel – you have all been excellent friends and colleagues, and made the good times great, and the hard times better!

To Fie, who has been the most supportive partner I could have ever wished for. Thank you for moving to the other side of the globe for me, sticking with me during the hard times, and providing immense emotional support. Thank you for consistently putting up with my science jargon, and your relentless love and support.

Finally, to my family. To Nick and Maddy, for not only being supportive siblings, but my best friends. I look forward to being in the same country as you both again. And to Mum and Dad – I could not have done any of this without your help, and I hope that this thesis, in some small way, serves as a token of my appreciation. I love you both.

CONTENTS

LIST OF TABLES

LIST OF FIGURES

LIST OF ABBREVIATIONS AND ACRONYMS

Accumulation and net accumulation are used synonymously and refer to a positive surface mass balance.

AIS	Antarctic Ice Sheet
AP	Antarctic Peninsula
AS	Amundsen Sea
ASL	Amundsen Sea Low
AWS	Automatic Weather Station
BS	Bellingshausen Sea
EAIS	East Antarctic Ice Sheet
ENSO	El Niño–Southern Oscillation
GMWL	Global Meteoric Water Line
GNSS	Global Navigation Satellite System
GPR	Ground Penetrating Radar
Gt	Gigatonnes
HWDS2	Hot Water Drill Site 2
HYSPLIT	Hybrid Single Particle Lagrangian Integrated Trajectory
IoA	Index of Agreement
IPO	Interdecadal Pacific Oscillation
L	Low
L-A	Low Amundsen
L-BA	Low Bellingshausen/Amundsen
L-R	Low Ross
MEaSUREs	Making Earth System Data Records for Use in Research Environments
NOAA	National Oceanic and Atmospheric Administration
NZARI	New Zealand Antarctic Research Institute
R	Ridge
RACMO	Regional Climate Model (Antarctica)
RAS	Ross Ice Shelf Air Stream
RIGGS	Ross Ice Shelf Geophysical and Glaciological Survey
RIS	Ross Ice Shelf
RS	Ross Sea
SAM	Southern Annular Mode
SLAP	Standard Light Antarctic Precipitation
SLR	Sea Level Rise
SMB	Surface Mass Balance
SOI	Southern Oscillation Index
SWE	Snow Water Equivalent
TAMs	Transantarctic Mountains
TWT	Two Way Travel time
V-SMOW	Vienna Standard Mean Ocean Water
WAIS	West Antarctic Ice Sheet
Z	Zonal

LIST OF APPENDICES

1 INTRODUCTION

"If Antarctica were music it would be Mozart. Art, and it would be Michelangelo. Literature, and it would be Shakespeare. And yet, it is something even greater; the only place on earth that is still as it should be. May we never tame it." – Andrew Denton

Antarctica is a land of extremes. It is often referred to as the highest, driest, coldest, and windiest continent on Earth. The lowest known naturally occurring temperature at the Earth's surface, -89.2°C, was recorded at Vostok Station, winds of up to 327km/h have been recorded, much of the interior receives less than 25mm of precipitation per year, and the average elevation is over 2000m above sea level. Ice covers 98% of the Antarctic continent, has an average thickness of around 1.6km, and reaches well over 4km in its thickest parts. Antarctica holds 90% of the world's ice (70% of the world's surface freshwater) and with a volume of 27 million km^3, it is capable of raising sea levels by ~60m if it were all to melt (Lythe et al., 2001; Fretwell et al., 2013). In recent years there has been increasing evidence that the Antarctic Ice Sheet (AIS) is losing mass, thus contributing to sea level rise (Shepherd & Wingham, 2007; Rignot et al., 2008; Allison et al., 2009; Shepherd et al., 2012; Hanna et al., 2013; Martín-Español et al., 2016). The overall mass balance of Antarctica remains poorly constrained however, with a recent study also suggesting that Antarctica is gaining mass (Zwally et al., 2015). A large component of this ambiguity of Antarctic mass balance arises from uncertainty and interannual variations of its surface mass balance (SMB) (Wang et al., 2016).

The largest input to most glacier systems is from net snowfall accumulation, described by the SMB, with dynamic losses accounting for the largest output in Antarctica. Little is known about the overall SMB regime in Antarctica (Verfaillie et al., 2012); for example, ambiguity and temporal variability of SMB approximations have led to sea level rise contribution estimates from the Pine Island sector to vary by a factor of two (Thomas et al., 2004; Van den Broeke et al., 2006; Mayewski et al., 2009). There is uncertainty as to how the SMB has been responding, and will respond to a changing climate – the result of very few in-situ measurements and large spatiotemporal variability (Frezzotti et al., 2005). It is currently unknown if Antarctic SMB is increasing or decreasing, thus, whether or not it is contributing to, or offsetting current sea level rise (SLR). It has been suggested that for every 1°C of climate warming, snowfall will increase by 5% (Frieler et al., 2015), equivalent to a sea level fall of 0.3-0.8mm yr^{-1} (Cuffey & Paterson, 2010). It is unclear if this hypothesis will prove true; based on climate models, Previdi and Polvani (2016) and Lenaerts et al. (2016) have asserted the likelihood of increased Antarctic SMB by mid-century, whilst Fudge et al. (2016) provided empirical evidence that increased temperatures don't necessarily result in increased accumulation. There is currently little empirical data showing an increase in precipitation driven by anthropogenic climate change (Monaghan et al., 2006a), with year-to-year SMB variability attributable to strong natural variability (Bromwich et al., 2011). Further complicating is the fact that increased accumulation would lead to increased ice flow and thus dynamical losses (Winkelmann et al., 2012), and higher temperatures would lead to increased surface melt and runoff (Lenaerts et al., 2016), potentially offsetting any mass gain from increased accumulation.

As 5-6mm of equivalent sea level falls on Antarctica as snow every year (Church et al., 2001; Lenaerts et al., 2012), it is vital that Antarctic SMB evolution is understood in greater detail and confidence. Aside from the more temperate Antarctic Peninsula (AP), surface melt is negligible, as it generally refreezes in the subjacent firn layer (Lenaerts et al., 2012). Indeed, mid-summer temperatures will have to increase by 5°C to produce a significant amount of continent wide surface melt, an unrealistic scenario for the coming century (Cuffey & Paterson, 2010). With the knowledge that a warmer ocean could give rise to increased snowfall, increased basal ice shelf melting, and grounding line retreat, it seems reasonable to assume that the temperature of ocean waters will be the most important climatic variable controlling Antarctica for the near future. Given that ice shelves surround 75% of Antarctica's coastline, heavily modulate the flow of grounded ice, and are in direct contact

with the oceans, they in particular, are gateways for climate warming to reach the inner ice sheet. This gives rise to the overarching aim of this thesis: to investigate the spatiotemporal variability of net snow accumulation on the world's largest ice shelf – the Ross Ice Shelf (RIS).

1.1 Ice Sheet Mass Balance

The overall mass balance of glaciers and ice sheets is determined by examining the difference between inputs and outputs (Figure 1). In Antarctica, the major input is snowfall (Cuffey & Paterson, 2010) and the major output is basal ice shelf melting and ice discharge (calving) (Rignot et al., 2013), with calving accounting for up to 90% of Antarctic mass loss (Bennett & Glasser, 2011). Ice sheet mass balance, as described by Hagen and Reeh (2004) is expressed by equation 1.1.

$$\frac{\partial V}{\partial a} = M_a - M_m - M_c \mp M_b \qquad 1.1$$

where V = ice volume, a = one year, M_a = annual surface accumulation, M_m= the annual loss by glacial surface runoff, M_c = the annual loss from calving icebergs and M_b = the annual balance at the bottom (melting or freeze-on of ice).

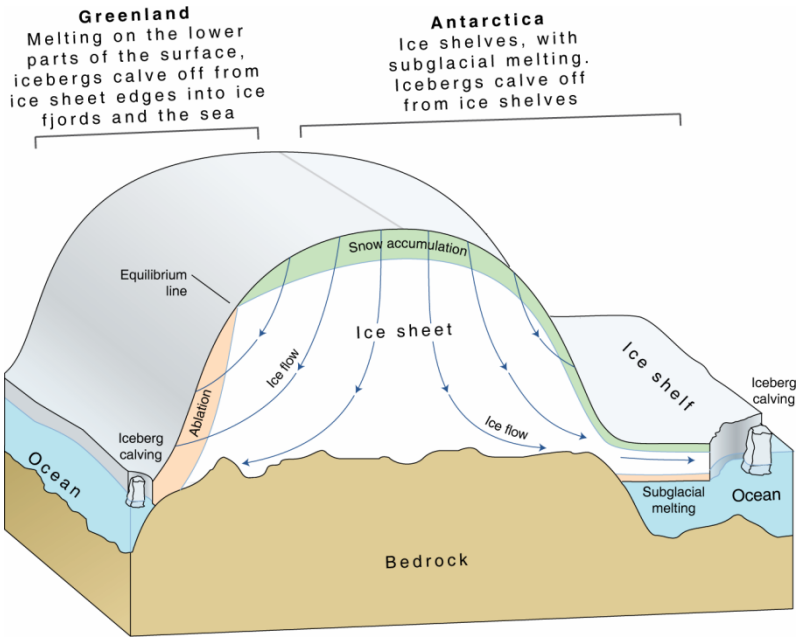

Figure 1: Schematic of ice sheet mass balance, showing input from snow accumulation and output from dynamic losses at the margin, as well as subglacial melting. Original figure from http://lima.nasa.gov/img/UNEP_icesheetcartoon.png. The right side of the figure represents Antarctic systems whilst the left represents Greenland, as the latter has no large ice shelves.

The magnitude of ice loss from Antarctica is poorly known, with estimates ranging from -139 gigatonnes (Gt) yr^{-1} to 42 Gt yr^{-1} (Shepherd & Wingham, 2007), with most losses coming from the AP and the West Antarctic Ice Sheet (WAIS) (Rignot et al., 2004; Thomas et al., 2004; Rignot et al., 2008) . To offset mass loss, the ice sheets gain mass from snowfall, yet the overall mass balance for Antarctica remains negative. The most recent estimation at the time of writing suggests a net mass balance of -84 ± 22 Gt yr^{-1} for the AIS (Martín-Español et al., 2016), and the general scientific consensus is in agreement of a negative mass balance (Figure 2).

There are three main methods for measuring ice sheet mass balance (Rignot, 2011):

I. The mass budget method, where perimeter losses are compared with interior snow accumulation
II. The gravity method, where time series of time variable gravity data is used to deduce mass changes (excludes ice shelves)
III. The altimetry method, where repeated altimetry surveys across the ice sheet are used to determine volume, thus mass, changes.

No single method is preferred above others, and all methods yield different results. Consequently, a combination of methods is usually advantageous.

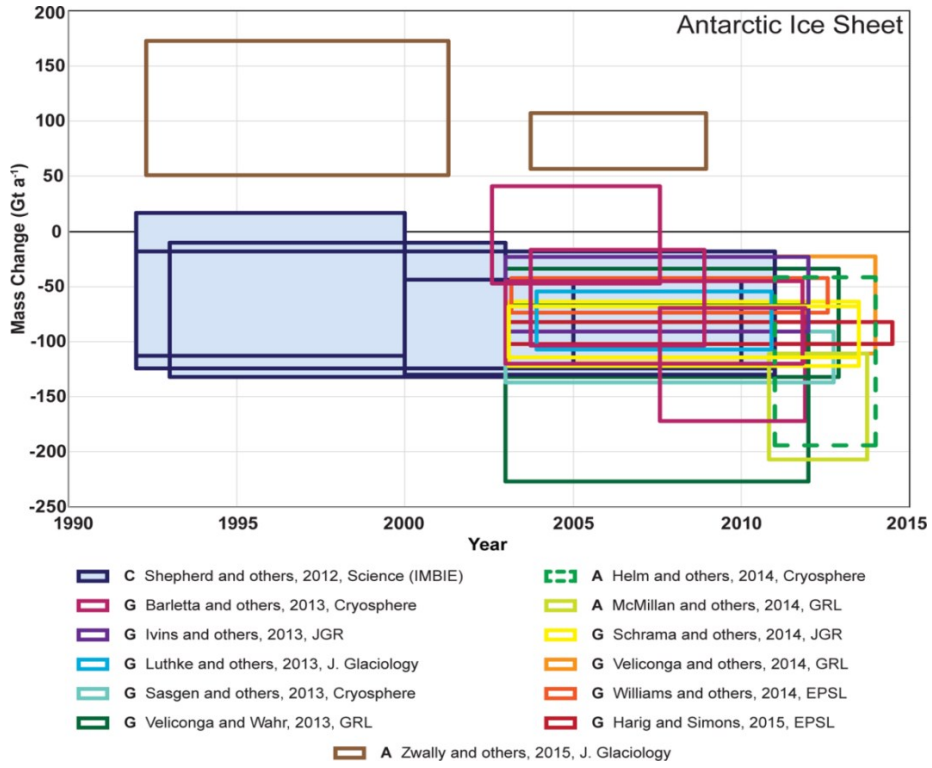

Figure 2: Ice sheet mass balance estimates from different studies (Scambos & Shuman, 2016).

1.1.1 Surface Mass Balance (SMB)

The sum of gains and losses from the end of the summer melt season to the end of the next is known as surface mass balance (Meier, 1962). Precipitation from clouds, formation of hoarfrost, sublimation, surface melting and runoff, wind scouring, snow drift deposition, and surface cloud (i.e. 'diamond dust') all contribute to water transfer across Antarctica (Vaughan et al., 1999a). Individual components are difficult to measure, but the aggregate of them all is measureable by various techniques. The components of surface mass balance have been explained in detail by Van den Broeke et al. (2004) are represented by:

$$Surface\ Mass\ Balance = PR + SU_s + ME + ER_{ds} + SU_{ds} \qquad 1.2$$

Where:

$PR =$ solid precipitation.

SU_s = surface sublimation/deposition. In summer, the surface sublimation may remove a large amount of the winter snow deposition, and may remove up to 15% of annual snow across the entire ice sheet (Van den Broeke, 1997; Van den Broeke et al., 2004).

ME = Surface melt. Surface melt usually occurs in summer around the fringes of the continent, although melt has been observed for longer periods in the Antarctic Peninsula.

ER_{ds} = processes related to drifting snow (usually erosion/deposition due to divergence or convergence of the horizontal snowdrift transport). If the friction velocity exceeds a threshold value, snow particles are lifted from the surface and suspended in the air. For the Antarctic ice sheet as a whole, drifting snow is likely to be of little significance, with estimates that sublimation of drifting snow (SU_{ds}, next paragraph) is two orders of magnitude more important (Déry & Yau, 2002; Van den Broeke et al., 2004).

SU_{ds} = sublimation of drifting snow particles in a column extending from the surface to the top of the drifting snow layer. This occurs in conditions of under saturated air with respect to the ice. When snow is airborne more of its surface area is exposed which makes drifting snow sublimation more effective than surface sublimation. In a steady state scenario the SU_{ds} represents a definite negative balance as the sublimated mass is resupplied from the surface by particles entering the suspension layer. Despite previous estimates (Déry & Yau, 2002), Van den Broeke et al. (2004) found that the effect of SU_{ds} was similar to ER_{ds}, although there was considerable uncertainty in their estimates. Lenaerts et al. (2012) suggest that the main process of ablation is SU_{ds}, supporting Déry and Yau (2002).

All terms are negative when they remove mass from the surface and positive when they add mass. As with most remote and harsh locations, Antarctica is a difficult continent to measure SMB parameters separately – precipitation gauges are not very effective in high wind speed conditions and typically undercatch by up to 50% (Fassnacht, 2004) and conversely, drifting snow may enter the gauges (Bromwich, 1988; Van den Broeke et al., 2004). Currently, it is difficult to measure snowfall in real-time without disturbing the natural patters of snowdrift, and natural processes of compaction (Eisen et al., 2008). In this regard, snow pillows show potential measure snowfall in real-time, but remain problematic during icing, frosting and crusting events (Engeset et al., 2000), and are not in wide use. The spatial and temporal variability means that interpolations of point measurements are not easily or necessarily accurately done, meaning that other techniques must be employed to overcome these limitations (Eisen et al., 2008). The continent also covers an area of 14,000,000 largely inaccessible square kilometres, making spatially comprehensive measurements logistically impossible. Given this difficulty, most SMB measurements are obtained with stakes or firn cores to yield a year-to-year picture (Van den Broeke et al., 2004). The difficulty associated with obtaining SMB measurements in Antarctica has led to a lack of spatially and temporally coherent observations, and the majority of SMB measurements have been taken relatively close to the coast where spatial variability is high. For example, net accumulation derived from 2 cores 18km apart in Wilkes Land (East Antarctica) differed by a factor of two (Morgan et al., 1991; van Lipzig et al., 2002). There is no single method for measuring surface mass balance and its components, as each method differs in temporal and spatial scales as well as resolutions (Eisen et al., 2008), as is shown in figure 3 and figure 4.

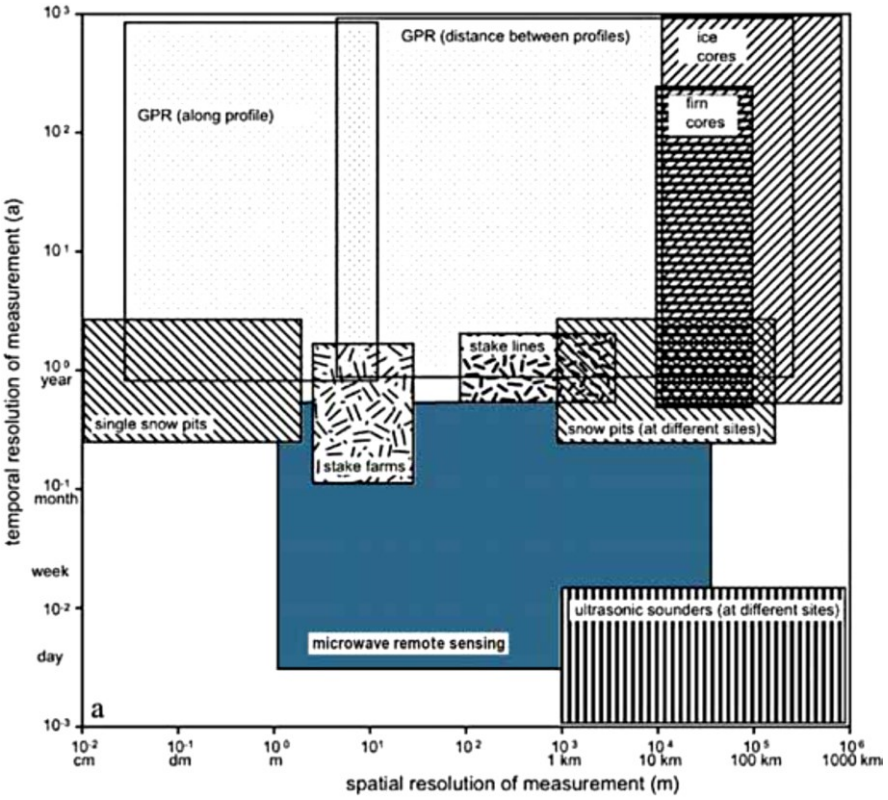

Figure 3: Spatial Resolution of different methods of accumulation measurements. Original image from Eisen et al. (2008) that has been modified to include microwave remote sensing by Linow (2011).

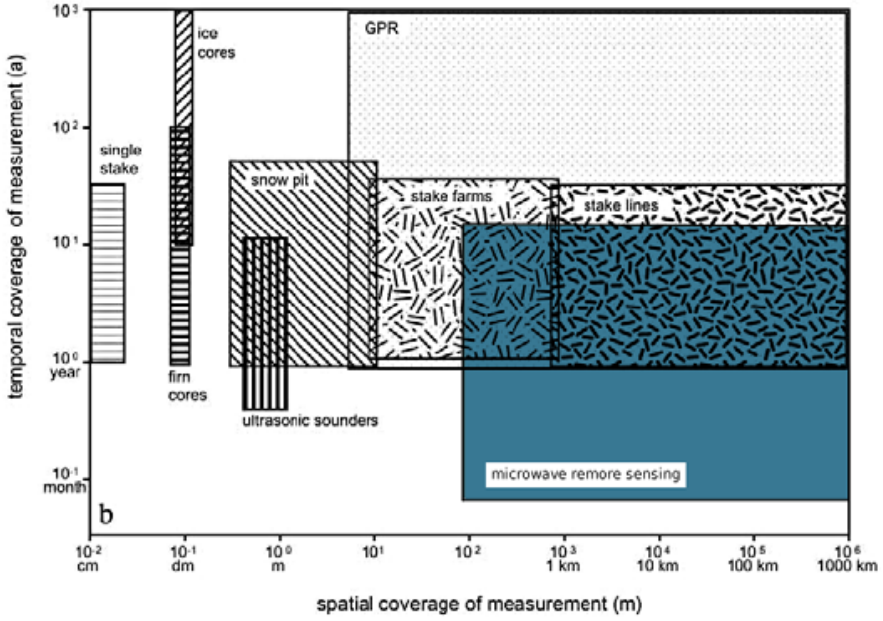

Figure 4: Spatial Coverage of different methods of accumulation measurements. Original image from Eisen et al. (2008) that has been modified to include microwave remote sensing by Linow (2011).

Snow accumulation is most commonly represented as mass, usually in the form of snow water equivalent (SWE, or mm w.e.), g cm^{-2} or kg m^{-2} and is expressed on a yearly scale (yr^{-1}). These measurements provide more information than the snow height alone, which is not useful unless the density is known. It can be thought of as the depth of water that would result if all the snow in a snowpack melted instantaneously. While snow density is covered in detail in section 3.2.1, equations 1.3 and 1.4 will serve as a primer for understanding the snow depth and density relationship:

$$Snow\ Density = \left[\frac{snow\ weight\ (g)}{snow\ volume\ (cm^3)}\right] \times 1000\ (kg\ m^3) \qquad 1.3$$

$$Snow\ Water\ Equivalent\ (SWE) = Depth\ \times Density \qquad 1.4$$

For a comprehensive review of methods to measure snow accumulation in Antarctica, refer to Eisen et al. (2008)

Compilations provide an excellent overview of the spatial and temporal extent of in-situ SMB measurements. These compilations often provide the basis for the calibration of atmospheric models, which produce accumulation maps. Ultimately, this leads to similar errors among all maps (Arthern et al., 2006), and subsequently, identifying the errors is difficult as the accuracy of these maps is often determined by comparing one map to another and often, models will share the same bias (Genthon & Krinner, 2001; Arthern et al., 2006). Conversely, if model disagreements are present, it provides the basis for determining regions where additional ground truth measurements may be required.

Favier et al. (2013) presented an updated surface mass balance data set for the whole Antarctic continent. The data includes the compilation from Vaughan et al. (1999a) as well as additional inclusions from more recent years. All data and the locations are shown in Figure 5. Metadata for each measurement is provided, allowing the end user to filter out any results.

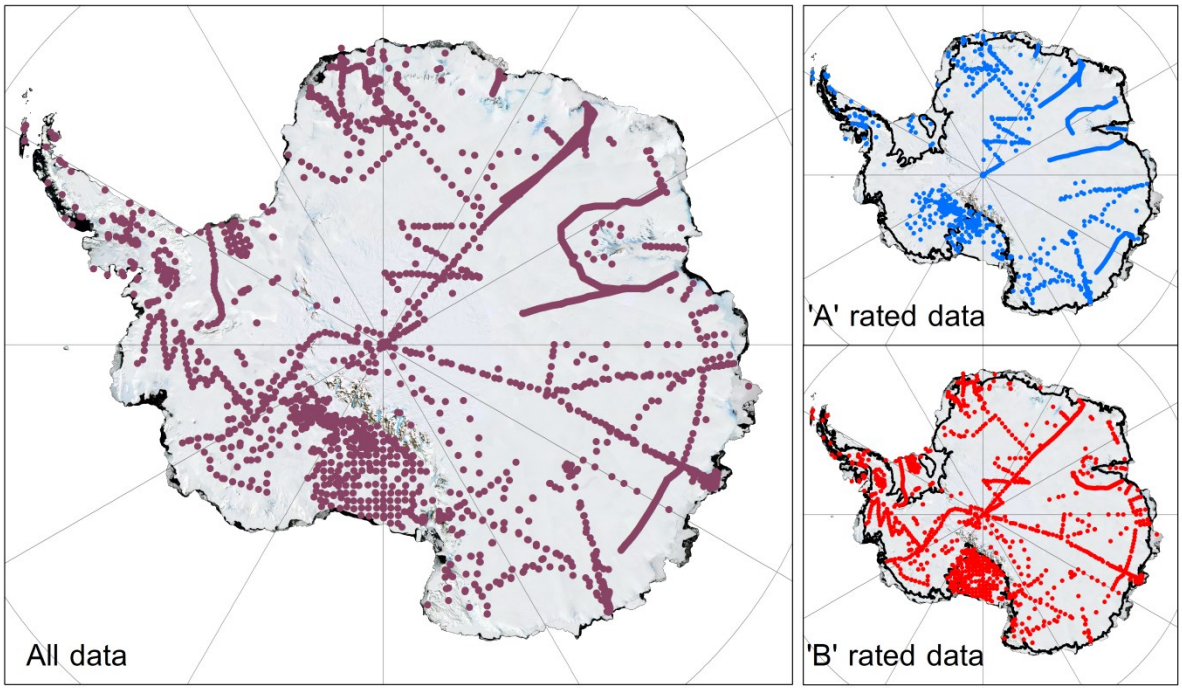

Figure 5: Visual representation of the surface mass balance compilation from Favier et al. (2013) showing on the left) the entire data set and on the right) locations of reliable field data (A rated data, top), and unreliable data (B rated data bottom). The data are quality controlled, regularly updated, and freely available online in CSV Format.

As the SMB represents the largest input of mass in Antarctica, it is imperative to estimate its magnitude accurately to meaningfully assess overall ice sheet mass balance. Many projections of the mass balance are based on the input-output (mass budget) method where input (SMB) and output (glacial dynamics) are modelled separately (Agosta et al., 2015). The uncertainty associated with this method is equal to the sum of uncertainties of input and output estimates which can be of the same order of magnitude as the mass change itself (Agosta et al., 2015). There has been little work that has linked the interactions of surface mass balance and ice dynamics, ultimately leading to uncertainty in estimates of sea level rise contributions (Ritz et al., 2015). Nevertheless, the overall SMB for Antarctica (including ice shelves) is estimated at 2418 ±181Gt yr^{-1} (Lenaerts et al., 2012). However, different studies have yielded different estimates as shown in Table 1.

Table 1: Snow accumulation over the Antarctic grounded ice

Source	Method	Accumulation (Gt/a)
Vaughan et al. (1999a)	interpolated field data	1811
Giovinetto and Zwally (2000)	interpolated field data	1883
Huybrechts et al. (2000)	interpolated field data	1924
Arthern et al. (2006)	passive microwave, field data	1768
Monaghan et al. (2006b)	climate model	1475-2331
Van de Berg et al. (2006)	climate model	2076
IPCC [2013, 13SM, pg. 5]	mean and standard deviation	1923
Turner et al. (1999)	ECMWF reanalysis	2106*
Lenaerts et al. (2012)	climate model	1983 (2418*)
Rignot et al. (2008)	climate model	2055
Van Wessem et al. (2014)	climate model	1793**

* Denotes accumulation across the grounded ice sheet and the ice shelves

** Denotes accumulation across the grounded ice sheet exclusive of the Antarctic Peninsula

The sources of precipitation across the continent vary greatly. Coastal sites generally receive precipitation from frontal cyclonic systems, whilst further inland on the plateau most precipitation is in the form of small ice crystals from isolated cloud, or even clear sky precipitation (i.e. 'diamond dust') (King & Turner, 1997). The areas with the greatest net accumulation include western parts of the Antarctic Peninsula (>1500mm w.e. yr^{-1}) and coastal West Antarctica (>1000mm w.e. yr^{-1}). Sections of coastal East Antarctica are estimated to receive ~1000mm w.e. yr^{-1}, whilst much of the interior ice sheets receives <25mm w.e. yr^{-1} (Lenaerts et al., 2012). Figure 6 shows the overall surface mass balance regime of Antarctica.

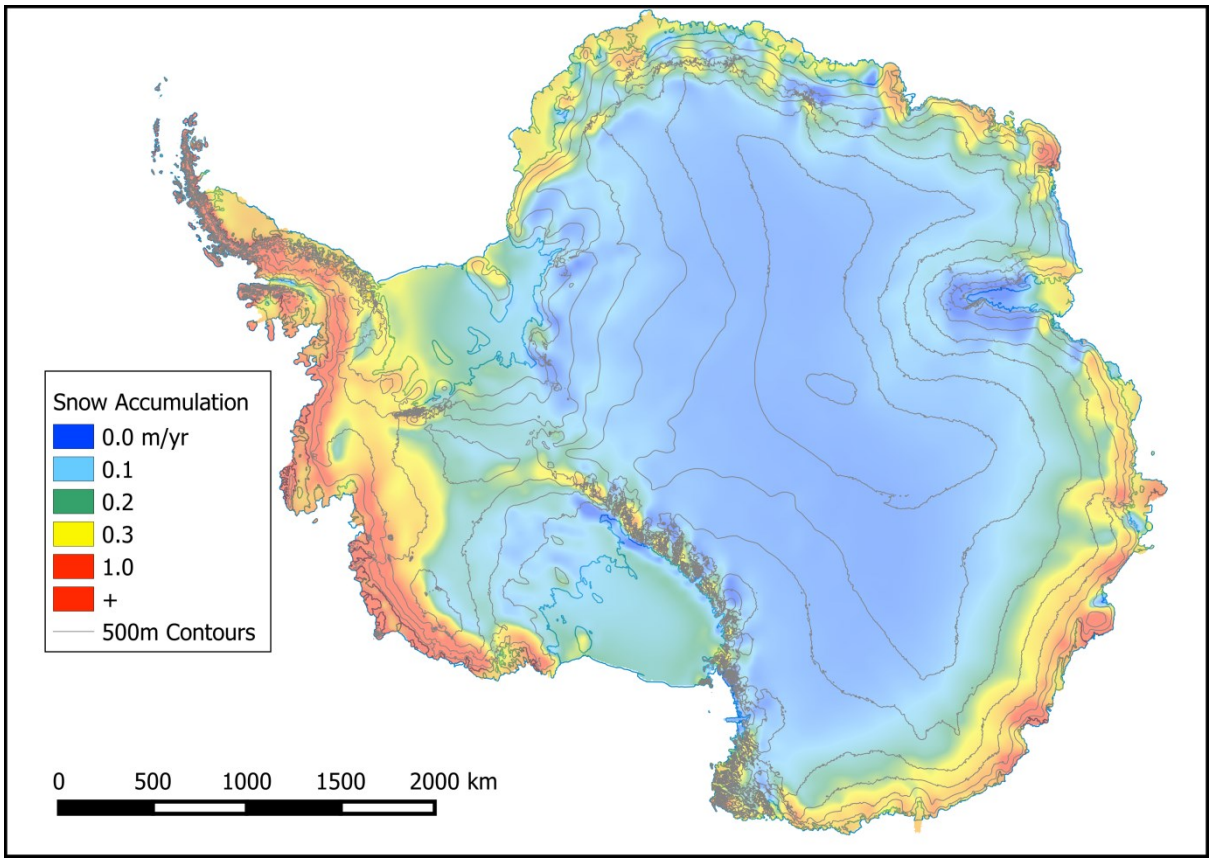

Figure 6: Snow accumulation across Antarctica. From Van de Berg et al., (2006), and produced with Quantarctica.

1.2 Ice Shelves

Antarctic ice shelves have undergone widespread thinning and retreat in response to atmospheric and oceanic forcing, and the importance of surface processes on ice shelves has recently been highlighted (Trusel et al., 2015). Up to 74% of ice discharged from the AIS passes through ice shelves (Vaughan et al., 2013), and the future dynamics of the AIS is strongly influenced by ice shelf behaviour (Pollard et al., 2015; DeConto & Pollard, 2016). In order to predict the future dynamics of ice shelves, it is necessary to understand their past and present state and understand the physical processes that link the climate to ice shelf stability and mass balance (Verfaillie et al., 2012).

Much of the WAIS is marine based, with the Bentley subglacial trench resting almost 2500m below sea level. This is problematic, as it is far more likely that an ice sheet resting on a bed below sea level will undergo rapid changes than one lying on a bed above sea level (Hughes, 1981; Rignot et al., 2004; Schoof, 2007; Joughin et al., 2012) . Mercer (1978) suggested that the WAIS was susceptible to a rapid collapse stating that "a major disaster – a rapid 5m rise in sea level, caused by the deglaciation of West Antarctica – may be imminent" (p. 321),

and that a "deglaciation of West Antarctica would probably be the first disastrous result of continued fossil fuel consumption" (p. 328).

Mercer (1978) also stated that "one of the warning signs that a dangerous warming trend is under way in Antarctica will be the breakup of ice shelves on both coasts of the Antarctic Peninsula" (p.324), starting with the northernmost and extending gradually southward. Mercer's predictions are starting to be realised, with around 20% of ice shelves on the Antarctic Peninsula having collapsed since the 1970's (Kuipers Munneke et al., 2013, 2014). The disintegration of an ice shelf does not directly contribute to sea level rise, as the ice shelf is already floating, thus displacing, water in the ocean. Ice shelves that are grounded at the sides, on islands or high points on the bed exert drag on the ice, increasing the resistance of the system to flow - without the ice shelf, unrestrained flow of ice from the ice sheet is permitted. For example, when the Larsen B Ice Shelf (Antarctic Peninsula) disintegrated, the velocity of some of the tributary glaciers increased eightfold (Rignot et al., 2004).

The Ross Ice Shelf is the world largest ice shelf, at nearly 520,000 km^2, roughly the size of France, or a quarter of the surface area of Greenland. The existence of the RIS is governed by the inflow of ice from the East and West Antarctic ice sheets, addition of mass via basal freezing and snowfall on the surface (i.e. net snow accumulation). Given that surface melt and sublimation is negligible in the region, the addition of mass via snowfall is critically important as it contributes substantially to the mass balance of the ice shelf (Benn & Evans, 1998). Despite the known importance of the RIS, and indeed all ice shelves, (e.g. De Angelis & Skvarca, 2003; Rignot et al., 2004; Scambos et al., 2004; Naish et al., 2009; Pollard & DeConto, 2009; Pollard et al., 2015), little is known about its SMB regime. The RIS has disintegrated in the past, when planetary temperatures were up to 3°C warmer than present, and atmospheric CO_2 levels were at 400ppm. This disintegration likely influenced the collapse of the WAIS (Naish et al., 2009), which may have contributed up to 5m of sea level rise (Pollard & DeConto, 2009). The recent breach of 400ppm global atmospheric CO_2 (Ritter, 2015) has triggered discussions on the stability of the RIS in a warming globe. Further understanding of the surface processes on the RIS is imperative for accurate modelling of future ice shelf behaviour, and importantly, the stability of the WAIS.

The RIS is situated between 160°E and 150°W and 78°S and 85°S. It is bounded by the Transantarctic Mountains to the south and west, by Marie Byrd Land to the east and by the Ross Sea to the north (Bentley, 1984) (Figure 7). Resistance from the walls of the

embayment, ice rises, and longitudinal compression upstream exerts a back-pressure, restricting the flow of ice and providing stability to the grounded ice sheets. In a glaciological setting, the RIS region contains constituents of the EAIS, WAIS, ice streams, and the ice shelf itself. The combination of these glacial entities makes the RIS an ideal setting to investigate the SMB. The core site, Hot Water Drill Site 2 (HWDS2) is located at -80.683, 174.817, approximately 370 km from Scott Base (Figure 7).

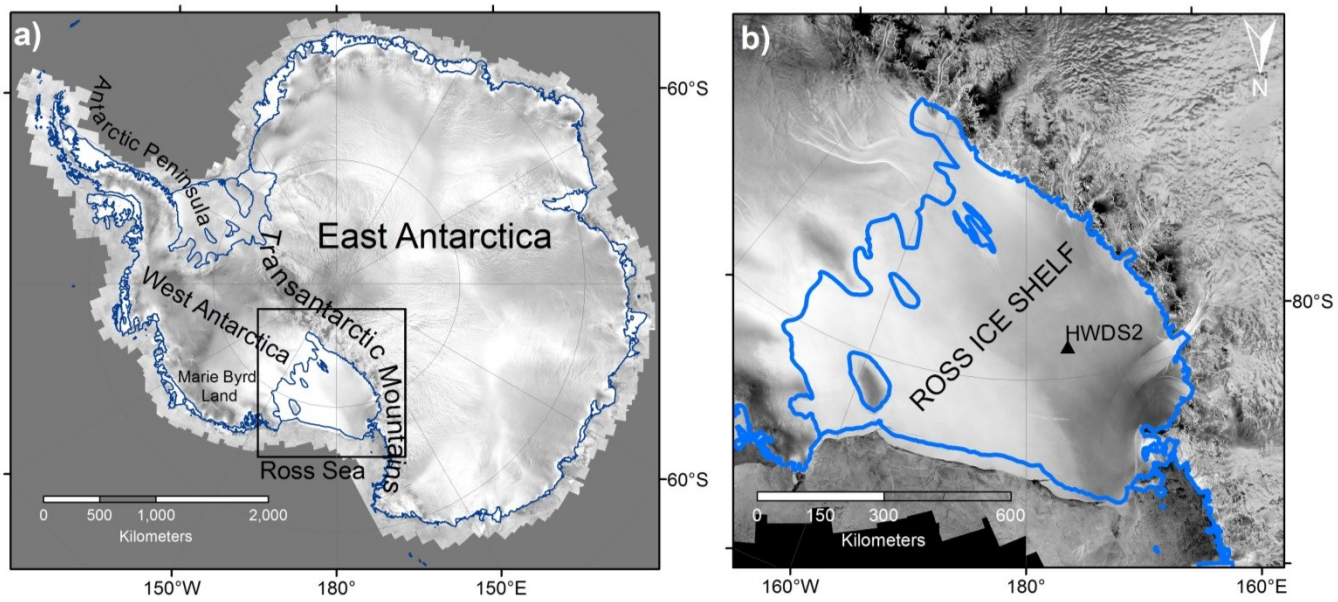

Figure 7: An annotated map of Antarctica showing extent of the Ross Ice Shelf (a) and the field camp location, HWDS2 (b).

1.3 Aims, objectives and structure of this thesis

The RIS and WAIS have collapsed in the past, yet the RIS remains largely unaffected by current global warming. With increased ocean and atmospheric warming, the question arises: what are the key processes that govern the stability and existence of the RIS? This research aims to quantify the magnitude and spatiotemporal variability of net snow accumulation at HWDS2, and understand the non-climatic and climatic controls behind the spatial and temporal variability, respectively. This research will contribute to the New Zealand Antarctic Research Institute (NZARI) programme 'The Vulnerability of the Ross Ice Shelf in a Warming Globe', helping to better understand the response of the RIS in a warming climate.

Specifically, this thesis aims to answer the following questions:

1. What is the temporal variability of accumulation near our study site, and can atmospheric models accurately predict snow accumulation in this area?

2. What is the spatial variability of accumulation near our study site, and what are the drivers?
3. What are the main climatic drivers of temporal variability, and how does synoptic variability influence snow accumulation?

These aims will be met by the following objectives:

1. The magnitude and temporal variability of net snow accumulation at HWDS2 will be determined by means of annual layer counting using a high-resolution stable isotope analysis of a 16m firn core, and the performance of climate models in the region will be numerically tested and compared to the empirical core derived accumulation rates.
2. The spatial variability of the net accumulation will be derived by means of ~150km of 500MHz ground penetrating radar profiles, using the firn core to date internal layers, and satellite imagery & ice shelf velocity data to understand non-climatic controls.
3. The main climatic drivers of temporal variability will be identified by means of an atmospheric back trajectory cluster analysis.

This thesis is structured to provide the reader with the best sense of continuity. Chapters 3, 4 and 5 are written in a quasi-academic paper style format. This introductory chapter has provided the foundation the reasons why this work is needed, thus introductions to each individual chapter are kept as short as possible, with the focus predominately on the methodology, underlying theory, results, and discussions. Similarly, summaries are kept as short as possible, with the major summary and synthesis presented in chapter 6. The overall structure is as follows:

Chapter One: "Introduction"

Chapter Two: "Antarctic Climatology & Site Description"

This chapter discusses the general characteristics and climatology of Antarctica and the Ross Ice Shelf and presents and introduction to decadal scale climate variability that may influence snowfall, such at the El Niño Southern Oscillation. The second part of this chapter describes the current state of research on surface mass balance of the Ross Ice Shelf, and presents current estimates from in-situ measurements and atmospheric models.

Chapter Three: "Temporal variability of net snow accumulation: annual layer counting by means of stable isotope analysis"

This chapter discusses the underlying theory of stable isotope variations in snow and ice, and the methods used to derive net accumulation. The results are also presented, and key findings discussed.

Chapter Four: "Spatial variability of snow accumulation by means of ground penetrating radar analysis"

This chapter presents the theory behind GPR use in snow and ice studies, and discusses the results from the GPR analysis and the drivers behind spatial variability of snow accumulation.

Chapter Five: "Climatological & meteorological controls on snow accumulation on the Ross Ice Shelf"

This chapter is focussed on an atmospheric back trajectory analysis using HYSPLIT, where the dominant synoptic pathways are identified, and related back to both decadal scale climatic variability and the accumulation rates derived in chapter three.

Chapter Six: "Synthesis, Conclusions, and Future Work"

2 ANTARCTIC CLIMATOLOGY & SITE DESCRIPTION

"*Having failed to demolish us by dogged persistence the gale tried new tactics on the evening of May 24, in the form of a series of Herculean gusts. As we learned afterwards, the momentary velocity of these doubtless approached 200 miles (320 km) per hour.*" – Douglas Mawson, at Cape Dension, 1913.

2.1 General Climatology of Antarctica & the Ross Ice Shelf

2.1.1 Antarctica

Antarctica is the Southern Hemisphere's heat sink, considerably controlling the circulation of the atmosphere at the mid and high latitudes (King & Turner, 1997). The continent itself is climatologically important in the Southern Hemisphere especially so, as the area surrounding the continent is largely devoid of high topography. The meridional thermal contrast between the warm subtropics and the cold Antarctic continent results in a highly baroclinic zone, and a strong pressure gradient to the north of Antarctica. If one were to examine a typical sea level pressure chart, a few striking features would be observed – the large circumpolar trough, the weak anticyclone over the continents' interior, and some departures from zonal symmetry within the circumpolar trough (King & Turner, 1997). The circumpolar trough is a region of low pressure (980-990hPa) around Antarctica between ~50°S and ~70°S caused by the high level of cyclonic activity around the continent, reflecting the lack of barriers to zonal flow

(King & Turner, 1997) and the interaction of cold continental and warm oceanic air masses. The circumpolar trough undergoes a Semi-Annular Oscillation (SAO), where it is deepest and closest to the continent in the weeks surrounding the equinoxes, when the temperature gradient between the mid and high latitudes is greatest (Van Loon, 1967). The cyclonic activity within the trough is the dominant mechanism for heat and moisture transfers from the mid to high latitudes. Due to the steep topography, most of the moisture is precipitated out along the coasts of the continent where, despite accounting for less than 40% of the total area, regions below 2000m elevation receive over 80% of Antarctic precipitation (Monaghan et al., 2006b). Within the circumpolar trough exists a few major regions of persistent low pressure, with the Amundsen Sea Low (ASL) being the most dominant (Turner et al., 2013), spanning the Bellingshausen, Amundsen and Ross Seas between ~65-70°S.

Persistent and strong winds are often the result of radiative heat loss at the ice sheet surface which regularly generate strong inversion conditions, where the lower atmosphere warms with increasing height above ground level (Phillpot & Zillman, 1970). Coupled with the sloping topography, the negative buoyancy of Antarctic surface air often results in the generation of large scale katabatic winds. As a result of their static stability, surface winds flow around barriers rather than over them (Coggins, 2013), giving rise to highly intense katabatic winds in the valleys of outlet glaciers and steep coastal regions (Parish, 1984). These can be exceptionally strong and persistent – at Cape Denison the mean annual wind speed during Mawson's expedition was ~20m s^{-1} (King & Turner, 1997). These katabatic winds are of particular importance with respect to snowfall in Antarctica as they are able to transport snow considerable distances from high on the Antarctic plateau through valleys onto ice shelves and coastal regions.

The Southern Annular Mode (SAM), also known as the Antarctic Oscillation, is the dominant mode of variability in the southern hemisphere between the subtropics and polar latitudes (Marshall, 2003), describing the periodic variability in the position and strength of the circumpolar pressure and wind patterns. The SAM is the leading empirical orthogonal function in surface pressure, geopotential height, surface temperature, zonal wind among many other atmospheric fields (Kidston et al., 2009). Gong and Wang (1999) defined the SAM by pressure differences as follows:

$$SAM = P^*_{40°S} - P^*_{65°S} \qquad 2.1$$

Where $P^*_{40°S}$ and $P^*_{65°S}$ are the normalised monthly zonal mean sea level pressure (MSLP) at 40°S and 65°S respectively. This basic method was modified by Marshall (2003), by simply using observational data opposed to global reanalysis data. Since the mid 1960's, the SAM index has experienced a positive trend, mostly during summer and autumn, indicative of a negative (positive) pressure trend at 65°S (45°S) (e.g. Figure 8, showing the SAM index from 1975-2016).

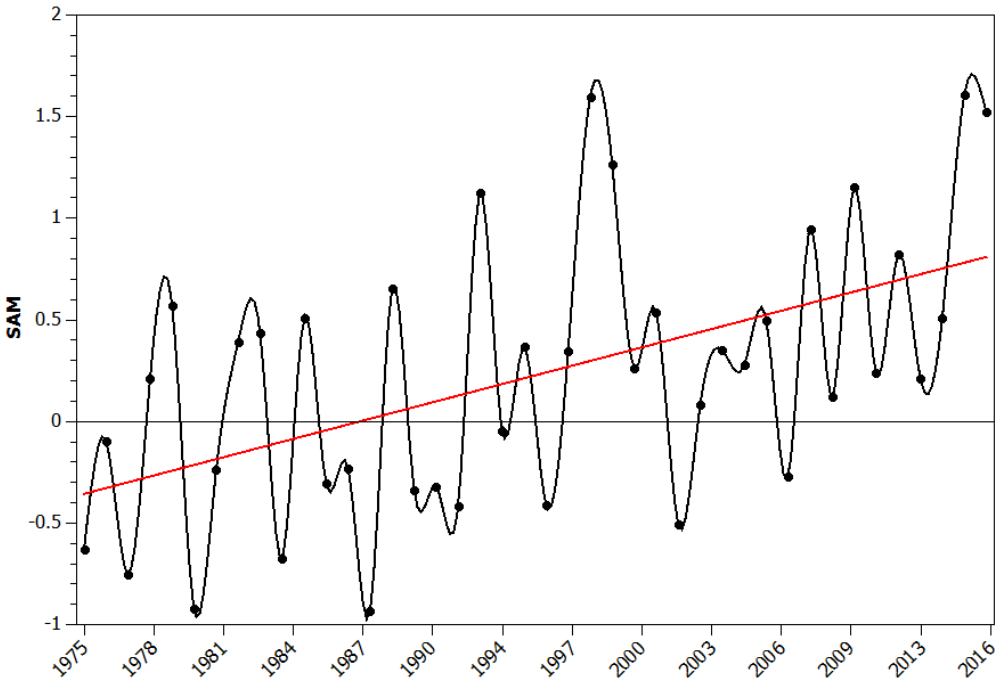

Figure 8: Annual average SAM index 1975-2016. Data downloaded from http://www.nerc-bas.ac.uk/icd/gjma/sam.html

A positive SAM index corresponds with a strong meridional pressure gradient, and vice versa for a negative SAM. A positive phase is usually accompanied by a southerly shift in strong, zonal westerlies and little exchange of moisture and heat from the mid latitudes, resulting in a cooling trend for much of interior Antarctica (Marshall, 2007). Coupled with the strengthening of the circumpolar winds in recent decades (Marshall et al., 2006), the positive SAM trend has led to a southerly shift in the circumpolar winds, resulting in a larger temperature gradient between the mid and high latitudes.

The 2-10year El Niño–Southern Oscillation (ENSO) is a coupled ocean-atmosphere mode, forced in the tropical Pacific, and its cycles are responsible for up to 30% of the interannual variability of Antarctic surface pressure (Turner, 2004). In normal tropical Pacific conditions, the upwelling of cold water off the coast of South America results in an east-west

temperature gradient, driving the easterly trade winds. During El Niño conditions, upwelling in the east is disrupted, causing warm oceanic temperature anomalies from South America across the Pacific, thus disturbing the typical atmospheric circulation. The ENSO teleconnection to the high latitudes is generally described by the poleward travel of Rossby wave trains, where the high latitude Pacific sector is the terminus position of the Pacific South American wave train (see Turner (2004) for a comprehensive review). ENSO variability can be explained by the Southern Oscillation Index (SOI), the normalised surface pressure difference between Tahiti and Darwin. During positive (negative) SOI periods, easterly tradewinds in the tropics are strengthened (weakened), reflecting the east-west shift of warm water in the Pacific Ocean. Positive (negative) SOI periods are characterised by La Niña (El Niño) conditions. ENSO teleconnections in Antarctica are mostly exhibited in the Ross, Amundsen, and Bellingshausen sectors in the form of pressure, surface temperature, sea ice, and wind anomalies (Turner, 2004). During strong La Niña events, the ASL has been known to deepen with increased cyclonicity in the region (Turner, 2004), directly affecting weather patterns on the RIS. In the western Ross Sea sector, La Niña events are typically associated with lower sea level pressure, cooler sea surface temperatures (SST's) and a warmer land surface temperature, and vice versa for El Niño years (Bertler et al., 2004; Bertler et al., 2006).

2.1.2 The Ross Ice Shelf

The RIS is climatologically unique, bordered on the west and south by the Transantarctic Mountains (TAMs), an impressive range with peaks far exceeding 4,000m. The Ross Sea sits to the north, and the gently sloping WAIS to the east. The RIS is devoid of any surface roughness, influencing the character of the katabatic wind regime. Katabatic winds that drain through outlet valleys in the TAMs and off the WAIS interact with synoptic scale systems and may flow for hundreds of kilometres, until they reach the Ross Sea (Bromwich et al., 1992). Due to the stable nature of the Antarctic boundary layer, when strong, cold (low level) flows encounter high topography they seldom overcome the barrier (Coggins et al., 2014). This is often the case along the TAMs (Figure 9), where persistent flow of cold air towards the TAMs results in a 'damming'. The dammed cold air increases the height of the inversion layer and produces a pressure gradient that is directed perpendicularly outwards from the barrier (Coggins, 2013). Once the gradient force forms equilibrium with the Coriolis force, a resultant geostrophic wind flows parallel to the barrier i.e. a 'barrier wind'. The combination

of the katabatic flow and barrier winds give rise to the RIS Air Stream (RAS, Figure 10), which has implications for the generation of precipitation (Bromwich, 1988) due to its association with cyclonic circulation in the Ross Sea. Further, katabatic winds coupled with synoptic conditions in Marie Byrd Land have been shown to be catalysts for mesocyclonogensis (Bromwich, 1991; Carrasco & Bromwich, 1994). For a comprehensive review of the RAS, refer to Coggins et al. (2014).

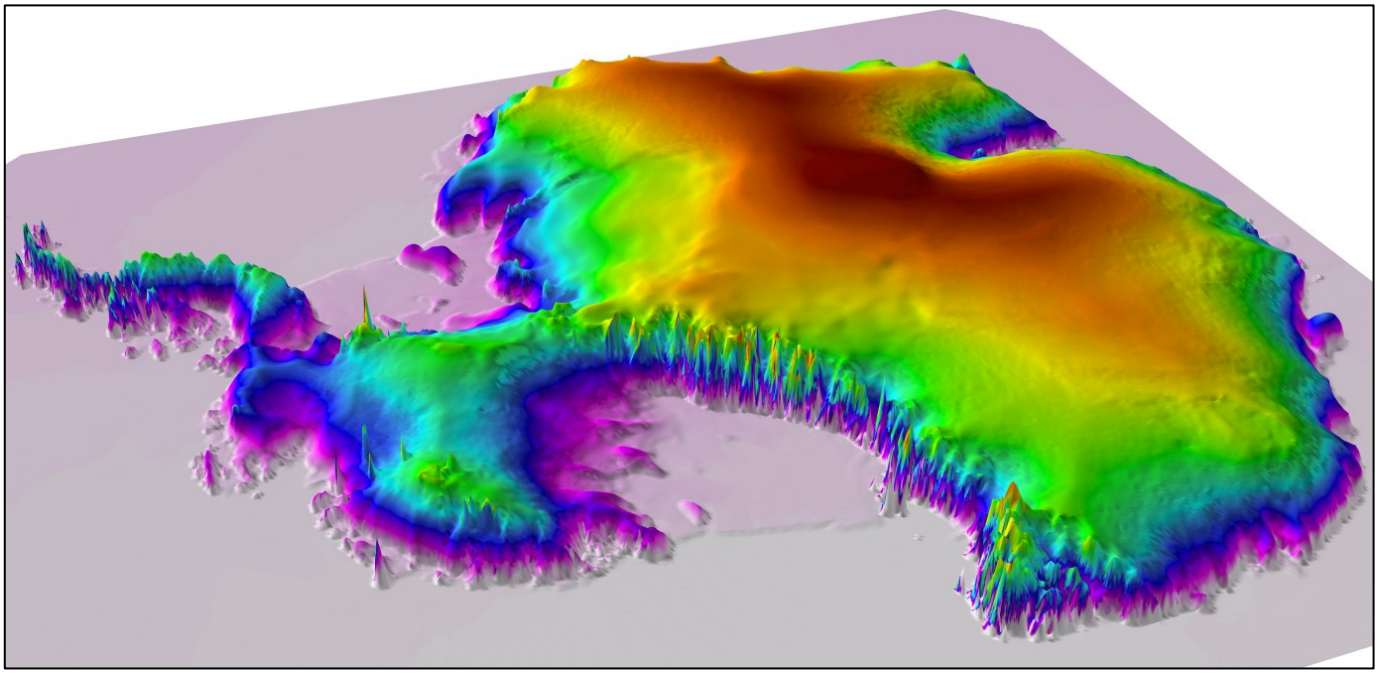

Figure 9: 3D visualisation of RAMP2 digital elevation model for Antarctica (vertical profile exaggerated). Figure shows the large barrier of the TAMs along the coast of the Ross Ice Shelf.

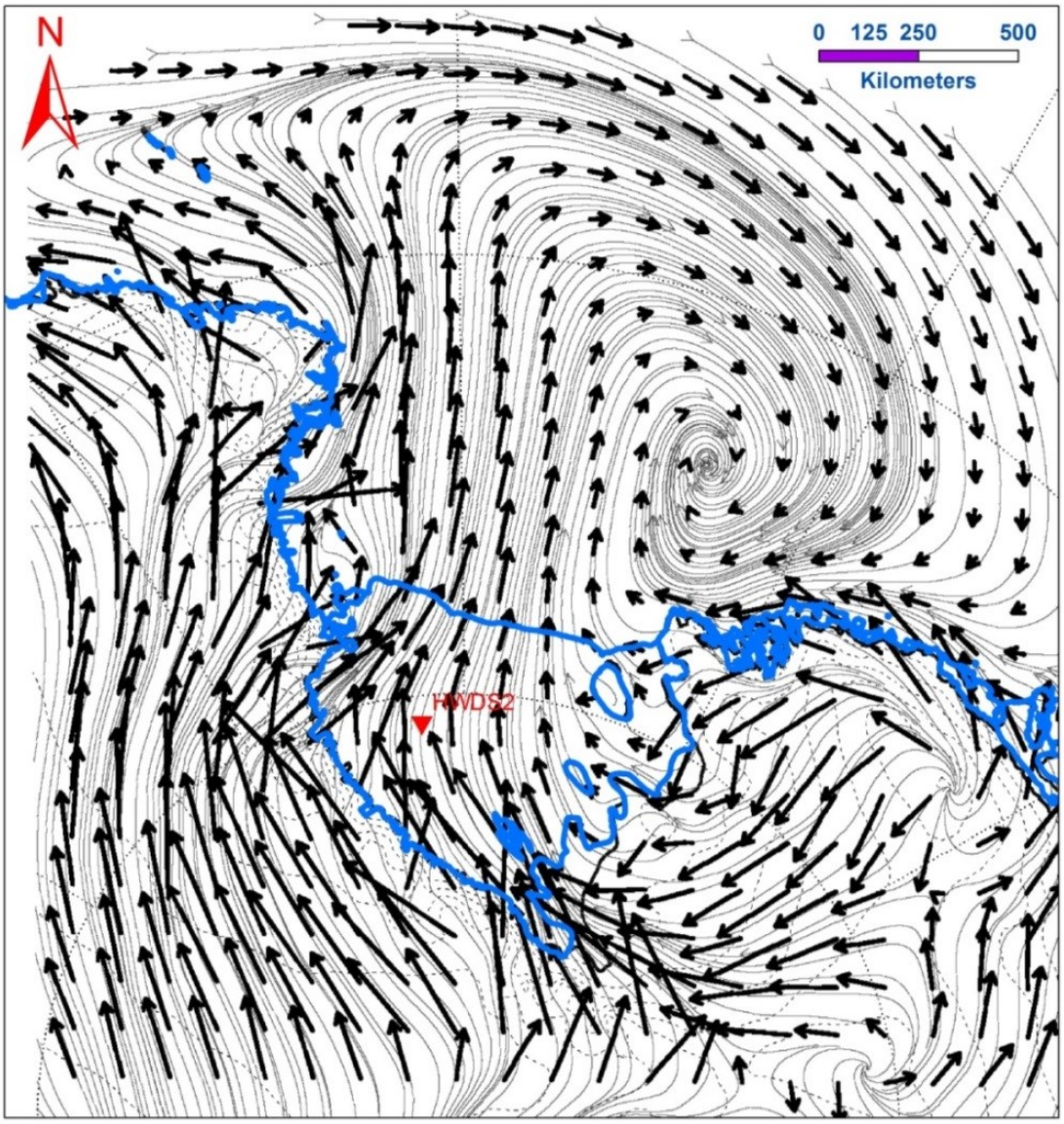

Figure 10: Typical airflow on the Ross Ice Shelf & surrounds. Mean wind vectors from the AMPS archive for the period Nov 2001 to Oct 2002. Modified from Parish et al. (2006) to show scale, continent/ice shelf outline and HWDS2 field location.

Temperatures on the RIS range from ~-65°C to 6°C, with typical summer (winter) temperatures of around ~-7°C (~-40°C) although these temperatures vary significantly both spatially and temporally (Costanza et al., 2016). Winter temperatures vary far more than summer, possibly due to increased cyclonicity (Costanza et al., 2016) (Figure 11). Pressure over the RIS typically ranges between 980-990hPa, with marked seasonal and multi-annual variations because of the effects of the ENSO and SAM oscillations, as well as more local

weather phenomenons. Maximum wind speeds range between 25-30m s^{-1}, with all maximum observations being recorded in the winter months (Costanza et al., 2016).

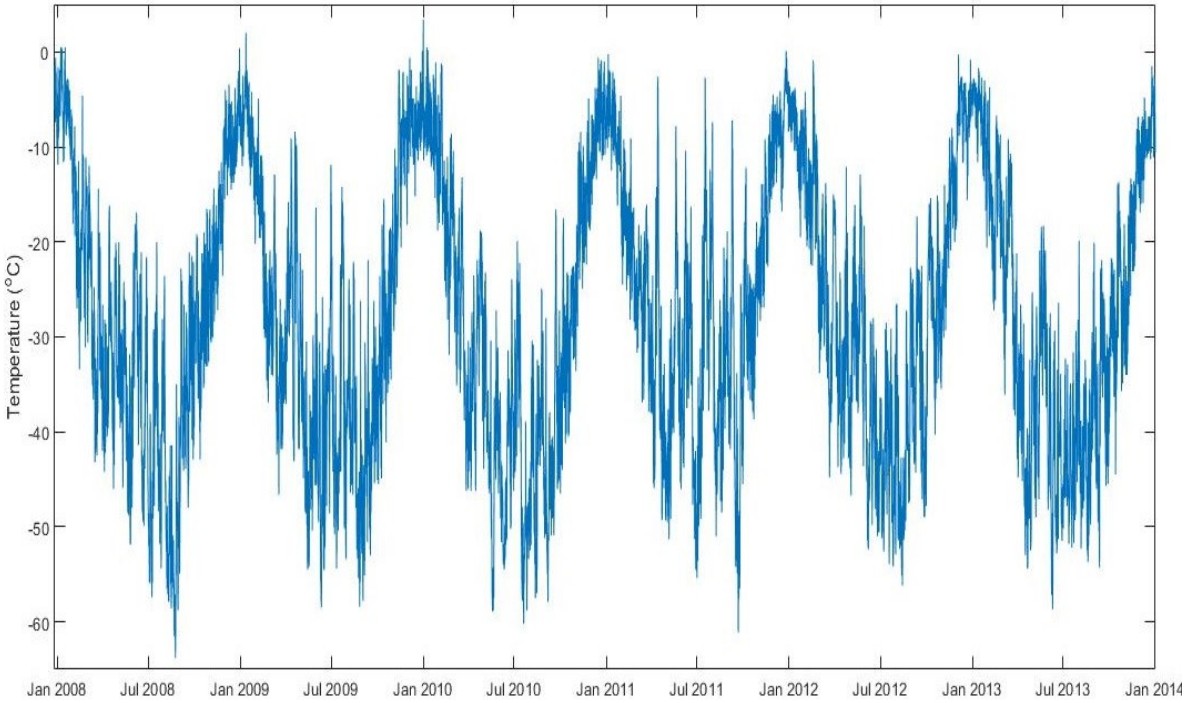

Figure 11: 3-hourly average temperatures from Jan 2008 to Jan 2014 from Gill AWS. Data supplied from Costanza et al. (2016).

Snowfall on the RIS occurs year round, with most accumulation occurring in discrete events, although there doesn't appear to be any dominant snowfall season/month (Figure 12). Precipitation events on the RIS are typically related to large-scale synoptic cyclones that are constrained by the surrounding topography. Sinclair et al. (2010) found that at the Gawn Ice Piedmont (near the Byrd Glacier that feeds the RIS), single storm events contributed to >60% of accumulation measured, including one storm that delivered 7% of the net accumulation in one day. The Ross Sea region is known as a centre for the formation of mesocyclones (Bromwich, 1991; Carrasco & Bromwich, 1994) which are defined as sub-synoptic scale low pressure systems (King & Turner, 1997). Mesocyclones occur on average once per week on the RIS, and are responsible for a significant proportion of snowfall (Carrasco & Bromwich, 1994). Rockey and Braaten (1995) suggest, for example, that over a third of snowfall at McMurdo Station is associated with mesocyclones. Due to their small horizontal scale, mesocyclones are difficult to monitor and predict (King & Turner, 1997). Recent studies have also demonstrated the importance of 'atmospheric rivers' on precipitation (Gorodetskaya et

al., 2014; Fudge et al., 2016), which may contribute a substantial amount of annual precipitation in a single event.

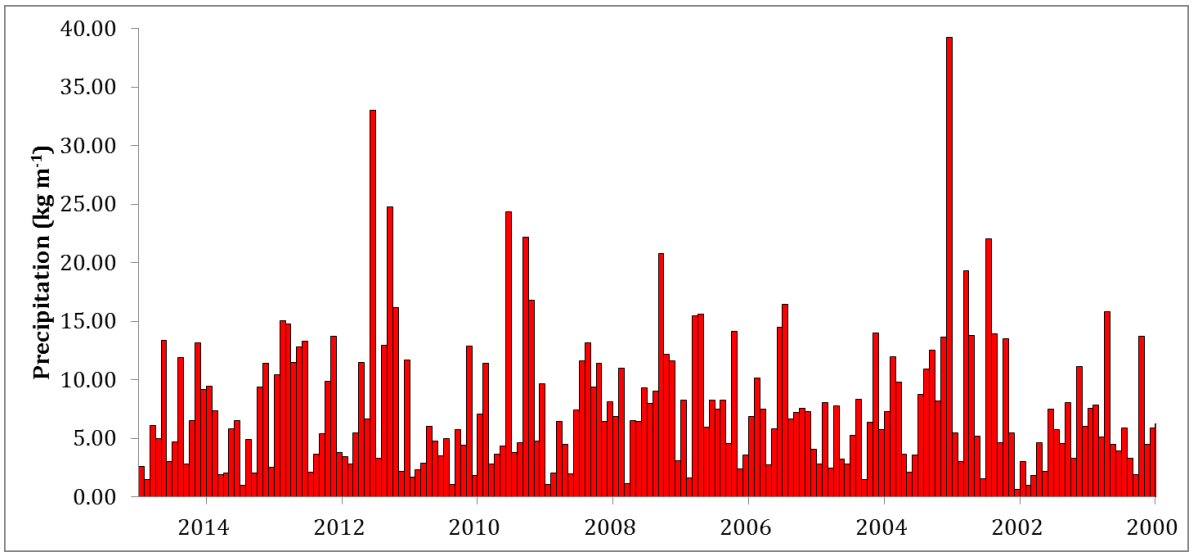

Figure 12: RACMO 2.3 monthly precipitation for HWDS2 2000-2015. Data supplied by Van Wessem et al. (2014). Most snowfall is concentrated in large, single events that can occur at any time in the year.

Both the ENSO and SAM have been found to have a marked effect on the precipitation regime of the Ross Sea region. Cohen et al. (2013) classified synoptic types for the Ross Sea region into 6 types: low Bellingshausen/Amundsen (L-BA), low (L), zonal (Z), low Ross (L-R), ridge (R), and low Amundsen (L-A) (Figure 13). In their study, they found that types L-BA, Z and L-R accounted for the largest amount of precipitation at Roosevelt Island, with L-R accounting for nearly 30% of the total precipitation (based on 1979-2011 NCEP reanalysis data). The SAM was negatively correlated with type L-R (cyclonic flow from the Ross Sea), and strongly positively correlated with type L-BA (cyclonic flow from the Amundsen & Bellingshausen Seas). The SOI was negatively correlated with type L-R and positively correlated with type L-BA. Although this is for Roosevelt Island, it is likely that that a similar regime is in place at HWDS2, as the precipitation source region is likely to be similar. Although significant annual variability exists, the SOI and SAM explained over 50% of the variability in L-BA and L-R in spring and ~40% in autumn. These factors could provide useful insights when interpreting a surface mass balance/precipitation record, and are discussed in further detail in chapter 5.

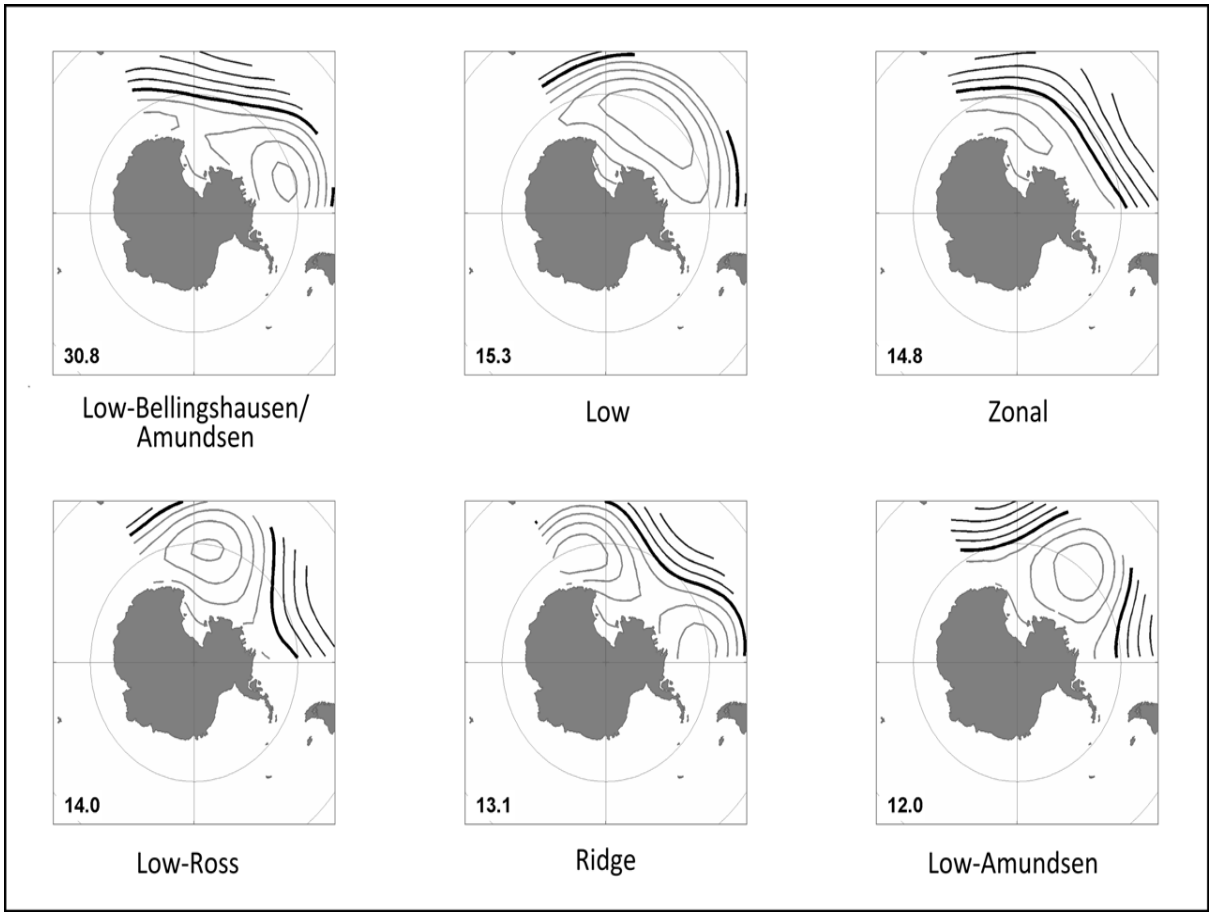

Figure 13: Synoptic types for the Ross Sea region, with the frequency (%) of occurrence shown on the lower left corner. Sourced from Cohen et al. (2013).

2.2 Surface Mass Balance on the Ross Ice Shelf

2.2.1 Estimates from In-Situ Studies

In situ studies during the period of 1935-1978 have SMB measurements from as little as 55mm w.e. yr^{-1} up to 285mm w.e. yr^{-1} at various locations across the Ross Ice Shelf (Wade, 1937; Nikolaeva, 1958; Vickers, 1958; Zumberge, 1958; Crary et al., 1962; Kotlyakov, 1966; Thomas et al., 1984). The first large scale surface mass balance study was published by Crary et al. (1962), who estimated the average accumulation over the ice shelf to be approximately 220mm w.e. yr^{-1} . In 1977, their results were found to be largely overestimated (Clausen & Dansgaard, 1977), although the different results are more likely a result of interannual variability. There was no data collected in vicinity of HWDS2, but the closest measurements obtained accumulation rates of ~165−175mm w.e. yr^{-1}. Later, Heap and Rundle (1964) published a study including accumulation measurements from over 2000 stakes and 31 snow pits from the northern edge of the ice shelf. It was found that the average accumulation was

144mm w.e. yr^{-1} between the years 1960–1962. Their study region was over 100km north of HWDS2, and again, measurements were taken over a period of 1-2 years, so are not temporally representative nor representative of conditions at HWDS2.

Between the years 1973−1978, a comprehensive analysis of surface accumulation was undertaken as part of the Ross Ice Shelf Geophysical and Glaciological Survey (hereafter 'RIGGS'). The stake method was used for this spatially comprehensive survey but most were only taken over a period of 1 year and therefore likely do not represent the long term averages. These data provide an estimate of accumulation at HWDS2 of ~110-125 mm w.e. yr^{-1}, while data from the Favier et al. (2013) compilation (Figure 5, chapter 1) provides a slightly higher estimate of accumulation, at ~125-160mm w.e. yr^{-1}. It must be stressed that these are estimates and whilst the general pattern of accumulation across the ice shelf is likely to hold true, the magnitudes are unlikely to be representative of any long-term averages. Nevertheless, figure 14 illustrates the results from the RIGGS project, and results from the Favier et al. (2013) compilation.

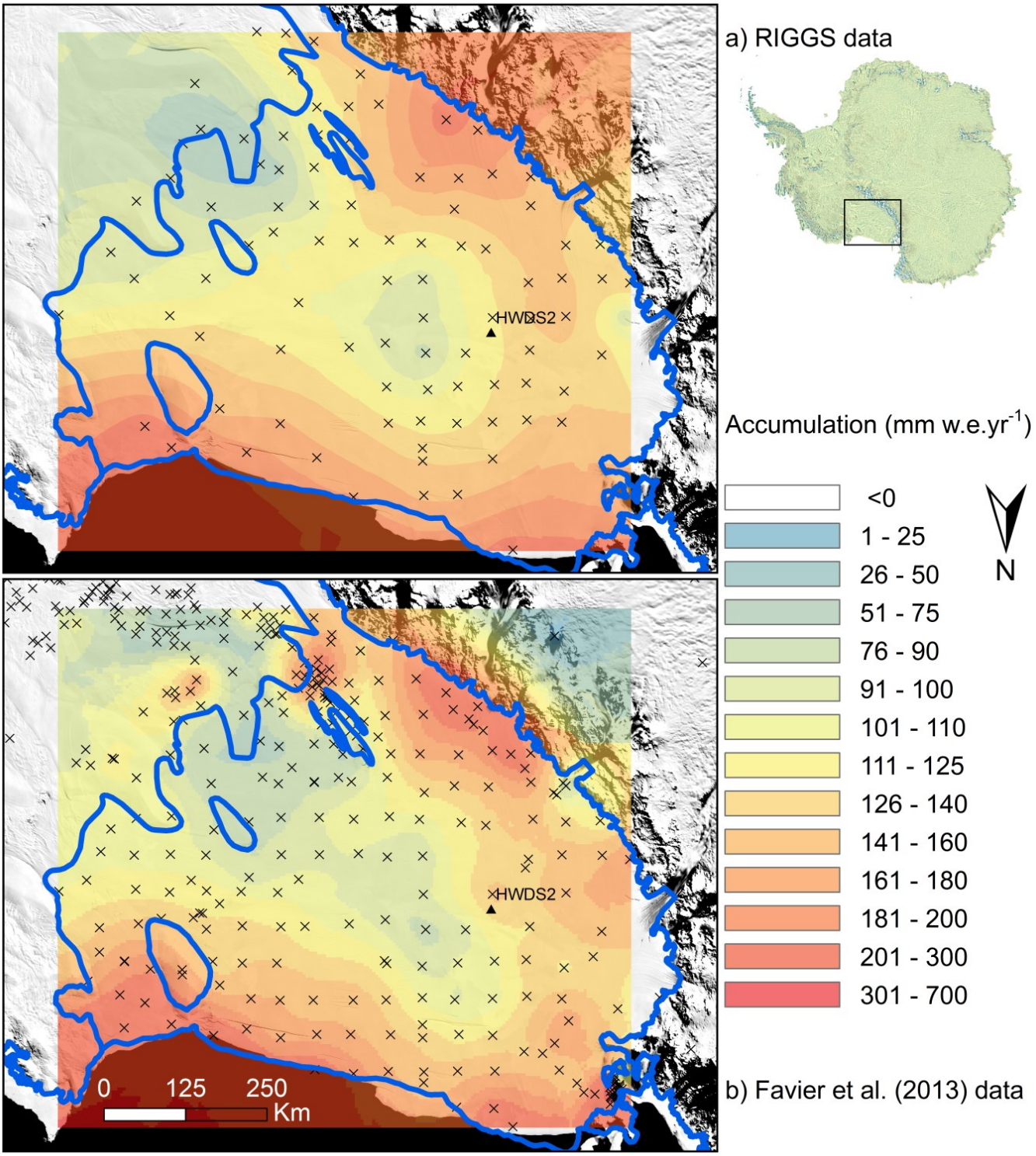

Figure 14: Accumulation map of the RIS created using the a) RIGGS and b) Favier et al. (2013) data, which were interpolated using a Bayesian Kriging method in ArcMap 10.2. Interpolation is overlaid on a MODIS mosaic.

Similar patterns between the two datasets are noted, with much of the interior of the ice shelf having very little accumulation compared to the coastal regions and the eastern side of the TAMs.

2.2.2 Estimates from Atmospheric Models

Simulated surface mass balance models usually include solid precipitation, sublimation, and snowmelt as a minimum (Van de Berg et al., 2006) and more detailed models include other parameters such as albedo, drifting snow and sublimation of drifting snow (Lenaerts et al., 2012). Unfortunately, most assessments suffer from large uncertainties due to the incomplete parameterizations of polar cloud microphysics and precipitation (Wang et al., 2016). Most atmospheric models use the regional climate model for Antarctica (RACMO/ANT) which is adapted for use over large ice sheets (Reijmer et al., 2005). RACMO usually combines the dynamics of HIRLAM (High Resolution Limited Area Model) which is comprehensively covered by Unden et al. (2002) and the physics of the European Centre for Medium Range Weather Forecasts (ECMWF) Integrated Forecast System (IFS) which is described in detail by Van Meijgaard et al. (2008). The models are usually forced by ERA-Interim reanalysis (Dee et al., 2011).

Van de Berg et al. (2006) produced an accumulation map using RACMO2.0/ANT (55km spatial resolution) that represented the period 1980-2004 and was in good agreement with 1900 in-situ measurements presented in the compilation by Vaughan et al. (1999a). Despite underestimating the SMB in interior East Antarctica, their model exceeded previous continent wide SMB estimates by as much as 15%, attributable to an overestimation of snowfall in coastal regions with few in-situ observations. Model output from Van de Berg et al. (2006) estimates snowfall at HWDS2 at approximately 140mm w.e. yr^{-1}.

Lenaerts et al. (2012) published a higher spatial resolution (27km) surface mass balance model based on RACMO2.1/ANT, which included physics of snowdrift and the most recent data from the ECMWF IFS. The model was forced by ERA-Interim reanalysis data that represented the period 1979-2010. Their model fit very well with approximately 750 in-situ surface mass balance measurements (R=0.88). The model captured spatial variability and the large gradient from the interior towards the coast quite well, but still had a negative bias for much of the interior (up to 55 ± 15% for elevations over 4000m).

The most recent update to the regional climate model, RACMO2.3, was developed by Van Wessem et al. (2014) and includes an upgrade in the ECMWF-IFS physics package. The upgrade includes changed to the cloud scheme and cloud microphysics and changes to the turbulent and radiative schemes. The changes that influenced surface mass balance included a parameterisation that allowed for cloud ice supersaturation which resulted in more cloud water being transported to the interior of the East Antarctic Plateau and decreased the negative bias in downward longwave radiation and surface temperature from RACMO2.0 (Van Wessem et al., 2014). The parameters that defined the formation of precipitation were also changed which led to a more efficient and quicker formation of precipitation in convective situations. Overall, RACMO2.3 shows a small change in total surface mass balance across Antarctica, but shows a better representation of the surface mass balance in East Antarctica and shows less bias than RACMO2.0 when compared to in-situ observations. However, the results from RACMO2.3 were still within the margin of error from RACMO2.1 (Lenaerts et al., 2012). Biases of up to 15% are still observed, but are drastically improved from RACMO2.1. For example, for regions above 4000m in East Antarctica the negative bias has reduced from 55 ± 15% to 10 ± 10%. At present, RACMO2.3 performs the best at capturing the absolute magnitudes of snow accumulation over Antarctica (Wang et al., 2016).

The published spatial resolution of the accumulation maps presented from these models makes it difficult to interpret the actual output from these models unless data is supplied by the authors. Van Wessem et al. (2014) have kindly supplied the RACMO2.3 data, which were extracted in MATLAB and then processed in the same method as the RIGGS and Favier et al. (2013) data sets, providing a much higher resolution output for the RIS. The results are shown in figure 15.

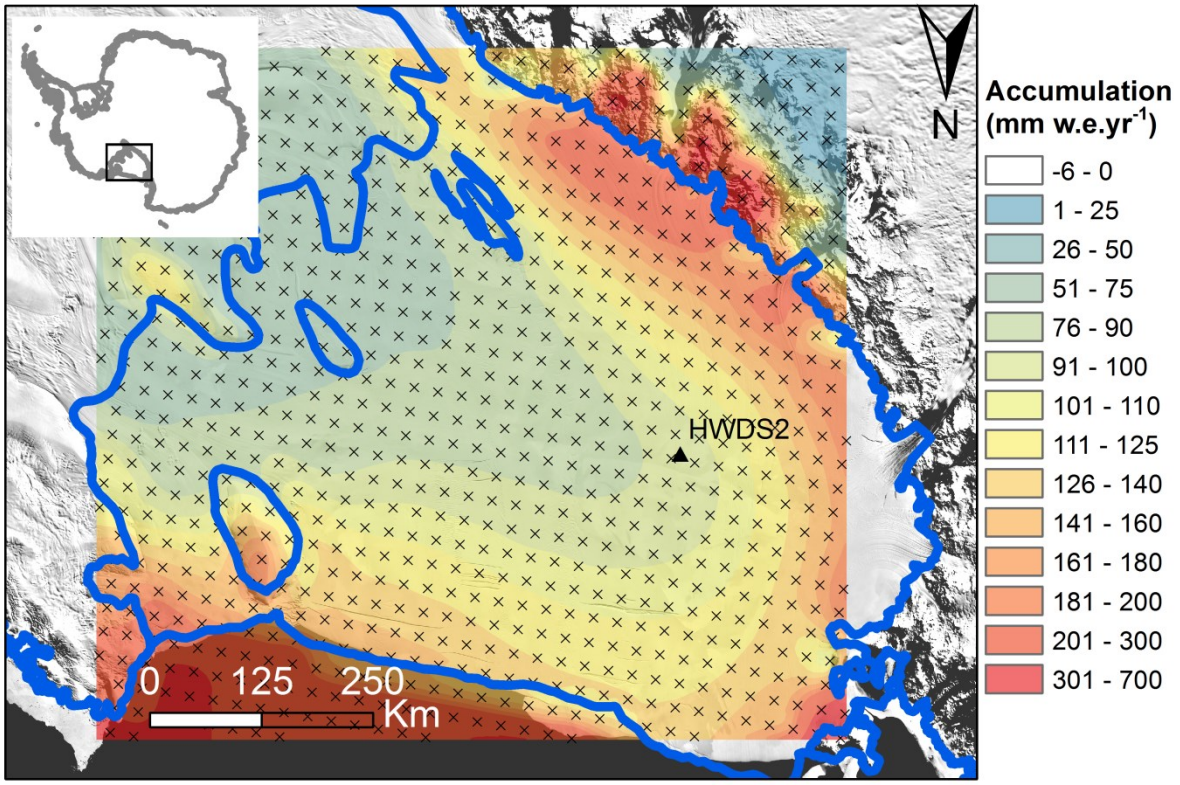

Figure 15: RACMO2.3 Surface Mass Balance data interpolated in ArcMap 10.2 using a Bayesian Kriging method.

Figure 15 shows the RACMO2.3 SMB data for the Ross Ice Shelf. A reasonably similar pattern to those observed in the RIGGS and Favier et al. (2013) data is observed, with a relatively high level of accumulation on the coastal regions and on the lee side of the TAMs. For the study site, HWDS2, the RACMO2.3 data estimates 90-100mm w.e. yr^{1}.

Finally, using passive microwave and field data, (Arthern et al., 2006) estimates snow accumulation at HWDS2 at approximately ~128mm w.e. yr^{-1}. Table 2 presents a summary of the accumulation estimates for the field site, HWDS2.

Table 2: Summary of net accumulation estimates for HWDS2

Source	Method	Accumulation (mm w.e. yr^{-1})
Van Wessem et al. (2014)	Climate Model (RACMO2.3)	95
Dee et al. (2011)	Climate Model (ERA-Interim)	90
Thomas et al. (1984)	Interpolated field data (RIGGS)	110-125
Favier et al. (2013)	Interpolated field data	125-160
Van de Berg et al. (2006)	Climate Model	140
Arthern et al. (2006)	Passive microwave, field data	130
Average		~120

2.3 Ross Ice Shelf Velocity

As the ice shelf flows to the north, it may bring layers of snow formed in a region of higher accumulation, which may need to be accounted for depending on the time series derived. Rignot et al. (2011a) assembled a digital mosaic of the ice motion in Antarctica using multiple satellite interferometric synthetic aperture radar data collected between 2007-2009 (MEaSUREs project). These data indicate that the ice velocity near HWDS2 is between 550-600m yr^{-1} (Figure 16). Depending on the accumulation rate at the site, velocity may need to be taken into account when interpreting results.

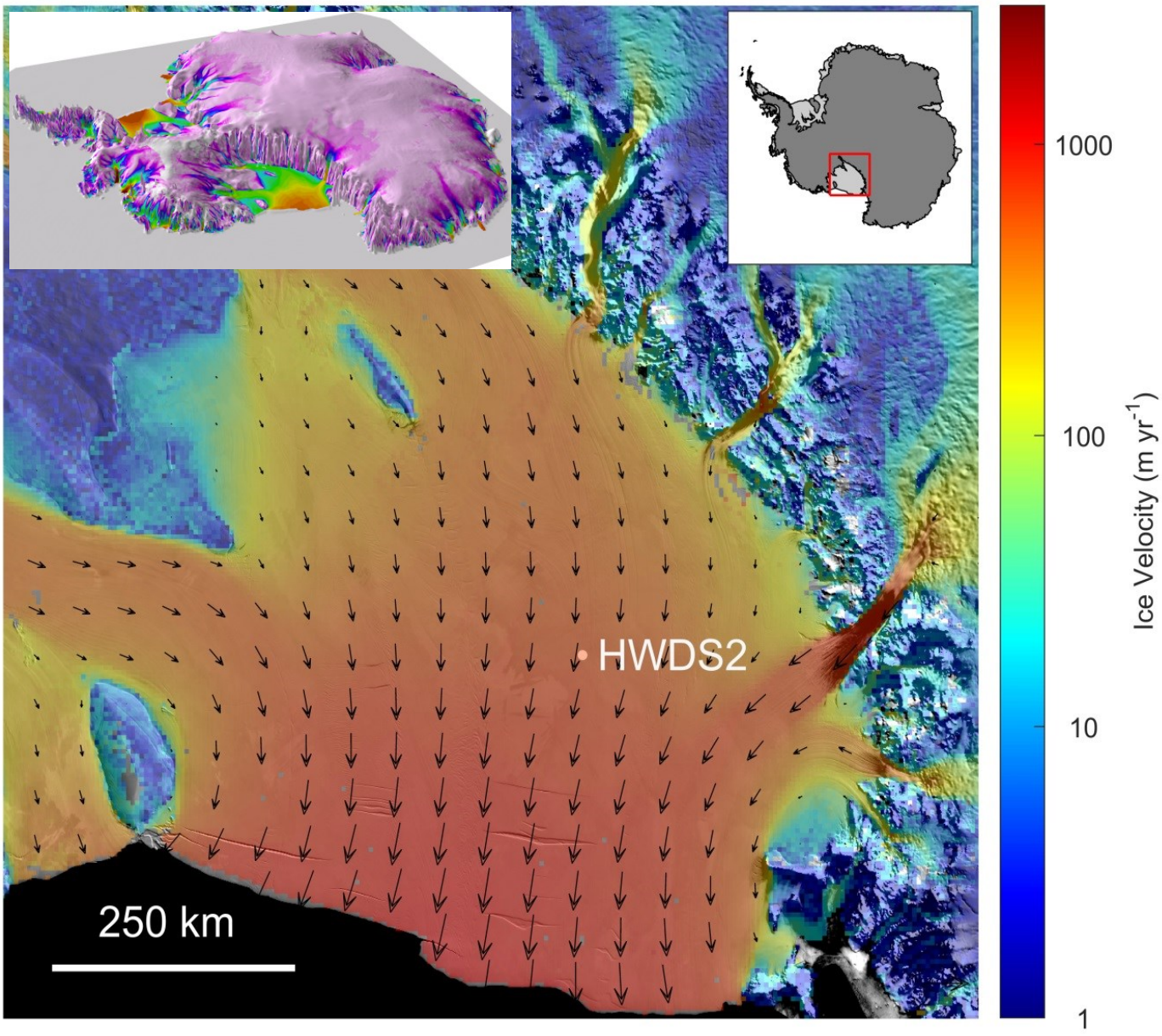

Figure 16: Ross Ice Shelf Velocity (Rignot et al., 2011b) and vectors indicating velocity & flow direction Data from Rignot et al. (2011a) were downloaded from the National Snow & Ice Data Centre (NSIDC). Plotted in MATLAB using the MEaSUREs Toolbox. Top-left inset shows velocity over the whole continent, draped over the RAMP2 DEM.

3 Temporal Variability of Net Snow Accumulation: Annual Layer Counting by means of Stable Isotope Analysis

3.1 Introduction

This chapter focusses on the stable isotope analysis of the firn core used to derive snow accumulation rates. In the interest of clarity and continuity, comprehensive descriptions of the underlying theories can be found in appendices 1 & 2, which are referred to when appropriate.

3.1.1 Stable Isotopes $\delta^{18}O$ and $\delta^{2}H$

Represented by δ values, the isotopic composition of snowfall depends largely on meteorological conditions, resulting in differences between years, seasons, and months, allowing for the determination of both past temperature and annual snowfall. Due to Rayleigh processes (Dansgaard, 1964), snow deposited in summer has less negative isotoptic compositions than snow deposited in winter. Accordingly, by studying isotopic compositions

with high depth resolution, seasonal minima and maxima can be identified, allowing for annual layer counting, thus accurate dating.

Isotopes are elements of the same atomic number, however, as they different numbers of neutrons, they have different masses. Chemically, stable isotopes behave in the exact same manner, but due to kinetic effects, they behave differently in physical and biological systems. For example, the light $H_2{}^{16}O$ water molecule has a vapour pressure approximately 100‰ higher than $^2H_2{}^{16}O$ (HDO) and approximately 10‰ higher than $H_2{}^{18}O$ (Calkin, 1995), meaning the heavy molecules of HDO and $H_2{}^{18}O$ evaporate less readily and condensate more rapidly from the vapour than the lighter $H_2{}^{16}O$. For this reason, global atmospheric circulation depletes heavy isotope containing waters from air masses in high altitudes and latitudes (Dansgaard, 1964; Cuffey & Paterson, 2010).

For practical purposes, absolute concentrations of hydrogen and oxygen isotopes are seldom used. Instead, the ratio of one isotope relative to the other in a given compound is measured against a reference ratio, usually V-SMOW (Vienna Standard Mean Ocean Water) (Brand et al., 2014). The ratios of $^{18}O/^{16}O$ and $^2H/^1H$ of water or ice are measured as $\delta^{18}O$ and δ^2H and are defined in equation 3.1, where δ is either $\delta^{18}O$ or δ^2H.

$$\delta = \left[\frac{R - R_{SMOW}}{R_{SMOW}}\right] \times 1000 \qquad 3.1$$

where R = the abundance ratio of $\delta_{light} / \delta_{heavy}$ in the sample, compared to R_{SMOW}, the standard ratio (0‰ for both $\delta^{18}O$ and δ^2H). Equation 3.1 gives results in units of parts per thousand (‰, per-mille).

The simplest model of atmospheric circulation includes Hadley and Ferrel Cells (Persson, 2006). From the tropics, warm, moist air is transferred in Hadley Cells towards approximately 30°S/N, where Ferrel Cells drive air circulation towards the poles. Ferrel Cells carry evaporated subtropical ocean water, relatively rich in HDO and $H_2{}^{18}O$, towards the polar regions. As these heavier isotopes are preferentially removed, precipitates that occur in progressively cooler regions are gradually more negative in HDO and $H_2{}^{18}O$ (Figure 17) (Dansgaard, 1964; Calkin, 1995; Singh & Singh, 2001; Cuffey & Paterson, 2010). This describes the process of atmospheric isotopic fractionation, or Rayleigh distillation.

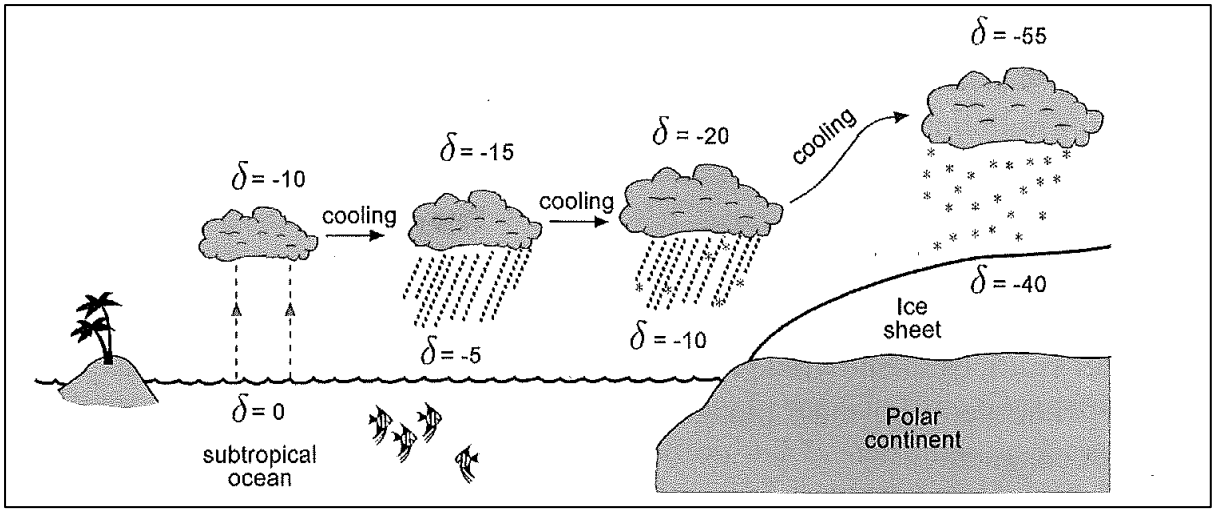

Figure 17: Schematic of moisture transport from mid to high latitudes and the associated fractionation of in $\delta^{18}O$ for the air mass and precipitation i.e. Rayleigh distillation (Cuffey & Paterson, 2010).

Using the definition of δ in equation 3.1, and assuming the initial δ values of the vapour (δ_v) are known, the final δ values in precipitation (δ_p) can be calculated:

$$\delta_p = \alpha(\delta_v + 1000) - 1000 \qquad 3.2$$

where α is an empirically derived value that describes fractionation rates. For a full introduction to Rayleigh distillation and the mathematical descriptions, refer to Appendix 1

The partition of isotopes between two substances or two phases of the same substance with different isotope ratios is called *isotope fractionation*. The dominate phenomena resulting in isotope fractionations are (Sharp, 2007):

- Equilibrium Fractionation: Here, differences in saturation vapour pressure influence the fractionation rate of vapour evaporated from liquid and is thus dependent on temperature. The separation increases with decreasing temperature, and theoretically, at very high temperatures there is no discrimination between heavy and light isotopes.
- Kinetic Fractionation: In addition to equilibrium fractionation, smaller, kinetic fractionation processes also exist. The kinetic effect relates to the diffusivity of isotope molecules, and is primarily dependent on humidity and wind speed at the site of evaporation. Whilst kinetic effects don't substantially alter $\delta^{18}O$ and $\delta^{2}H$ compositions, it remains possible to quantify these effects via the *d*-excess parameter (next page).

A linear relationship exists between δ^2H and δ^{18}O, a relationship known as the Global Meteoric Water Line (GMWL). Craig (1961) plotted δ^2H and δ^{18}O values against each other (Figure 18), and was the first to discover the GMWL: $\delta^2\mathrm{H} = 8 \times \delta^{18}\mathrm{O} + d$, where *d,* deuterium excess, is ≈10‰ in in the majority of meteoric waters on Earth.

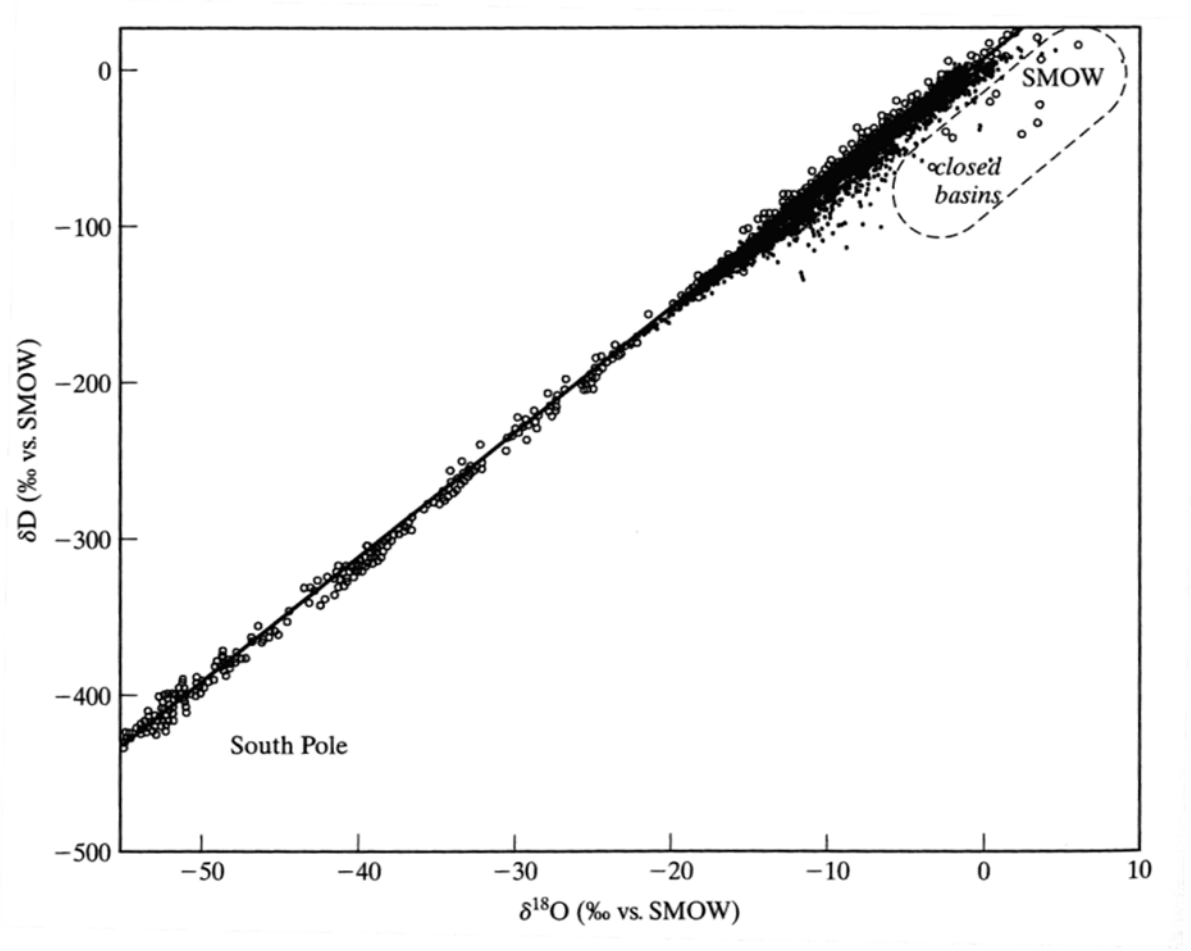

Figure 18: Global Meteoric Water Line. Originally produced by Craig (1961), adapted from Sharp (2007).

The GMWL is a linear relationship that represents the average meteoric water lines from all over the world, but all regions on earth have their own local meteoric water lines (LMWL). The intercept, *d*, or deuterium excess, is defined by Dansgaard (1964):

$$d = \delta^2\mathrm{H} - 8 \times \delta^{18}O \qquad 3.3$$

The *d*-excess parameter explains the deviation from equilibrium conditions and is thus an indicator for kinetic fractionation. *d*-excess increases with an increase in the moisture deficit, 1- *h*, at the site of evaporation, where *h* is the relative humidity at the surface temperature of

the water (Sharp, 2007). Thus, kinetic effects are more dominant at sites of lower humidity. Appendix 1iii on page 118 has a more comprehensive discussion on kinetic effects.

With respect to Antarctic snow, the *d*-excess provides useful insight into the source location of the precipitation, e.g., higher *d*-excess values are associated with precipitation originating from air masses that travel further inland or across the continent and vice versa. At interior Antarctic locations, a negative correlation is generally observed between δ^2H or $\delta^{18}O$ and *d*-excess (Froehlich et al., 2001; Masson-Delmotte et al., 2008), but positive correlations between δ^2H or $\delta^{18}O$ and *d*-excess are commonly observed at Antarctic coastal sites (Ciais et al., 1995; Schlosser et al., 2008). As the source of precipitation on the RIS is thought to come from both the Ross and Amundsen seas, interpretation of *d*-excess records may prove difficult without knowledge of snowfall timing. For example, precipitation originating from the Amundsen Sea often traverses the WAIS, which would lead to high *d*-excess values and more negative δ values via the continental and rainout effect (Dansgaard, 1964). Conversely, precipitation from the Ross Sea would potentially yield lower *d*-excess values and less negative δ values.

Temperature is the main control on the isotopic composition of precipitation, mostly explaining the seasonal variations in δ values. However, secondary effects can considerably alter the isotopic composition therefore must be considered. These secondary effects include the seasonality of precipitation, transport pathway, the initial isotopic composition of the precipitation, and post depositional changes. These effects are discussed in detail in section 3.3.1.

Calkin (1995) states that an annual accumulation of at least ~250mm w.e. yr^{-1} is best suited for annual layer counting using stable isotopes, although estimates vary a great deal. Dansgaard et al. (1973) reported that in Antarctica 340mm w.e. yr^{-1} was required, but more recently, Eisen et al. (2008) have suggested that annual accumulation should be above ~80-100mm w.e. yr^{-1}. In reality, it depends on many more factors such as sampling resolution, snowfall seasonality, temperature, humidity, and wind regimes than accumulation alone.

3.2 Methods

3.2.1 Density estimates and sample resolution determination

In order to get a clear seasonal signal in the isotope record of the firn core, samples must be taken at a high enough sampling resolution to record the isotopic variation in seasonal snowfall – typically between 4-10 samples per annual layer (Fischer et al., 1995; Kuramoto et al., 2011), although this number varies depending on the study goals. Thus, the sampling resolution depends on the thickness of the annual layer, which is controlled by the densification rate.

The transformation of snow to firn to glacial ice is a fundamental process of glaciology (Herron & Langway, 1980). The firn densification rate in Antarctica is dependent on the snow temperature, burial rate (or, net accumulation) and near surface wind speed. Boundary sliding is the main process controlling snow densification until snow reaches approximately 550kg m^{-3}. In this stage, bonds between the individual crystals are formed and air is exchanged between the snow and surface. At densities greater than 550kg m^{-3}, plastic deformation dominates the densification process and air between the grains is compressed and eventually separated into individual air bubbles (Linow, 2011). At densities of approximately 820-840kg m^{-3}, the firn is transformed to ice and the pore space becomes isolated from the atmosphere (Herron & Langway, 1980; Linow, 2011). Glacial ice has a maximum density of 917kg m^{-3} due to the compression of remaining air bubbles.

Densification models (e.g. Herron & Langway, 1980; Maeno & Ebinuma, 1983; Arnaud et al., 2000) often fail to represent density profiles in Antarctica or rely on empirically derived parameters and therefore additional sources of uncertainty (Linow, 2011). Thus, to estimate the density profile at HWDS2, the densification model derived by Linow (2011) was used, which allows for the density, ρ, at a given depth, d, to be derived:

$$\rho(d) = a_0 \cdot exp(a_1 \cdot z) + a_2 \qquad 3.4$$

To derive a_0, a_1, & a_2 the estimated average annual temperature (T) and annual accumulation (A) in water equivalent must be known.

$$a_0 = -0.55793 + 0.00127 \cdot T + 0.006621 \cdot A \quad 3.5$$

$$a_1 = -0.04193 - 0.00054 \cdot T + 0.00257 \cdot A \quad 3.6$$

$$a_2 = 0.85692 + 0.00271 \cdot T - 0.00417 \cdot A \quad 3.7$$

Using these equations and expected average annual accumulation (chapter 2) and temperatures for the vicinity of HWDS2 (based on AWS data supplied by Costanza et al. 2016), the expected density at given depths can be deduced, thus the expected annual layer thickness (Figure 19).

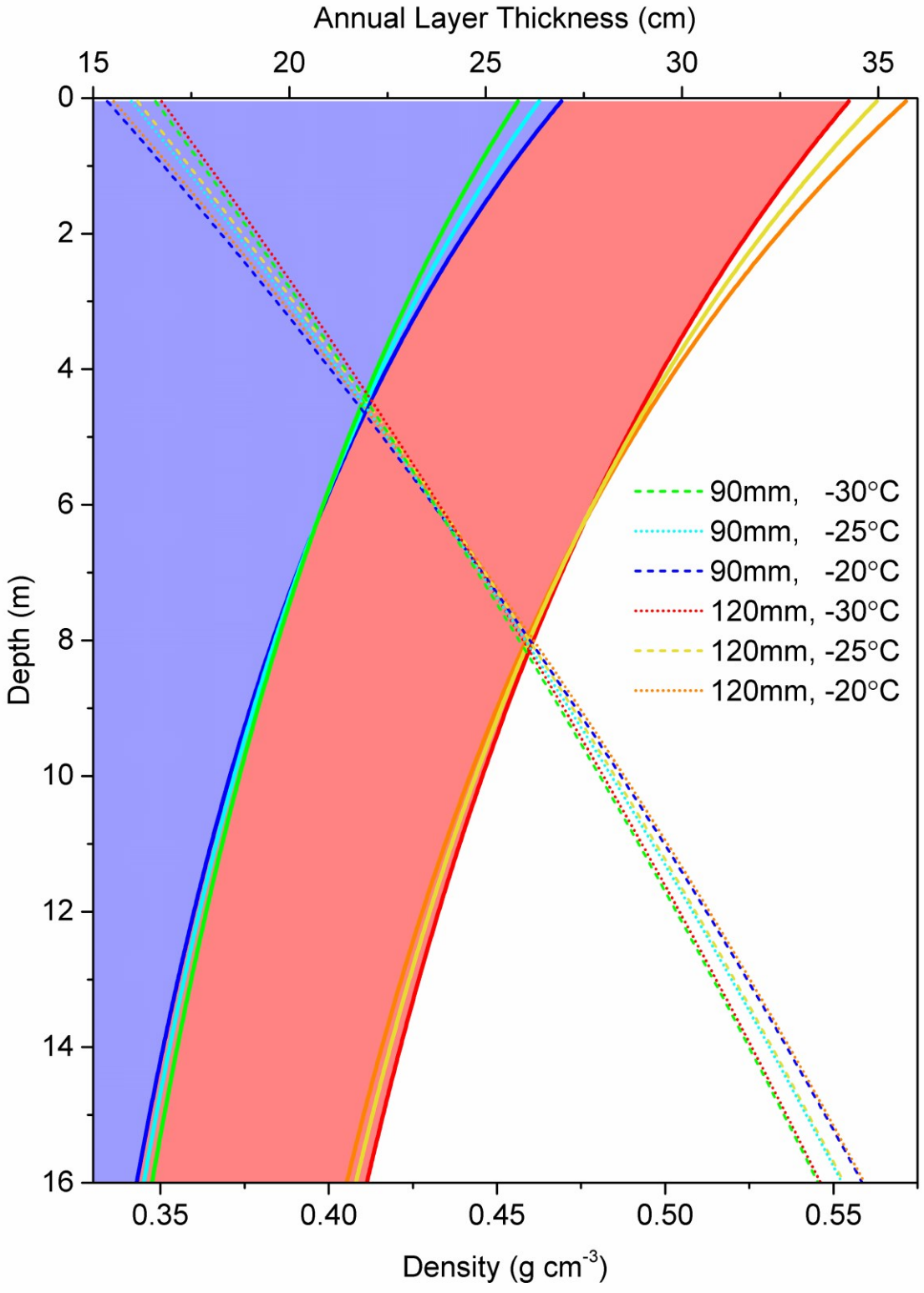

Figure 19: Expected density profile for various temperature and accumulation regimes. Dashed/dotted lines, associated with bottom x axis, represent density for given accumulation and temperature regimes, and the solid lines of the same colour represent annual layer thickness for that regime. Purple (red) shaded areas, associated with top axis, shows expected annual layer thickness for a regime of 90mm (120mm) accumulation and average annual temperature of -20°C (-30°C).

A conservative estimate of 90mm w.e. yr^{-1} accumulation and average annual temperature of -20°C was used to estimate annual layer thickness. To ensure 6-8 samples were collected per annual layer, a sampling resolution of 2-3cm was selected.

3.2.2 Field Component

This section provides information about the methods used whilst in the field. Figure 20 shows the field area and the waypoints that were used during the field season.

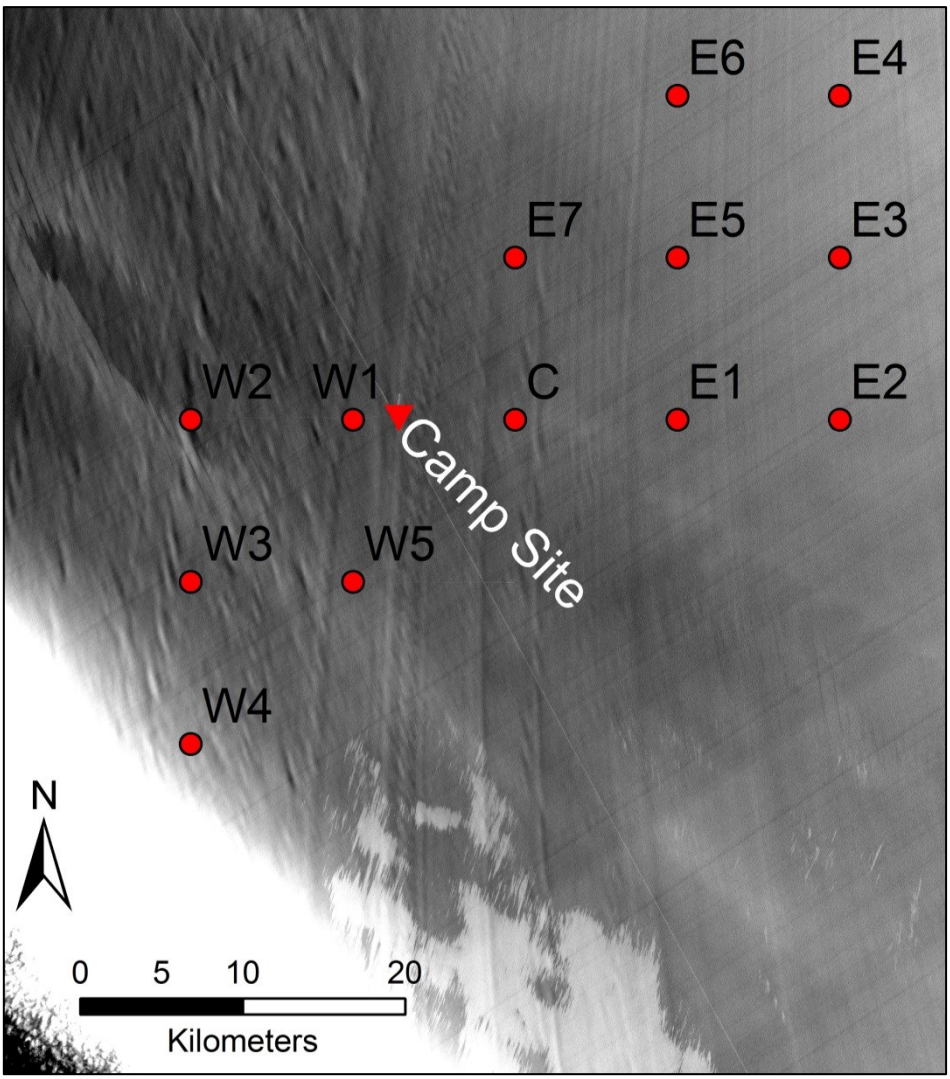

Figure 20: Waypoints near the campsite, plotted on Landsat 8 panchromatic band imagery, acquired on 24.11.2015.

Snow pits and firn cores were collected from both site C and site W3. The snowpit at site C was dug to a depth of 118cm, with the working face kept clear and orientated away from the

sun angle to minimise any potential melt and densification. Density measurements were taken at 3cm intervals using a small steel cylinder with a diameter of 3.56cm.

As per section 3.2.1, the core at site C was sampled at 3cm depth resolution to a depth of 9m, where the sampling resolution changed to 2cm. The core was sliced into individual pieces in situ using a band saw (Figure 21) and a centre section of each slice was 'cut' out using a sharpened hollow cylinder and a small mallet, and weighed for density measurements. It should be noted that whilst all care was taken in this process, some sample densification due to this method may have occurred. As the core extracted from site C was used for the stable isotope analysis, samples were stored in individual 70mL polypropylene containers inside coolers to ensure they remained frozen. Unfortunately, during transport to New Zealand, some samples were subject to melting and this is discussed in the following pages.

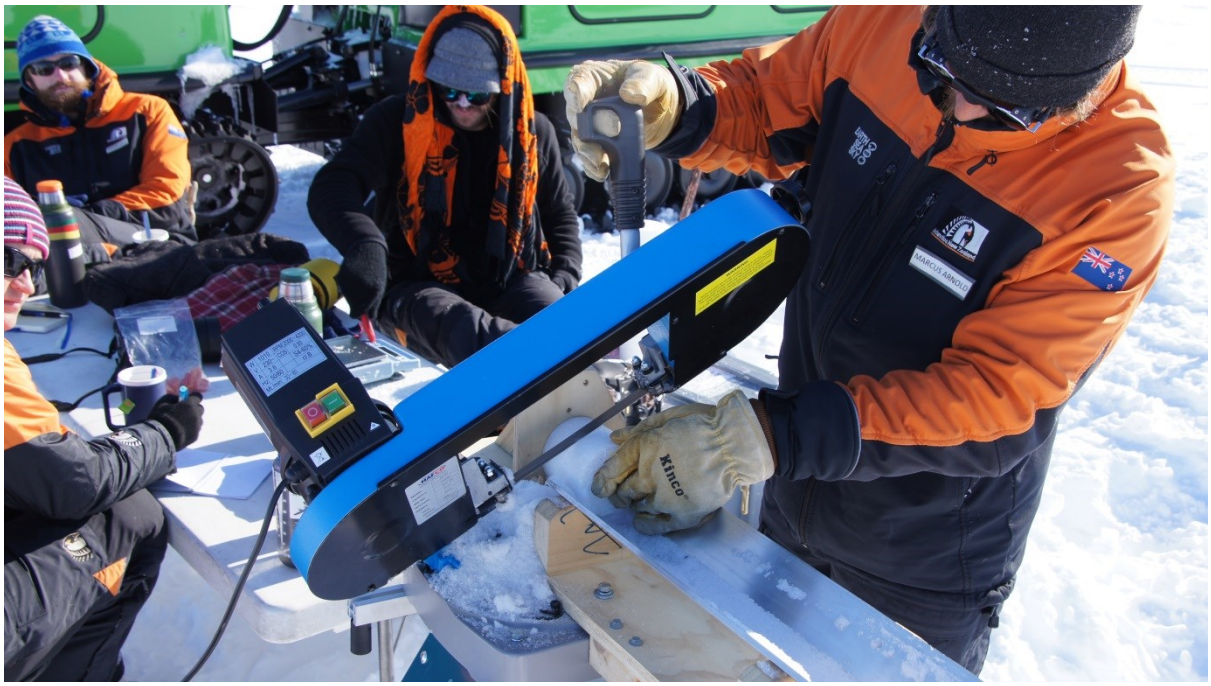

Figure 21: The author slicing a core section using the band saw. Photo: W. Rack.

At site W3 (Figure 20), a 140cm deep snowpit was sampled for density measurements at approximately 5cm depth resolution. The core was drilled to a depth of 14m, and was weighed at 5cm intervals. Both cores were extracted using a Kovacs Mark II coring system (Figure 22). As the measurements taken at W3 were for depth conversion from the radar profiles, 5cm was sufficient sampling resolution. Each core segment was measured, photographed, and described before being sliced with the band saw. Fieldwork at site C and W3 was performed on 25.11.2015, and 29.11.2015 respectively.

Figure 22: The Kovacs Mark II coring system. Photo: JJ. Kelly/National Geographic

3.2.3 Laboratory Component

Ice samples were transported from Antarctica to New Zealand in January 2016, and were kept frozen in a large freezer until required. During sample transport, some (~25%) samples were subject to melting. Expert advice (Nancy Bertler, *pers. comm.*, 2016) suggested that this should not have any large impact on the analysis. Samples were melted and transferred into 2mL glass vials, no more than one day prior to measurement. Sample processing was conducted at the University of Canterbury Geology Department using a Picarro L-1102*i* wavelength scanned cavity ringdown spectrometer (WS-CRDS). For a thorough description of the theoretical background of WS-CRDS methodology, refer to appendix 2.

The firn core extracted from site C was processed using the Picarro CRDS, consisting of an autosampler, a vaporizer, and a wash station containing dimethylpyrrolidinone (DMP) for pre and post cleaning of the syringe to avoid any contamination. High purity (>99.999%) N_2 was used as a carrier gas and was kept between 2.5-4 psi.

The sampling procedure involved the transfer of a 2µL sample to the vaporizer, where it was vaporized at 110°C. The vapour was then moved into the cavity, maintained at 67hPa and 80°C. In the cavity, the 50mW CW diode laser is built up over a period of ~1/10

microseconds, and is abruptly shut off. The decay of the remaining light in the cavity is measured by a sensitive wavelength monitor, which ultimately measures the concentrations of $\delta^{18}O$ and $\delta^{2}H$. Each sample was measured a minimum of six times to account for any memory effects. Any samples that, after six measurements, had a 1σ of greater than 0.1‰ for $\delta^{18}O$ and 2‰ for $\delta^{2}H$ for the final four of the six samples were reanalysed. The first two analyses of each sample were generally ignored. For additional quality assurance measures, any samples that had a change of greater than 1‰ & 7‰ for $\delta^{18}O$ & $\delta^{2}H$, respectively, from one sample to the next were re-analysed. Random samples were reanalysed at various stages throughout the analysis for quality control purposes. Several samples that were not subject to any melt during transport to New Zealand were analysed, re-frozen, and re-analysed. Reanalyses showed that the differences were well within analytical error (<0.1‰ / <1‰ for $\delta^{18}O$ / $\delta^{2}H$, respectively).

Offsets introduced by the instruments are often present (usually at sub-‰ levels), but can easily be accounted for with the use of standards calibration to generate a correction factor. Most standards used (and used in this study) are either (as per the IAEA, International Atomic Energy Agency):

- V-SMOW2 (Vienna Standard Mean Ocean Water) which has a composition of $\delta^{18}O$=0.00‰ and $\delta^{2}H$=0.00‰, or
- SLAP2 (Standard Light Antarctic Precipitation) which has a composition of $\delta^{18}O$=-55‰ and $\delta^{2}H$=-428‰

Additional internal standards were used for this research, and a two point (stretch and shift) normalisation was performed with respect to V-SMOW2 and SLAP2.

3.2.4 Firn Core Dating

Annual layer counting was performed by identifying summer maxima in the $\delta^{18}O$ and $\delta^{2}H$ profiles of the firn core. Using the distance (depth) between two summer maxima alongside the density measurements, conversion into water equivalent was possible. However, due to some poorly resolved sections of the isotope record, other methods had to be included, as described below.

After initial dating was performed using the aforementioned technique, an attempt to validate this method was undertaken using RACMO2.3 climate model data (Van Wessem et al., 2014). The data included daily precipitation, sublimation and runoff amounts for the nearest

grid point to our field site (model grid point 142, 85, location -80.66°, 174.6°). Whilst using climate model data to aid in interpretation of data that is, in turn, used to validate climate model data seems rather counter intuitive, it is reasonable to expect that modern climate models can capture overall patterns of precipitation reasonably well. If, for example, the climate model and empirical core data agree that there is far higher accumulation in a certain year compared to others, it is rational to use that as a validation of the dating technique employed. Further, if both model output and observational data show a year of high accumulation, it is possible to use that year as a reference horizon. By using a reference horizon, year-to-year accumulation rates cannot be resolved as the snow water equivalent to the depth of the horizon is divided by the age of the horizon, giving a single, bulk average amount. Using a reference horizon, however, greatly increases certainty of average net accumulation. Especially useful is when it is possible to use more than one reference horizon, giving better temporal resolution, but also maintaining very high certainty. Using model output is also extremely helpful in guiding annual layer picking in years where the signal is poorly preserved.

The seasonal isotope signal is preserved better in some years than others, with some years showing almost perfect sine-wave signals, and others being hardly discernible. Another method adopted was to ignore any areas where the signal was poorly preserved. This essentially eliminated any temporal resolution of the data as it disabled any dating of the core, but gave an estimation of the accumulation with very high certainty. All methods have their strengths and weaknesses, but combining all of the methods mentioned provides a useful tool in determining an accurate accumulation estimate. The results and uncertainties associated with each method are presented on page 57.

3.2.1 Statistical significance determination

Correlation significance is based on *t*-statistic from a two tailed test, with degrees of freedom adjusted to account for first order autocorrelation within relevant data, as per Bretherton et al. (1999):

$$N_{eff} = N \times \frac{1 - r_1 r_2}{1 + r_1 r_2} \qquad 3.8$$

where N_{eff} is the effective sample size, N is the sample size; and r_1 and r_2 are the lag-one autocorrelations of the time series being correlated. The strength of relationships is based on the Pearson Correlation Coefficient.

Linear trends are assessed based on *F*-test, and significance for all analyses is discerned based on the 95% confidence level (α=0.05). Note that these methods apply for the remainder of this thesis.

3.3 Results & Discussion

3.3.1 Isotope Analysis

652 samples from the firn core were analysed for stable isotopes $\delta^{18}O$ and $\delta^{2}H$ in February and March 2016. This section presents the results from the stable isotope analysis. $\delta^{2}H$ ($\delta^{18}O$) displays seasonal variation ranging from ~150‰ (15‰) in the upper sections of the core, to <15‰ (<2‰) in some of the more poorly resolved sections of the core. The *d*-excess shows no clear seasonal pattern or relationship to $\delta^{18}O$ of $\delta^{2}H$. The final analytical precision is <±0.1‰ for $\delta^{18}O$ and <±1‰ for $\delta^{2}H$, thus, a *d*-excess uncertainty of <±1.3‰ (all ± reported as σ1). The results from the analysis are presented in Table 3 and Figure 23.

Table 3: Descriptive Statistics from the stable isotope analysis

	$\delta^{18}O$ (‰)	**$\delta^{2}H$ (‰)**	***d*-excess (‰)**
Mean	-29.30	-231.85	2.54
Median	-29.38	-232.60	2.48
Standard Deviation	2.16	17.89	2.00
Range	16.64	133.26	13.99
Minimum	-38.73	-307.48	-3.32
Maximum	-22.10	-174.22	10.67
Number of Samples	652	652	652

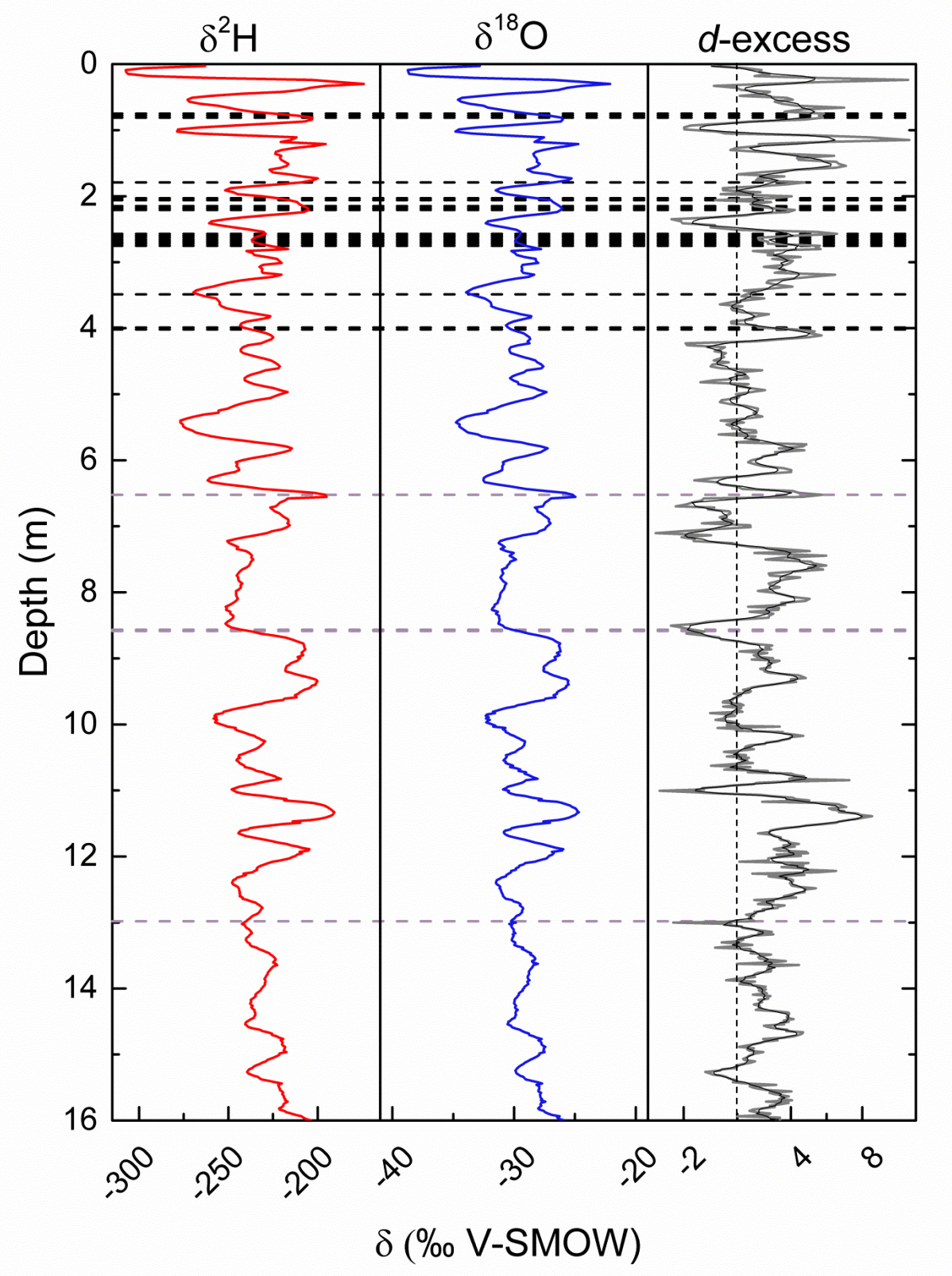

Figure 23: Stable Isotopes δ^2H & $\delta^{18}O$ and *d*-excess depth profiles.Black line through *d*-excess profile shows a 5-period moving window smoothing, and vertical dashed line indicates zero. Black and grey horizontal dashed lines indicate hoar frost and ice layers, respectively. Vertical dashed line represents zero.

The results show that the isotope signal is highly variable – some years show extremely well developed, almost perfect sine-wave signals, whilst others show poorly developed signals with ranges of, sometimes, <1‰ for $\delta^{18}O$ and <10‰ for $\delta^{2}H$. Whilst Dansgaard et al. (1973) state that the seasonal amplitude ($\delta_{winter} - \delta_{summer}$) should be above 2‰ / 10‰ for $\delta^{18}O$ / $\delta^{2}H$, it is impractical to adhere to that methodology as it results in many years' accumulation blended into one in some instances. Snow pit stratigraphy provided little information and had no major relationship with the isotopic composition, an observation consistent with other areas in Antarctica (Martin Schneebeli, *pers. comm.* 2016). In the upper layers, several hoar layers existed, which are often absent in winter snow. Contradicting this, in the core some hoar layers were found at depths that coincided with an isotope minimum. According to Cuffey and Paterson (2010) however, hoar frost layers may in fact form thick layers that could span a period of several years' firn.

The *d*-excess shows no significant relationship to $\delta^{18}O$ or $\delta^{2}H$. Qualitatively, there appears to be a slight, statistically insignificant positive relationship (Figure 24), which is contrary to the negative relationship observed for most of the continent (Masson-Delmotte et al., 2008), although in their review, the negative relationship was mostly absent at sites below 2000m. The LMWL (Figure 25) implies that snowfall is of meteoric origin, and as it sits just below the GMWL, a relatively humid, oceanic source region is likely. Figure 25 also shows the range of measured δ values, with the extreme values at either ends corresponding to the first ~30cm of snow.

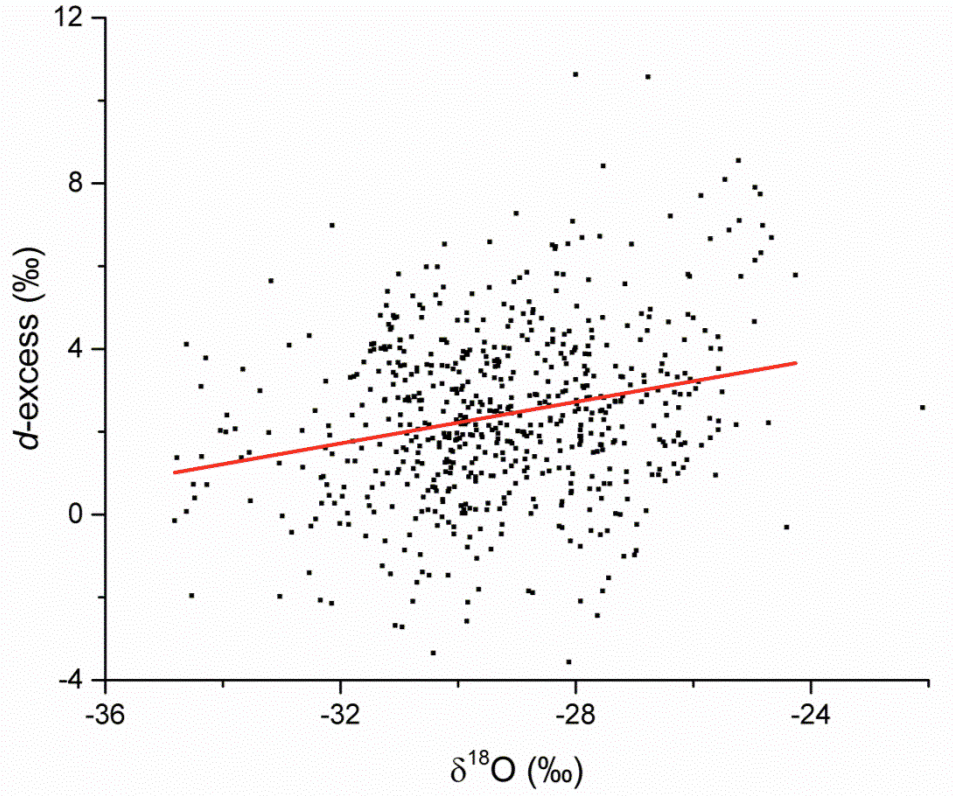

Figure 24: Scatterplot of $\delta^{18}O$ and *d*-excess No significant relationship or trend exists. Red line indicates a best linear fit (R^2<0.1).

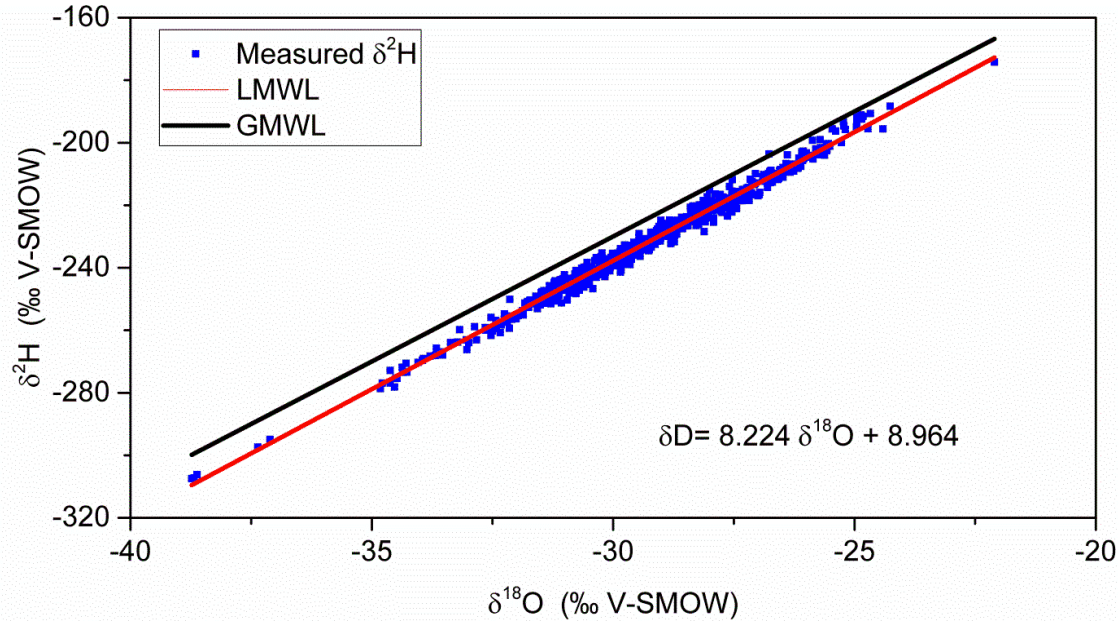

Figure 25: Measured δ^2H, the local meteoric water line, and the global meteoric water line. The LMWL lies just beneath the GMWL.

Due to the lack of meltwater in dry snow zones, post depositional isotopic modification must be due to vapour phase transitions of molecular diffusion rather than transitions between solid and liquid. According to Johnsen (1977), isotopic homogenisation in dry snow can occur when there is a vertical movement of vapour caused by barometric pressure changes or diffusion in the vapour phase. The presence of an ice layer may therefore prevent isotopic homogenisation by 'sealing off' the firn beneath it. On the contrary, when meltwater percolates through the firn, isotopic smoothing tends to occur. In any case, despite ice/melt layers being one of the major processes behind signal preservation/degradation (Johnsen, 1977), no ice lenses are present at depths of good signal preservation, except for perhaps at ~8.6m, where the *d*-excess is also quite negative, suggesting that there may have been some evaporation of the surface melt at the time. *d*-excess is often negative, indicative of evaporation or losses due to sublimation; according to Stichler and Schotterer (2000), in regions of low accumulation and low relative humidity, sublimation losses often result in isotopic enrichment, potentially explaining anomalous sections.. The opposite can also occur when the surface temperature drops and mass is added to the surface via condensation. In the surface layers where there is a large pore space, wind driven atmospheric water vapour can also be brought into the snow where it mixes with the vapour in the pore space. The water vapour molecules can then exchange with molecules of ice crystals, modifying their isotopic composition. In these events, the *d*-excess parameter becomes a poor indicator for moisture source as it becomes too heavily modified (Johnsen et al., 2000). In Antarctica, the diffusion length is ~7-8cm (Johnsen, 1977), and given the wavelength of the majority of the seasonal signals, this effect would be small.

The influence of meteorological conditions and source regions is a more likely explanation. Wind erosion of snow, or deposition of blowing snow have the capacity to eliminate any clear seasonal signals, different moisture source regions may leave vastly different isotopic signatures, and even changes in annual average wind speed can alter the isotopic composition (Town et al., 2008). For example, at Colle Gnifetti in the European Alps, distinct variations are observed in $\delta^{18}O$, but these variations are related to events rather than seasons, and show similar variability year round (Stichler & Schotterer, 2000). On the RIS, snowfall typically arrives from the Ross and Amundsen Seas (Cohen et al., 2013), both of which would leave different isotopic signals (Masson-Delmotte et al., 2008), which may be enhanced even by sea ice variations (Faber et al., 2016). Air-masses that have crossed the WAIS would be depleted in heavy isotopes due to altitude, temperature and continental effects (Dansgaard,

1964), compared to those originating in the Ross Sea that have little, if any, orographic barrier effects and thus a much shorter fetch. SST's also play a role in modifying the δ values – warmer SST's at the moisture source region result in higher δ values, and vice versa. Further complicating the isotope signal is the basic fact that not all precipitation events are the same. Some synoptic systems may simply have more moisture available; so even with the same source region and pathway, the isotope signal would be different. The above processes also complicate the *d*-excess signal (Masson-Delmotte et al., 2008), which is discussed further in chapter 5.

Southerly winds dominate the RIS and during large wind events it is quite likely that deposition of blowing snow from further south occurs, which would lead to a decrease in δ values. On the other hand, as these large wind events often occur in winter, it is equally as likely that low-density winter snow is preferentially removed (Arnason, 1981), leading to an increase in δ values. Indeed, some years may even be completely removed by wind erosion. Further, snowfall is usually associated with strong surface winds that have a virtually unlimited snowfield to scour. Snow drifting usually occurs with wind speeds between 7 and 13m s^{-1} (Bromwich, 1988) – wind speeds that are frequently met on the RIS. Thus, during large precipitation events it is probable that the air is filled with a combination of snow that is actual precipitation, and windblown snow (Bromwich, 1988). Knuth et al. (2010) found on the RIS that over 70% of large accumulation events (>1cm per 30mins) were associated with blowing and drifting snow, and not necessarily concurrent with precipitation. Another possibility is seasonality of snowfall. Whilst generally snowfall is expected to occur year round on the RIS, some years may present a seasonal bias in snowfall, which in turn biases the δ record. This process has been observed in Dronning Maud Land, where a decreasing trend in $\delta^{18}O$ values has been attributed to less winter and spring snowfall, rather than cooler temperatures (Schlosser & Oerter, 2002).

The isotopic composition of precipitation can also change rapidly and drastically, even during single events. Cohen (2013) analysed five surface snow samples collected over a 55 hour synoptic event at Roosevelt Island that resulted in only 3cm of snowfall. She found variations of >12‰ and >105‰ in $\delta^{18}O$ and $\delta^{2}H$ respectively – a huge range that far exceeds seasonal variations often observed. Fernandoy et al. (2012) found a complicated relationship between the isotopic composition of precipitation collected daily and air temperature on the Antarctic Peninsula, stating that the relationship was only suitable over monthly and interannual time

scales. Snow samples collected daily at Dome Fuji showed a strong relationship between temperature and δ values (R^2=0.79), but differences in δ values by up to 20‰ in the same month were also observed (Fujita & Abe, 2006). Similar results were obtained by Dittmann et al. (2016) at the same location. Similarly, at Dome C, Stenni et al. (2016) found variations in δ values of up to ~30‰ in the same season, and found a weaker relationship between temperature and δ values (R^2=0.63). Unfortunate for comparisons with this study, most studies that have collected daily samples are located on the East Antarctic plateau thus have very different precipitation and temperature regimes.

It seems that without in-situ observations it is impossible to attribute specific isotope signals to any single cause. Despite many attempts, relating the isotope signal to AWS data was simply not feasible. It is impossible to attribute any single extreme weather events to a section of the firn core or isotope signal, as there are many extreme events every year, sub-seasonal dating relies on equidistance interpolation between only 1-2 tie points (as per Vega et al., 2016) and there remains a large amount of missing data from the AWS records (which also tend to coincide with extreme weather events). Additionally, attempts to 'match up' the isotope record with the temperature record results in a large degree of human error and potentially, data manipulation.

Finally, a single core might not be particularly representative of the whole area. Klein (2014) found that near Kohnen Station in Dronning Maud Land, $\delta^{18}O$ varied by as much as ~10‰ over spatial distances of less than ten meters for samples collected on the same day. Ekaykin et al. (2016) showed that the isotope content and accumulation covaried with the surface slope of megadunes near Vostok station. Their study revealed that δ^2H varied by up to ~20‰ due to the megadunes over distances of up to 1km, similar results from an earlier study (Ekaykin et al., 2002). Qualitatively, it was noted during fieldwork that there were substantial variations in the firn pack in our study area. Whilst digging snowpits and installing an AWS station, melt layers existing in some snowpits were observed that were absent in others less than ten meters away. On the kilometre scale, changes in the appearance of surface snow were observed, with some areas having a 'crusty' surface and others being quite soft. It is therefore reasonable to assume that if the core were taken from a nearby location, even only some meters away, a different δ signal would be observed, although to what extent remains unknown.

Whilst all care was taken in the field to correctly document and sample the core, human error is occasionally an unavoidable occurrence. To ensure that no sampling errors were made (e.g. sampling the core section the wrong way around), the individual core sections were plotted over the isotope profile (Figure 26).

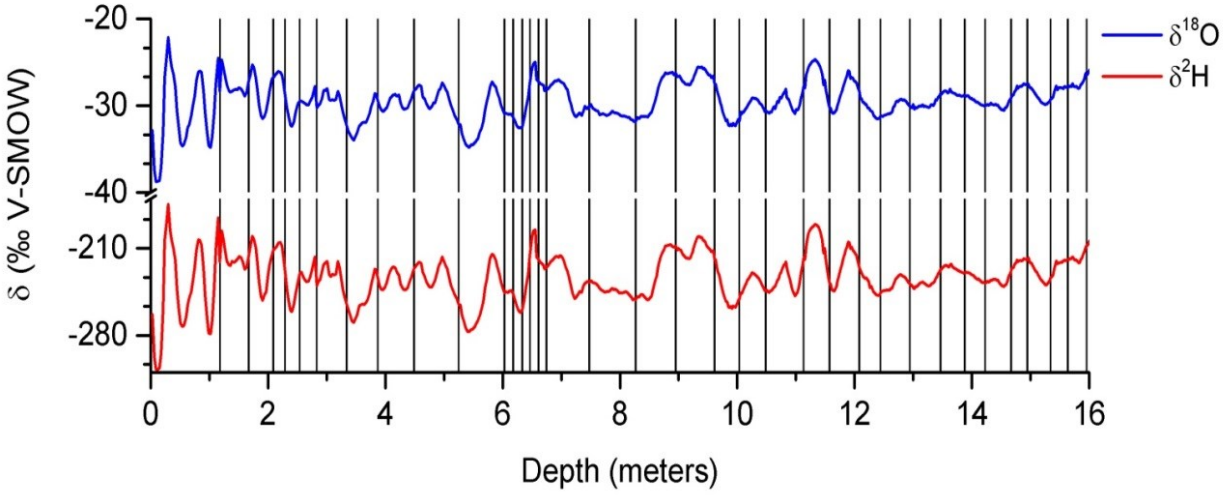

Figure 26: Stable isotope profile with vertical lines indicating the locations of the beginning of each core section.

The first section (sample #39) is from where the snow pit ended and the core started. The sample was an obvious outlier, likely due to contamination of snow from earlier layers in the snow pit and was thus ignored. Otherwise, the core sections show no impact on the isotopic compositions.

3.3.2 Accumulation Rates – Temporal Variability

Based on annual layer counting from the isotope record, average annual net accumulation was found to be 222mm $\pm$ 100 w.e. yr^{-1} (σ1), a 32 (+1/-5) year accumulation record, spanning the period 1984-2015. The accumulation record ranges from 107mm to 472mm water equivalent, a total range of 365mm. Based on *F*-test, a significant (p=0.015), decreasing trend in accumulation is found. The accumulation results are presented in Figure 27, & Figure 28 show where annual layers were chosen based on the isotope record.

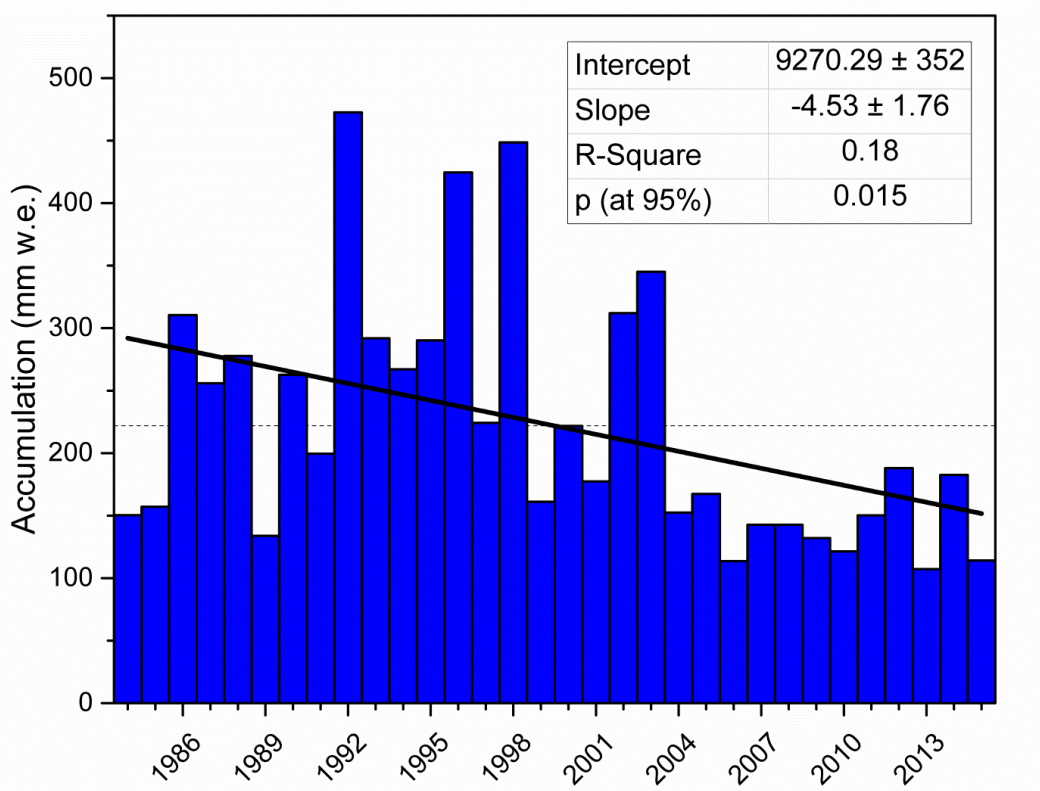

Figure 27: Net accumulation at HWDS2 derived from stable isotopes in a shallow firn core. A significant decreasing linear trend (solid black line) is found based on *F*-test. Dashed horizontal line indicates the mean of 222mm.

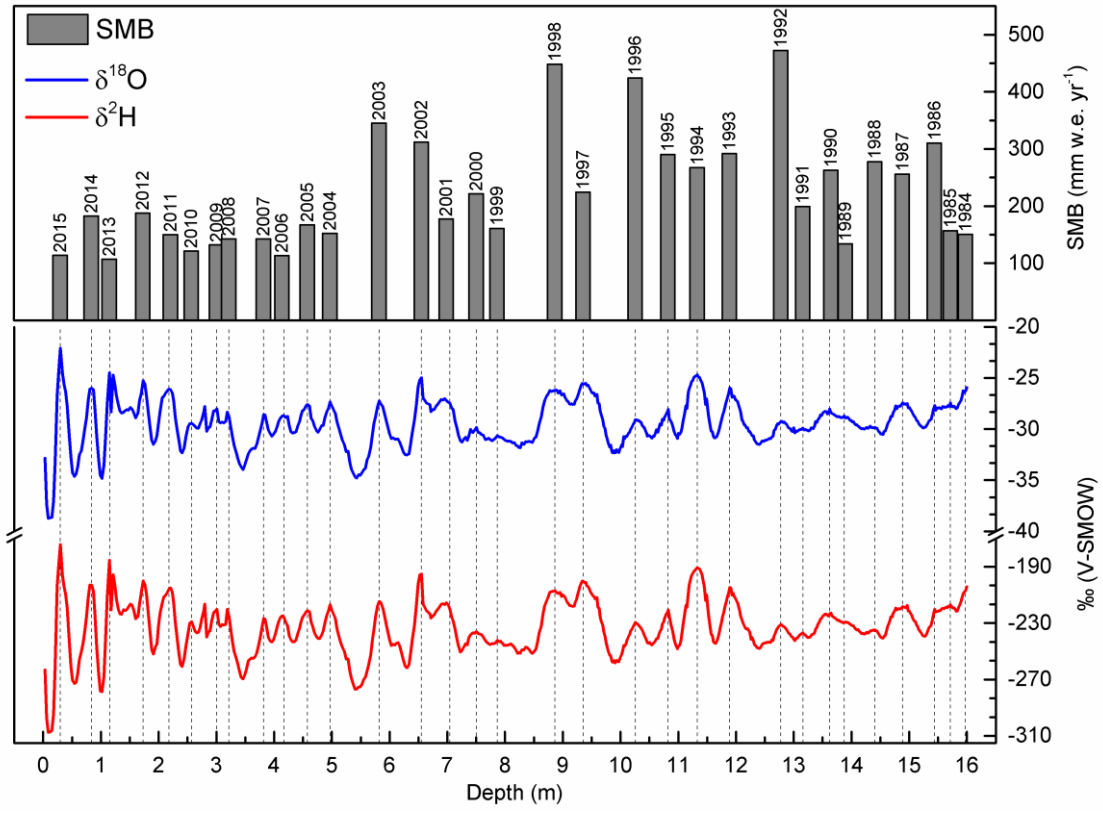

Figure 28: Stable isotopes and net accumulation, with vertical dashed lines indicating where a summer peak was chosen. Note that 2007 and 2008 have the same accumulation estimate. This was done as discerning a seasonal signal was problematic, so the accumulation between 3.01m-3.82m was divided by two and assigned to each year.

Whilst a significant linear trend is present, it is more likely to be a result of the huge interannual variability opposed to a real trend. The time series (i.e. sample size) is also very short (n=32), especially for climatic data. Substantial interannual variations in an accumulation record is not a rare phenomenon: Sinisalo et al. (2013), for example, measured accumulation using the stake method on the Fimbul Ice Shelf 2010-2013. They found accumulation at one site to be 62mm w.e. in 2010 and 475mm w.e. in 2011, an increase of more than sevenfold. Reijmer and Van den Broeke (2003) reported a fourfold increase in the SMB at Berkner Island between 1999-2000 using sonic altimeters on AWS stations. Based on accumulation rates derived from firn cores extracted near Neumayer Station, Fernandoy et al. (2010) showed an interannual range of accumulation to be ~500mm w.e. for a 21yr time series. Similarly, Schlosser et al. (2012) show interannual variations of up to ~500mm w.e. in Dronning Maud Land.

To numerically test the performance of RACMO2.3 and ERA-Interim, the results derived from the core were assumed accurate and compared to the modelled accumulation using the refined Index of Agreement (IoA) (Willmott et al., 2012). The IoA is a standardised measure of the degree of model prediction that varies between 0 and 1 (a value of 1 indicates a perfect match, and 0 indicates no match at all). Generally, anything above 0.5 indicates decent model performance (Cai et al., 2000). The calculation was performed using a MATLAB function written by S. Robeson at Indiana University (http://climate.indiana.edu/Index/d_r.m). As the final years from the core derived accumulation record have low certainty (1984 and 1985), all future comparisons and correlations are used from 1986 onwards. In the case of RACMO2.3, no data from 2015 was available, thus comparisons are based on 1986-2014.

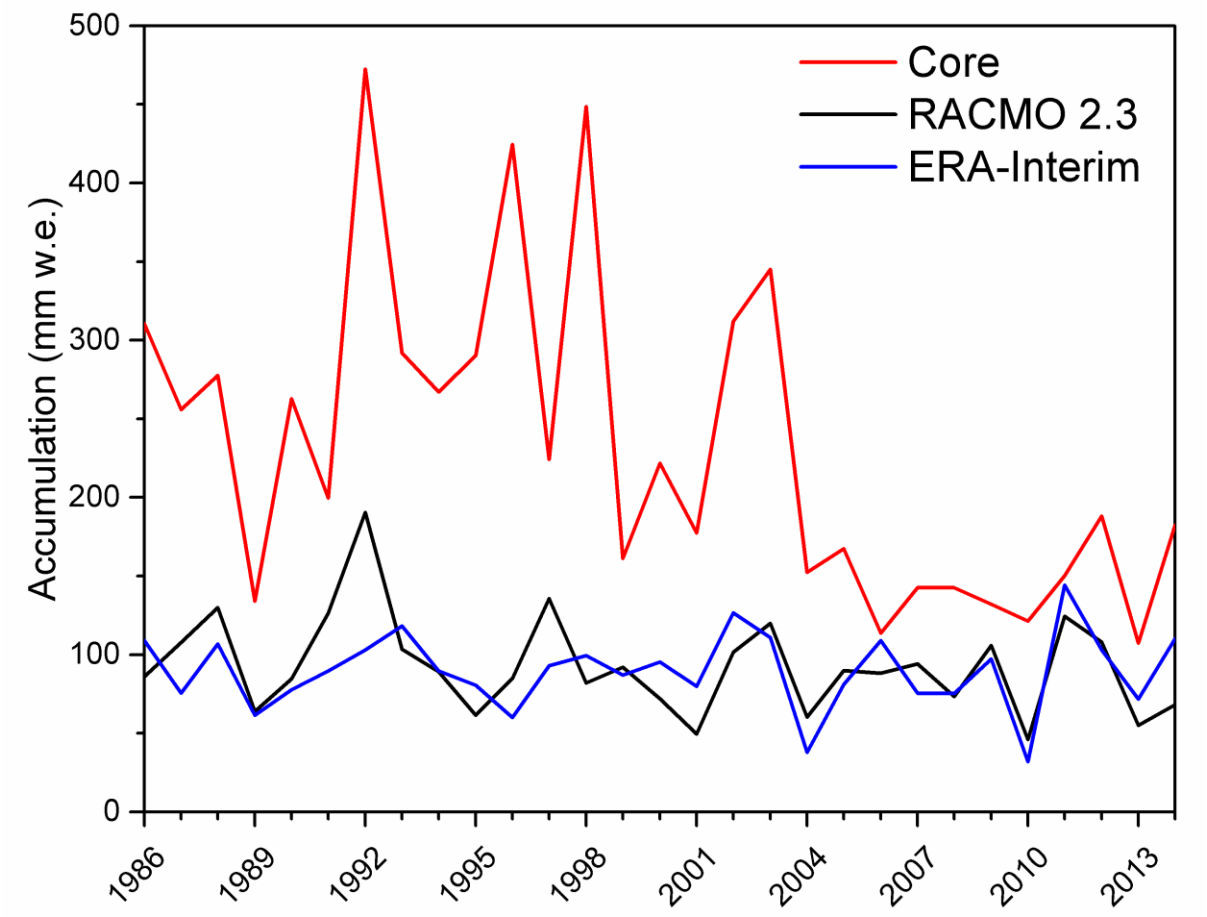

Figure 29: Core derived accumulation and RACMO2.3 and ERA-Interim modelled accumulation. Based on Pearson Correlation, a significant relationship exists, however the index of agreement is low, at 0.17.

Both RACMO2.3 and ERA-Interim capture the overall patterns quite well, particularly RACMO2.3, represented by a significant correlation with the measured accumulation rate ($r=0.45$, $p=0.015$). Both models magnitudes however, are substantially different. Based on the IoA, both models are considered poor performers for our study region, with an IoA of ~0.17 for both. A comprehensive discussion on the reasons behind this is beyond the scope of this study. Nonetheless, the spatial resolution of the models is too low to adequately capture all modes of snowfall, particularly on the Ross Ice Shelf, where mesocyclones and windblown snow likely contribute markedly to the SMB. Unfortunately, even with higher spatial resolution climate models, mesoscale cyclones are not well captured (Peyman Zawar-Reza, *pers. comm.* 2016), although increased spatial resolution may result better representation of snowfall events. Marwan Katurji (*pers. comm.* 2016) has kindly supplied 10km resolution regional climate model (RegCM) output for the Ross Sea region for the year 2013, which captures substantially higher snowfall for HWDS2 than RACMO2.3 (Figure 30).

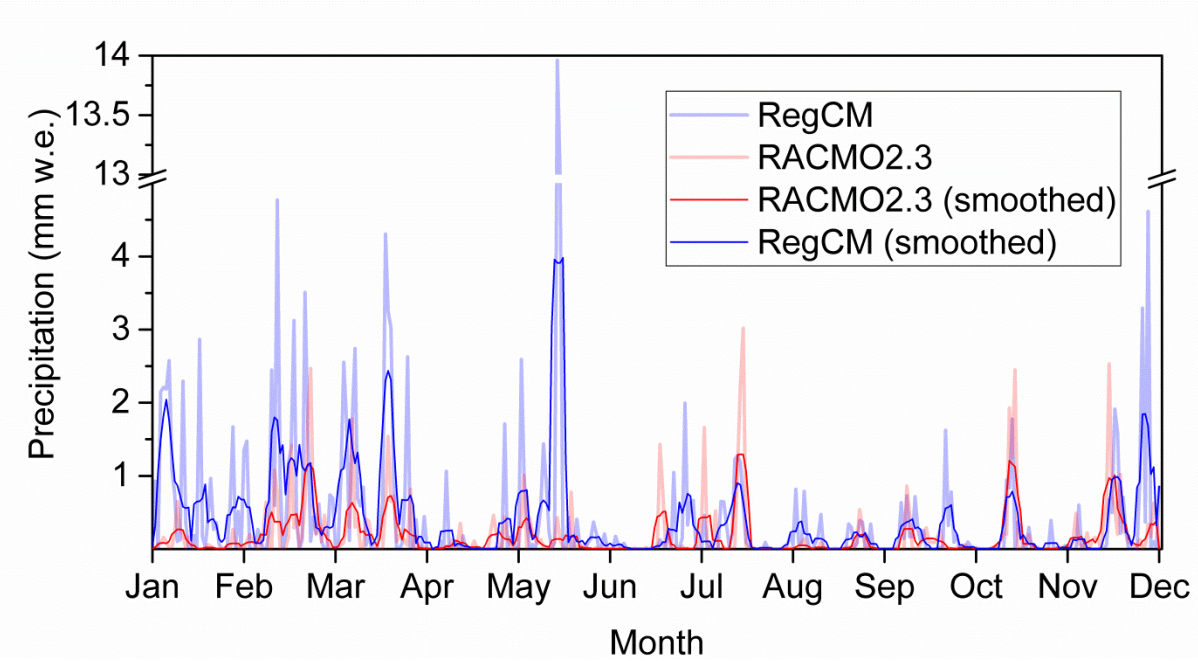

Figure 30: 10km resolution RegCM and RACMO2.3 precipitation for the closest grid-point to HWDS2 for 2013. Note the axis break between 5 and 13 mm w.e..

For 2013, RACMO2.3 suggests 56mm w.e. precipitation whilst the higher resolution RegCM suggests 157mm w.e. (core derived accumulation is 107mm w.e.). Although both models are forced by ERA-Interim, differences between models are due to more than spatial resolution alone; it is clear than increased spatial resolution aids in capturing the magnitude and frequency of precipitation events.

As RACMO2.3 is currently considered the best performer for the Antarctic (Wang et al., 2016), it will be used for all future discussions. Despite the poor IoA, RACMO2.3 shows, for example, that 1992 and 2003 were relatively large years of accumulation – years that align well with the core-derived age estimates. Consequently, 1992 and 2003 were used as reference horizons. As discussed in section 3.2.4, combinations of different dating techniques were used and the results of each method are shown in Table 4.

Table 4: Accumulation estimate, σ_1, time span, and confidence (qualitative) from each method used

Method	Result (mm w.e. yr^{-1})	σ_1	Years Resolved	Confidence
Annual Layer Counting using Stable Isotopes	222	100	32 (+1/-5)	High
'Perfectly' preserved seasonal signals only	218	99	13	Very High
2003 reference horizon	160	N/A	13	Very High
1992 reference horizon (1992-2003), not incl. 2003.	299	N/A	11	Very High
1992 reference horizon (1992-2015, inclusive).	224	N/A	24	High

The data shows that there is generally good agreement between the methods – annual layer counting, well-preserved signals and the 1992 reference horizon (to 2015) have a range of <10mm w.e. Not surprisingly, the 2003 (to 2015) reference horizon yields a much lower result, and the 1992 horizon (to 2003) yields a much higher result. The average of all methods is ~225mm w.e. yr^{-1}, which is essentially the average annual accumulation from the first method. Confidence levels for each method are purely qualitative. 'Years Resolved' refers to the amount of years' worth of net accumulation in each method, and not the actual length of the time series (e.g. there were 13 'perfectly preserved' seasonal signals, giving an average of 13 different years' net accumulation, however no dated years are associated with that method). Despite efforts to minimise uncertainty in the accumulation estimates, there is still the possibility that subjectivity in annual layer counting, unclear isotope signals, and errors in density estimates has led to erroneous results. It is for this reason that stable isotope analyses of firn cores is deemed only a "conditionally accepted" method, and is given a "B" rating for reliability, as per Magand et al. (2007). Assuming that 8 years' accumulation data are 'missed', giving a 40 year time-series, annual average accumulation is >175mm w.e., which is still markedly higher that previous estimates.

Chapter 5 describes the climatological controls on accumulation and a more thorough discussion on the temporal variability is found there.

3.4 Summary

A stable isotope analysis of a shallow firn core was used to determine the spatiotemporal variation and magnitude in accumulation at HWDS2. It was found that the annual accumulation is considerably higher than hitherto expected at ~222 mm w.e yr^{-1}, almost double estimates based on available data. It may take up to 1000 years for ice to reach the ice shelf edge, thus addition of mass via snowfall accounts for a much of its overall mass balance. If snowfall is indeed much higher than previously thought across the entire, or much of the ice shelf, the implications for its future behaviour and current estimates of its mass balance (e.g. Rignot et al., 2013), may be changed markedly. There is considerable interannual variation, with a range of 365mm w.e., and whilst large, such variations are common for Antarctic coastal sites. A significant decreasing trend in accumulation was found, although this is more likely a result of the large interannual variation and short time series. RACMO2.3 and ERA-Interim were found to be poor performers in this region based on the Index of Agreement calculation, likely due to the complex precipitation regime of the Ross Ice Shelf. Variations in the isotope signal are discussed in detail, although no major conclusions are drawn as, without in-situ observations, attributing any single section of the isotope recorded to a single event is simply not possible.

4 Spatial Variability of Snow Accumulation by means of Ground Penetrating Radar Analysis

4.1 Introduction

Frezzotti et al. (2004) showed that SMB variability at sub-kilometre scales is responsible for far greater SMB variations than temporal variability at the century timescale, thus understanding the magnitudes of local variability is critical in our understanding of the Antarctic SMB. Ground Penetrating Radar (GPR) is a commonly used method to image the subsurface, and is often used to image internal layers in glaciers and snow-packs, particularly useful for measuring snow accumulation if the internal layer is dated and density is known (Arcone et al., 2004; Daniels, 2004; Jol, 2009).

A typical GPR arrangement consists of a transmitter and a receiver in a fixed geometry, which are moved over a surface to detect reflections from subsurface materials (Jol, 2009) (Figure 31). Reflections are generally caused by changes in conductivity or permittivity, with density being the main cause for dielectric contrasts in relatively shallow depths (Hubbard &

Glasser, 2005). A pulse length between 400MHz-1000MHz is ideal for polar firn studies, as it allows for a deep enough penetration and identification of internal layers, whereas lower frequencies are preferred when deeper penetration is necessary, for example when determining ice thickness (Plewes & Hubbard, 2001).

The use of GPR systems for cryospheric research is common; GPR has been used to study basal conditions of glaciers (e.g. Copland & Sharp, 2001) and ice shelves (e.g. Rignot & Steffen, 2008), water content within snow-packs (e.g. Sold et al., 2015) internal structure of ice and firn (e.g. Arcone, 1996; Vaughan et al., 1999b; Pälli et al., 2002) and surface accumulation magnitudes and variability (e.g. Kohler et al., 1997; Rotschky et al., 2004; Spikes et al., 2004; Dunse et al., 2008; Müller et al., 2010; Kruetzmann et al., 2011; Hawley et al., 2014).

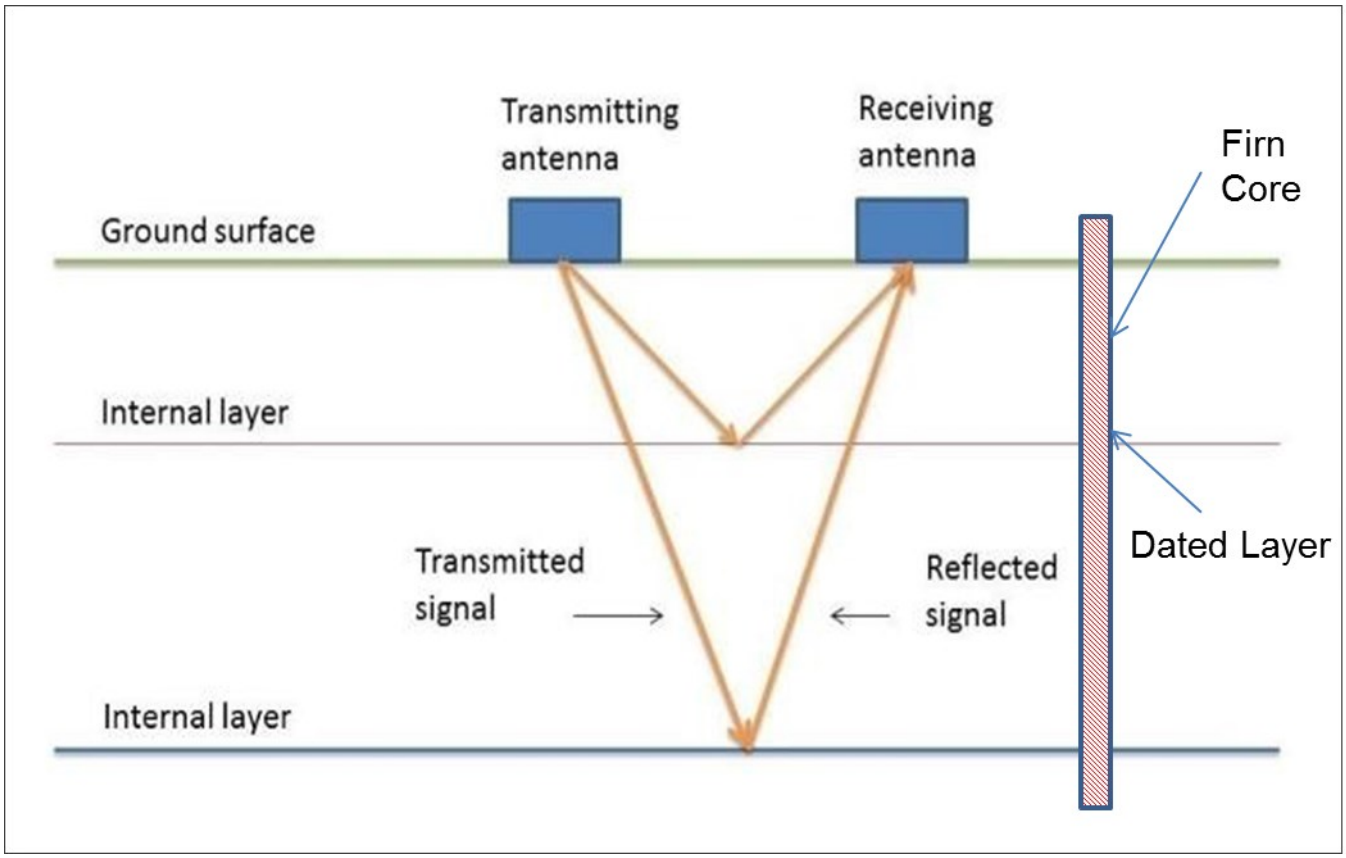

Figure 31 Schematic illustrating the basic properties of a GPR arrangement. Firn core added for illustrative purposes, showing how a dated layer can be expanded to a wider area. Modified from Michelle Ryan (*pers. comm.*, 2016)

Internal reflections that can be followed over long distances are assumed to be isochronal events that may have happened over a period of days (e.g. melt events and storms) or years

(e.g. depositions from volcanic eruptions). These isochrones can be used to synchronise ice core records from different locations and derive accumulation rates by matching them to firn cores and snow pits, as is done in this study. The amount of layers present within a firn column depend mostly on weather conditions at the time of deposition and shortly afterwards (Harper & Bradford, 2003), and as snow crystals are compressed with increasing depth, internal layers may merge, thus reducing the amount of reflectors in a radargram (Kruetzmann, 2013).

In the Ross Sea region, GPR has been used on the McMurdo Ice Shelf to estimate lateral extent of layers within ice (Arcone, 1996) and accumulation and compaction of snow (Kruetzmann et al., 2011). On the Ross Ice Shelf, GPR has been used to estimate ice thickness (Bentley et al., 1979), detect crevasses (Delaney et al., 2004), measure basal melting (Catania et al., 2010) and interpret and date historical changes in ice flow dynamics of the Ross ice streams (Catania et al., 2012). Little has been done with GPR on the RIS with respect to measuring snow accumulation, although the ROSETTA-ICE (Uncovering the Ross Ocean and Ice Shelf Environment and Tectonic setting Through Aero-geophysical Surveys and Modelling) program intends in 2015-2017 to use radar to determine surface accumulation comprehensively across the entire ice shelf. HWDS2 is situated in the middle of a particularly large snow accumulation gradient (see Figure 15, page 29), making it an idea area to investigate spatial variations.

4.2 Methods

4.2.1 Field Methods

A PulseEKKO PRO 500MHz GPR system was used, with a Trimble GeoXH GNSS (Global Navigation Satellite System) used for GNSS tracking. The DVL (data video logger, i.e. ‘control panel’) for the GPR system was maintained above 0°C during use, with the aid of an insulated box and heat packs (Figure 32a) Spare batteries were always carried, and when the voltage dropped below 11V, the battery was replaced.

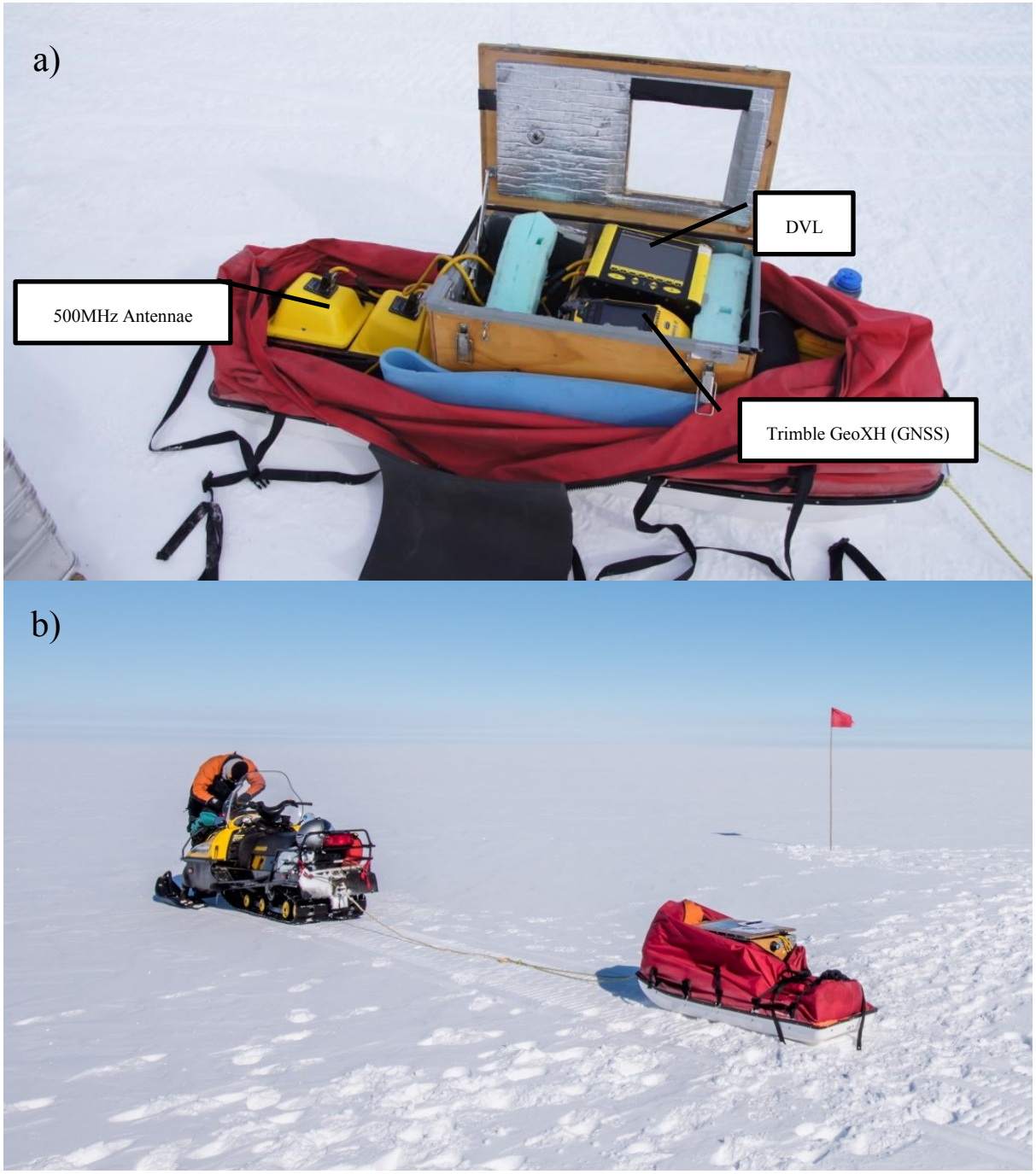

Figure 32: a) 500MHz GPR set up with shielded antennae pairs (separated by 0.23m), GPS, DVL, and insulated DVL box. b) GPR set up being towed behind a skidoo

The GPR was towed behind a skidoo, with speeds not exceeding 10-15 km h^{-1} (Figure 32b). Specific settings of the GPR varied, however minimal in-situ processing was applied as this could easily be done in post processing. The system was set to free run mode, where it took traces at regular intervals. Upon plotting of the GNSS points, the resultant average spacing

was approximately 2-5m per trace, depending on skidoo speed and the post processing steps undertaken. GPR profiles were collected between the 26.11.2015 - 30.11.2015, and the exact profiles that were taken are shown in Figure 33. Unfortunately, the GNSS disconnected during profiles from W2-W5 and from W3-W4. To account for this, an equidistance interpolation of coordinates was performed for each profile using the known coordinates of the waypoints. This is noted as a source of potential uncertainty as the skidoo speeds varied, despite best efforts to remain at a constant speed.

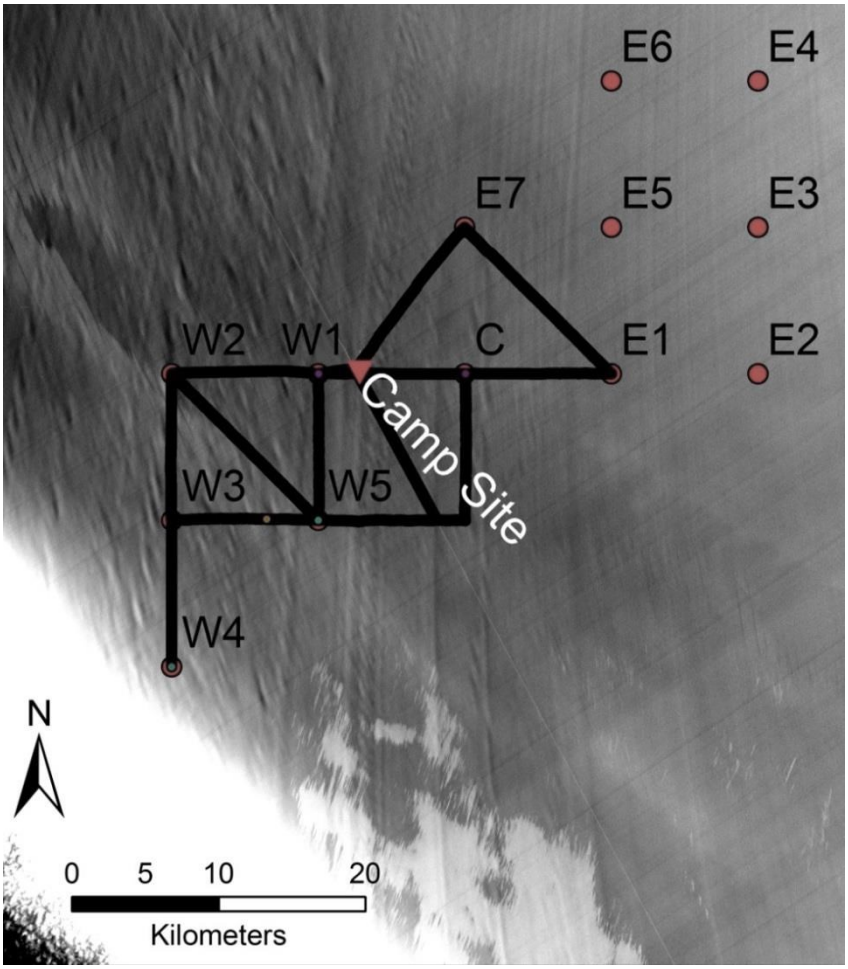

Figure 33: GPR profiles taken (shown as black lines)

4.2.2 Post Processing

GPR data were processed using ReflexW software from Sandmeier Scientific Software. An adapted combination of these general processing steps was applied to each profile:

1. Dewow

The close proximity of the receiver to transmitter in many GPR set-ups often results in a low frequency energy field near the transmitter, yielding a time-varying component to the field data (Jol, 2009). This causes the base level of the signal received to bow up or down, known as the "wow" effect. Dewow filtering is in its simplest form, a running mean filter, that subtracts the average values within a given window from the centre window value (Kruetzmann, 2013).

2. Gain (energy decay)

An energy decay filter was applied to account for the attenuation of the signal with depth. Energy decay was found to give the best results, although exact parameters differed for each individual trace. Most profiles used a scaling factor of 0.8 when applying the energy decay filter.

3. Band pass frequency

As an effective noise reduction method, trapezoidal band-pass frequency filters were applied to most traces, which improved data noticeably. This filter eliminated frequencies that were outside the range of frequencies considered to be part of the main signal (Kruetzmann, 2013). Different cut-off points were used, but were typically ~ 50/380 -780/900MHz.

4. Deconvolution

Deconvolution was applied to remove ringing noise/reverberation artefacts, and was used to maximise bandwidth and reduce pulse dispersion (Jol, 2009). Similar to other processing steps, no single parameters were used and were altered depending on the trace. Typical parameters however, involved autocorrelation start/end values of ~0/170 with a filter length of 2.

5. Stack traces

This was the final processing step done, and the amount of traces stacked depended on the noise and length of the profile. Stacking is simply the average of a specified number of traces, which helps to strengthen signals and remove noise.

Other filters that were applied included removal of zero traces and changing the start-time, which had no influence on the interpretation of profiles.

4.2.3 Two way travel time conversion

To accurately convert the two way travel (TWT) time of the radar wave to depth, the relative dielectric permittivity must be estimated using knowledge of the snowpack density. The propagation of a radar wave through ice is determined by electrical permittivity and conductivity. Electrical permittivity describes the capacity of a material to store an electrical charge, and its value changes depending on the properties of the material. The relative dielectric permittivity, ε'_r, of dry snow is related to the density, ρ (in kg m^{-3}), using the empirical formula (Kovacs et al., 1995) :

$$\varepsilon'_r\,(\rho) = (1 + 0.0845 \times \rho)^2 \qquad 4.1$$

When a transmitted radio-wave meets a boundary between two differing materials (i.e. materials with differing dielectric properties), the radio-wave is transmitted, refracted or reflected back to the surface, which ultimately provides information about the sub-surface characteristics at a given depth.

Most systems detect the backscattered signal from the target (Daniels, 2004) which is returned to the receiver as a trace. The trace includes a two-way-travel-time (TWT) (the time that it takes the pulse to travel to and from the target, in nanoseconds) and amplitude, which is dependent on the dielectric contrast. Using the density information from snow pits and firn cores to estimate ε'_r, the velocity, v, at depth, d, of the radar signal through the snow can be calculated:

$$v(d) = \frac{c}{\sqrt{\varepsilon'_r(d)}} \qquad 4.2$$

where c is the speed of light in a vacuum ($\approx 3 \times 10^8 \frac{m}{s}$). This allows the TWT to be converted to depth, allowing for accumulation estimates to be derived from the GPR profiles (Jol, 2009).

Visible reflectors within radar profiles were manually picked and exported in ASCII format, which contained the TWT, and coordinates. Using equation 4.2 this can be converted to depth, which is then converted to SWE and divided by the age derived from the firn core to

get the accumulation in mm w.e yr^{-1}. The density estimates that were used in equations 4.1 & 4.2 were derived from the exponential model derived by Alley et al. (1982):

$$\rho(d) = \rho_i - a \cdot exp^{-c \cdot d} \qquad 4.3$$

where ρ_i is the density of ice (917 kg m^{-3}), and a and c are the constants to be fitted. The model was fitted to the empirical data using the curve-fitting tool in MATLAB. As density profiles were taken at both C and W3, an average of the two density profiles was used when converting the TWT to depth.

Density was measured in-situ and modelled for the use of determining SWE and GPR depth conversion, respectively. Based on an analysis of covariance (ANCOVA), the density profiles at site C and W3 were statistically different ($p<0.01$) so an average of the two modelled density profiles was used for GPR time-depth conversion. This is acknowledged as a potential source of error, as in general, lateral and vertical variability in depth-density relationships are the largest source of error when using GPR for shallow layer approximation (Sinisalo et al., 2013). Figure 34 shows the density (measured and modelled) profiles for both sites.

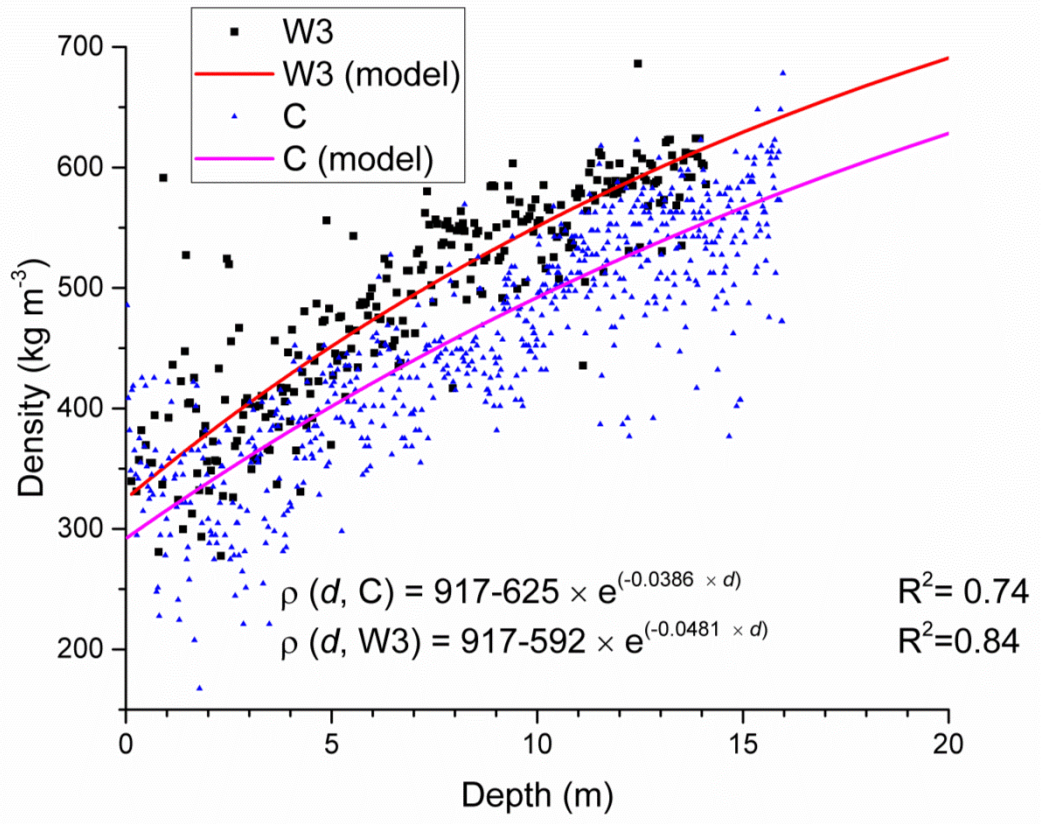

Figure 34: Density profiles (measured and modelled) for site C and W3 showing the constants derived from the MATLAB curve fitting tool for equation 4.3.

4.3 Results & Discussion

The GPR profiles required post-processing, as internal reflections were extremely weak and variable (Figure 35). Despite all profiles showing distinct reflections, the only continuous (i.e. visible in all profiles) reflector was observed at a depth of ~9m and was used as an isochrone to determine accumulation.

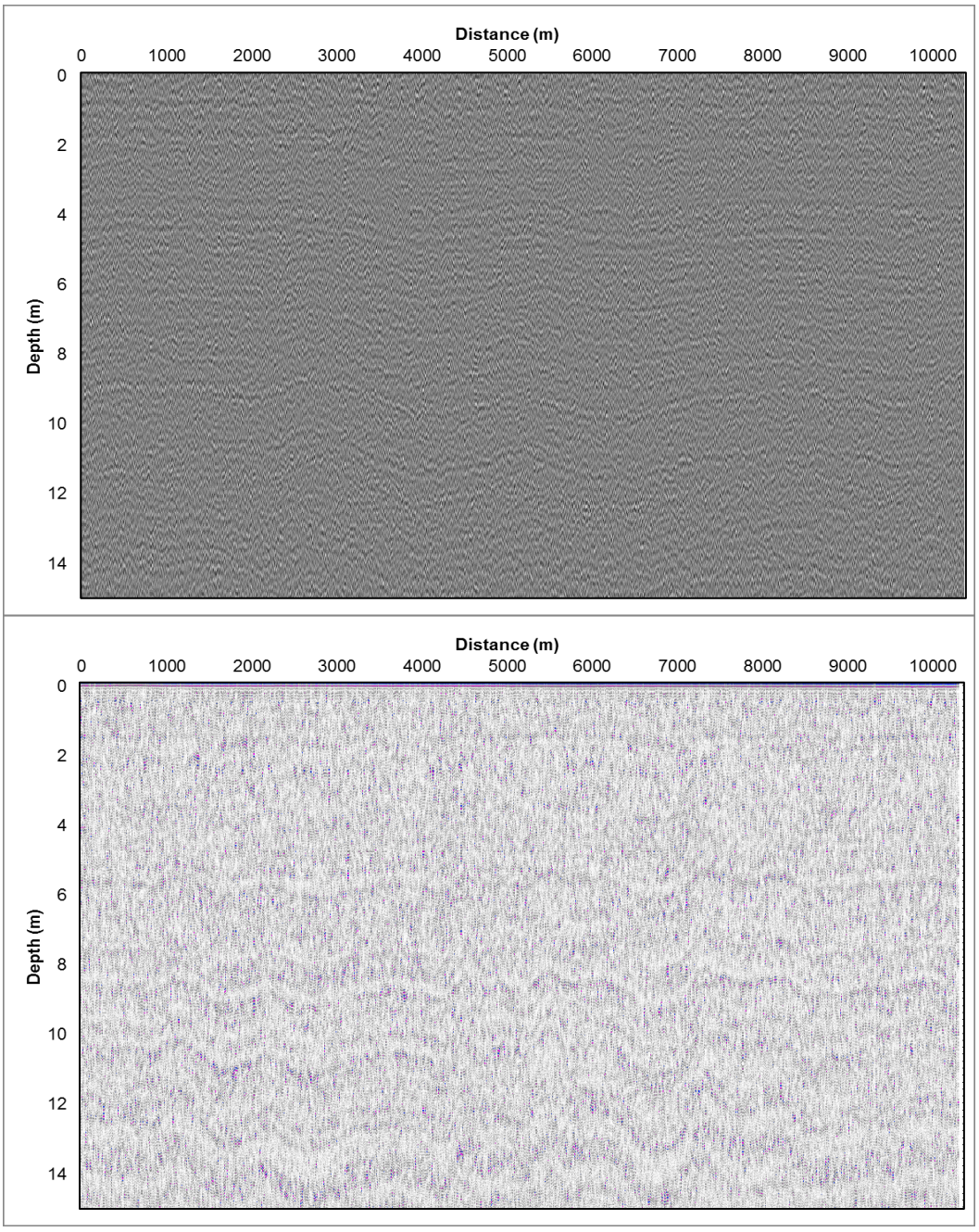

Figure 35: Examples of processed GPR traces (top = W3-W4, bottom = W3-W5). Internal reflections become more pronounced with depth and are more variable in east-west orientation than north-south. Illustrative figure only – depth & distance axis are approximate.

This layer was dated to 18.25 years based on the firn core processing presented in section 3.3.1. The depth of the isochrone was then converted to snow water equivalent (SWE) using the modelled density data, and divided by 18.25 to obtain accumulation per year.

To confirm the accuracy of the time-depth conversion and the use of the density models, the SWE (core derived) was cumulated to radar-derived depth (for the core site, C) and divided by 18.25. Results show that the difference between the core derived accumulation and radar derived accumulation are very small, with core and radar derived accumulation rates of 190 and 195 mm w.e. yr^{-1} respectively, showing that the time-depth conversion was accurate, with GPR estimates only ~2.5% higher which is acceptable for the goals of this study. Indeed, spatial variations of density and human error in layer picking may result in further uncertainty, however the cumulative error of these sources is likely to be negligible (e.g. Sinisalo et al., 2013).

Once data were extracted from the GPR profiles and converted into depth and ultimately accumulation, data were loaded into ArcMap10.2 and interpolated for visualisation (Figure 36). Surface topography can influence accumulation magnitudes, as snow can be removed (deposited) on the stoss (lee) side of surface features. If these features are dynamic, changes through time are expected, thus the changes in annual accumulation maybe be related to annual changes in surface features. Whilst in the field no visible surface features were observed aside from very small snow ripples that were typically in the order of a few cm, satellite imagery reveals many surface features between ~0.5-1km in width. The following section focusses on the spatial variability and investigates the effect it may have on the accumulation record.

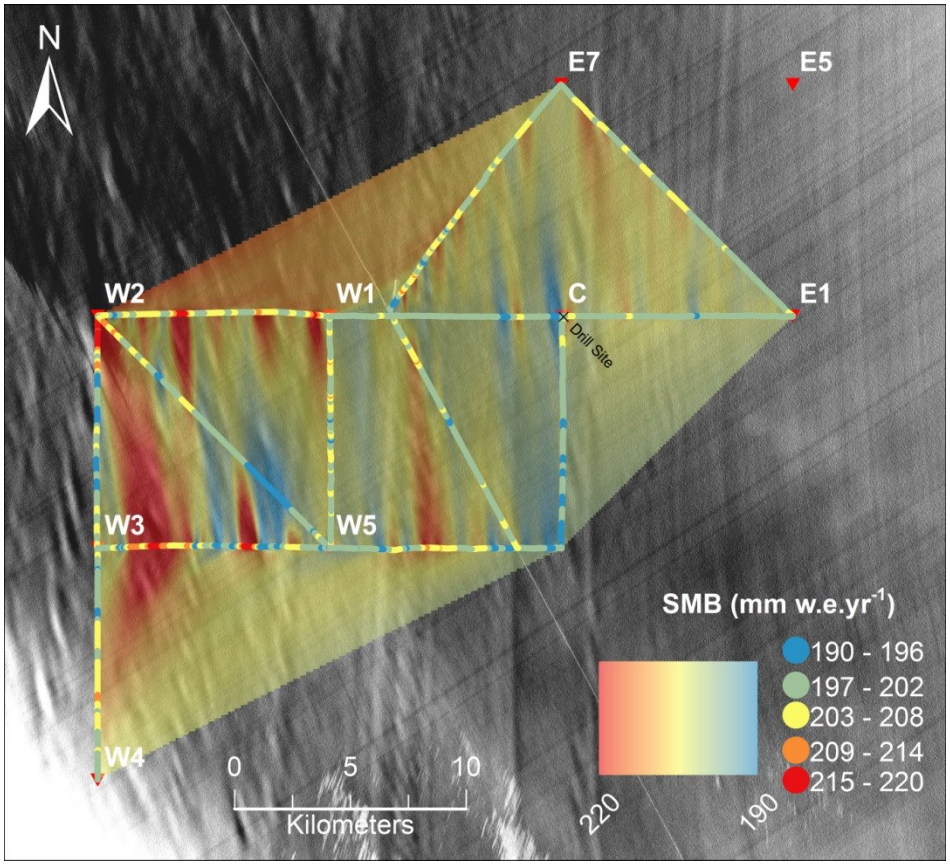

Figure 36: GPR profile interpolation showing spatial variability of accumulation. Interpolation was done using Natural Neighbour interpolation in ArcMap10.2, and Landsat 8 satellite imagery (panchromatic band) is used as the base layer. The thin white line is the South Pole traverse 'road'.

Figure 36 shows that the highest variability is in the west of the study region and appears to be associated with the increased surface roughness of that area, and not due to the expected snowfall gradient. These features do not appear to be caused by wind, but instead appear to originate flow lines that can be traced back to the grounding line. The flow stripes are defined as "topographic ridges or troughs with few-meter-scale relief, hundreds of meters to a few kilometres wide and tens to hundreds of kilometres long" (Fahnestock et al., 2000, page 654). There are multiple hypotheses on both the genesis and preservation of these flow lines, with the most likely hypothesis for ice shelves being the convergence of glacier tributaries of different velocities, resulting in shear margins between individual flow units (Glasser et al., 2015). Differential flow may continue downstream, preserving the flow lines, or flow lines may be transported passively. For the latter, it remains ambiguous how these features could persist on the surface after long time spans, especially in areas of high accumulation and wind. Another possibility is that these flow lines are the surface expression of vertical sheets of changed ice fabric (Glasser et al., 2015). Assuming hydrostatic equilibrium, they may also

be caused by the presence/absence of basal melting or basal crevasses/flowlines, potentially a result of subglacial landforms near the grounding line (Humbert & Steinhage, 2011). For the study region, differential flow is the most likely cause for at least some of the flow lines, as differential flow is evident based on MEaSUREs ice velocity data (Rignot et al., 2011b). A profile across the study area was taken from the MEaSUREs data, shown in Figure 37.

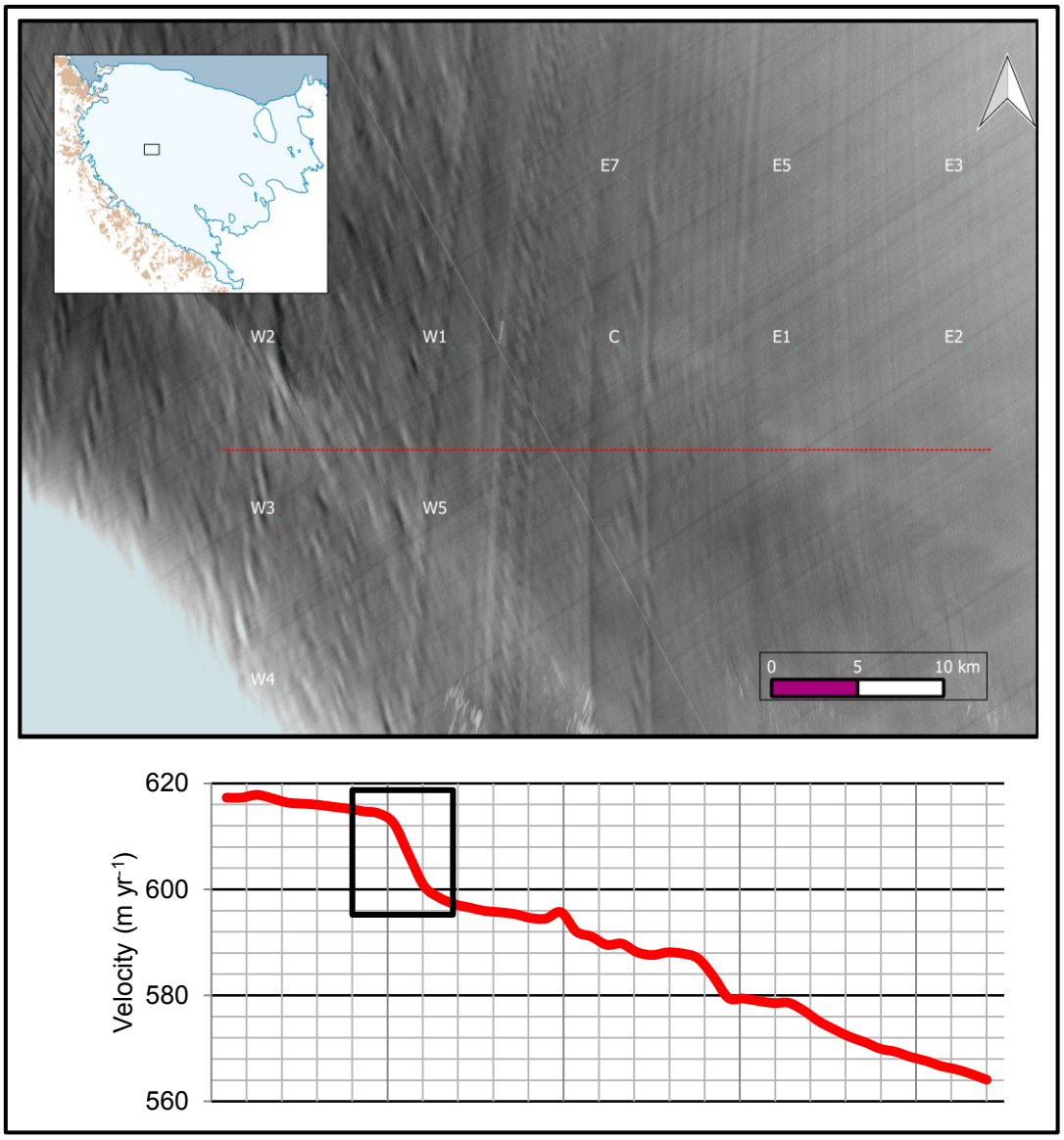

Figure 37: Velocity profile across the study area The figure demonstrates evidence for differential flow velocities, possibly maintaining the surface features. This is particularly evident in after the first ~10km from west to east (shown in the black box in the graph), where there is a steep drop in velocity of ~15m yr^{-1} over ~200m.

A comprehensive study on the genesis and preservation of these features is beyond the scope of this thesis. Nevertheless, it is observed that the features seen in western side of our study are features that can be traced back to the Shackleton and Liv Glaciers, whilst the features further east can be traced back to the Amundsen and Scott Glaciers. There is very little migration of these features in the GPR profiles, implying that they are not resultant of, or changing through time due to wind distribution of snow. It is possible that snow is preferentially deposited in the troughs, leading to faster densification due to the overbearing weight, and possibly, larger crystal size compared to windblown crests. As they become more pronounced with depth however (Figure 38), I suggest that these flow structures remain active (i.e. are not simply passively transported) and begin to influence firn morphology once it reaches a density where plastic deformation can occur (Maeno & Ebinuma, 1983).

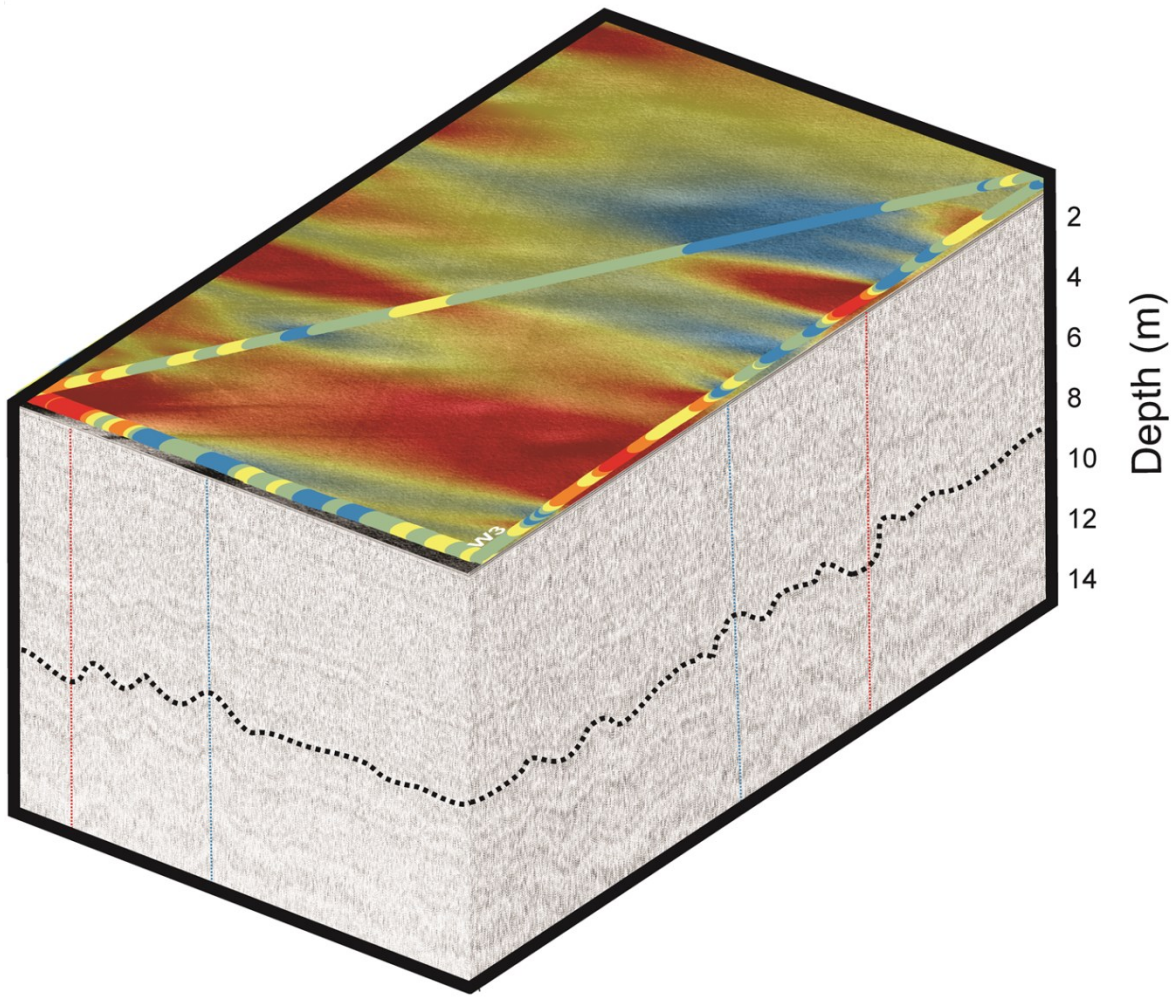

Figure 38: Schematic (not to scale) showing how internal layers relate to derived accumulation rates. Figure also shows how internal layers become more deformed and more pronounced with depth.

Whilst no flowline features were visible in the field (Figure 39), nor in the upper layers of the radargram, optical imagery is extremely sensitive to very subtle changes in surface slope, particularly on a very clean and reflective surface with a large solar incidence angle. Unfortunately, there are no sufficiently precise altitude data from the GNSS making it impossible to relate altitude to the surface features.

Figure 39: Image from W3 taken at 1:50pm, 29.11.2015, facing roughly north. Image demonstrates the lack of large surface features. Approximately 111° angle of view.

To help answer whether the spatial variability would influence the accumulation, a 3D map of the interpolation map from Figure 36 was generated (Figure 40). Based on velocity and age estimates, the isochrone originates ~11km south. Assuming that the spatial variability is stationary with time and that as the 'core site' moves northward it passes through the regions of higher and lower accumulation.

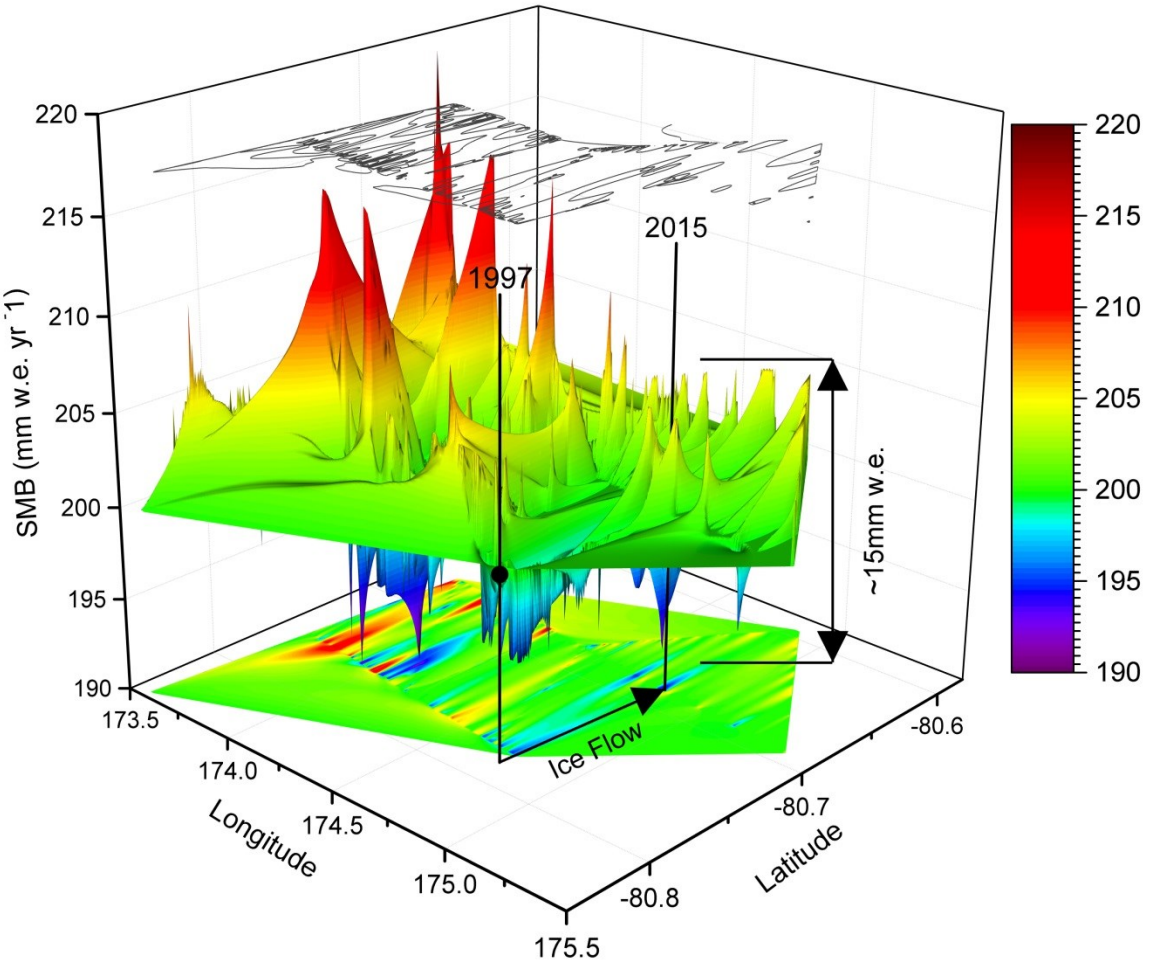

Figure 40: 3D plot of interpolation map presented in Figure 36, with projection on the base and 3mm w.e. contours above. Most of the variability is concentrated in the western region of the study area. 2015 indicates the location of the core site, and 1997 is an estimate of when the isochrone was on the surface.

From Figure 40, it is unlikely that spatial variability had much influence on the observed temporal variability. Even with the assumption that the variability is constant with time, the maximum spatial variability (surrounding the core site) is in the order of only 15mm, whilst we see differences of >300mm year-to-year to the same depth as the isochrone. Indeed, worth mentioning is the uncertainty associated with interpolation of point measurements. As the variability is caused by features ~0.5-1km in width, interpolating over areas of ~50km^2 doesn't represent reality. In this regard, it is assumed that the variability within the interpolated areas is of the same magnitudes as the observed in the GPR profiles. In any case, the maximum variability is concentrated in the west where features are aligned in a NNW-SSE orientation and are far more frequent, whilst there are fewer and smaller features in the eastern region of our study area.

4.1 Summary

This chapter has investigated the spatial variability of snow accumulation using Ground Penetrating Radar. Spatial variability was found to be over an order of magnitude smaller than the temporal variability, with maximum variability of ~15% within a 500km^2 area. GPR depth (accumulation) conversions were found to be accurate, with a difference of ~2.5% to the core derived accumulation at the core site. The spatial variability appears to be controlled by flow lines on the ice shelf, likely still active and possibly caused by the convergence of tributary glaciers or maintenance of subglacial features or basal crevasses. Despite the area being situated along a large snow accumulation gradient, no evidence was found in support of this. This is generally not surprising, as the total east-west profile distance was only ~30km, far too short to identify differences in snow accumulation caused by synoptic conditions. This chapter has shown that as spatial variability is small, temporal variations of net snow accumulation derived from the firn core must be the result of climatological and meteorological forcing, as discussed in chapter 5.

5 Climatological & Meteorological Controls on Snow Accumulation on the Ross Ice Shelf

5.1 Introduction

As Antarctic SMB is currently seemingly unaffected by anthropogenic forcing (Previdi & Polvani, 2016), it is necessary to understand the synoptic and natural climatic controls on year-to-year variations. Computing air mass trajectories is a method that can be used to estimate typical synoptic conditions and variability. They give an approximation of the path of air parcels over a given period of time (Crawford & Cohen, 2008), and can thus provide useful information on the source regions and transport pathways of precipitation to a given site (Scarchilli et al., 2011; Markle et al., 2012). Studying air mass trajectories can accordingly be of use in interpreting the influence of climatology on parameters such as snow accumulation. Now more than ever, it is imperative to understand baseline averages and variability in order to meaningfully assess future changes associated with climate change.

The use of cluster analysis on backwards air mass trajectories is one method of understanding the atmospheric transport mechanisms to a given site. In cluster analyses, trajectories that have similar transport speeds and directions are grouped together and are presumed to represent specific synoptic patterns (Hafner et al., 2007). Back trajectory analyses have been used in Antarctica to relate synoptic conditions to precipitation and ice core records (Schlosser et al., 2008; Fernandoy et al., 2012; Markle et al., 2012; Sinclair et al., 2013; Dittmann et al., 2016; Genthon et al., 2016). In this study, 3D back trajectories were created using the Hybrid Single Particle Lagrangian Integrated Trajectory (HYSPLIT) (version 4) model from the Air Research Laboratory at the National Oceanic and Atmospheric Administration (NOAA) (Draxler, 1999; Stein et al., 2015). HYSPLIT is one of the most widely used atmospheric transport models in the atmospheric science community, with one of the most common applications being back trajectory analyses (Stein et al., 2015).

5.2 Methods

Back trajectories were calculated for 120 hr (5-day) periods using NCEP/NCAR reanalysis (Kalnay et al., 1996), which has a spatial resolution of 2.5°. Trajectories begin at 12:00 UTC at 12-hour intervals, starting from January 1986 through December 2015 resulting in 21,912 trajectories. Model starting heights of 500m, 1,000m, and 1,500m above ground level (AGL) were tested to ensure representativeness. Trajectories for each starting height were spatially consistent, with very little variation, which is not surprising given the very thin boundary layer on the RIS. The model used in this study had a starting point of 500m AGL at our study site. Whilst others (Sinclair et al., 2010; Markle et al., 2012) have used higher starting levels, their study locations were immediately adjacent to the Trans-Antarctic mountains thus a higher starting point was required to remove the influence of topography. As HWDS2 is almost in the middle of the ice shelf, there is negligible surface roughness, and the boundary layer is thin, thus not significantly influencing trajectories. The model upper boundary was set to 10,000m AGL and the vertical motion method was set to data based.

Clustering techniques are used as a statistical tool to split large data sets into smaller, yet still distinct groups, with the goal of maximising within-group similarity whilst minimising between-group similarity (Kalkstein et al., 1987). HYSPLIT uses a *k*-means approach to its algorithm. The algorithm computes the Euclidean distance between each instance of a specific field and centres a series of predefined clusters, with the number of clusters (*k*)

defined by the user. The minimum Euclidean distance is achieved by including an instance into the cluster to which its Euclidean distance is lowest – a process that is repeated for every instance of the time series (Coggins, 2013). The entire routine is repeated multiple times so that instances can be moved between clusters if another clusters' centre is closer than the initial cluster in which they reside, and is continued until no instances are moved between clusters (Coggins, 2013). There is no correct number of clusters to identify (Christiansen, 2007); some methods exist to aid in deciding the amount, but it is ultimately up to the user and the goals of the study. In this regard, HYSPLIT provides a function to display the total spatial variance (the sum of all the cluster spatial variances, essentially the spatial difference between clusters) where, up to a certain value (k), the variance is large, and gradually decreases to a point where any additional clusters do not result in a large decrease in spatial variance. From this, six clusters would have seemed appropriate (Figure 41), however, this amount seemed to group together meteorologically different pathways (e.g. average height through the path and the velocity of the systems) that were spatially similar. Opposed to using statistical methods to identify a 'correct' number of clusters, an arbitrary k value of 20 was chosen to minimise the dimensionality of the data set whilst still capturing most of the synoptic air mass pathways, as per Markle et al. (2012). Computational limitations meant that the entire 30-year period of trajectories was clustered at 36-hour resolution at 12-hour intervals along each trajectory. Markle et al. (2012) created clusters at 48hr resolution for a 30-year period near the Byrd Glacier, and found that little information is lost when clustering at this resolution compared to 24-hour clustering resolution.

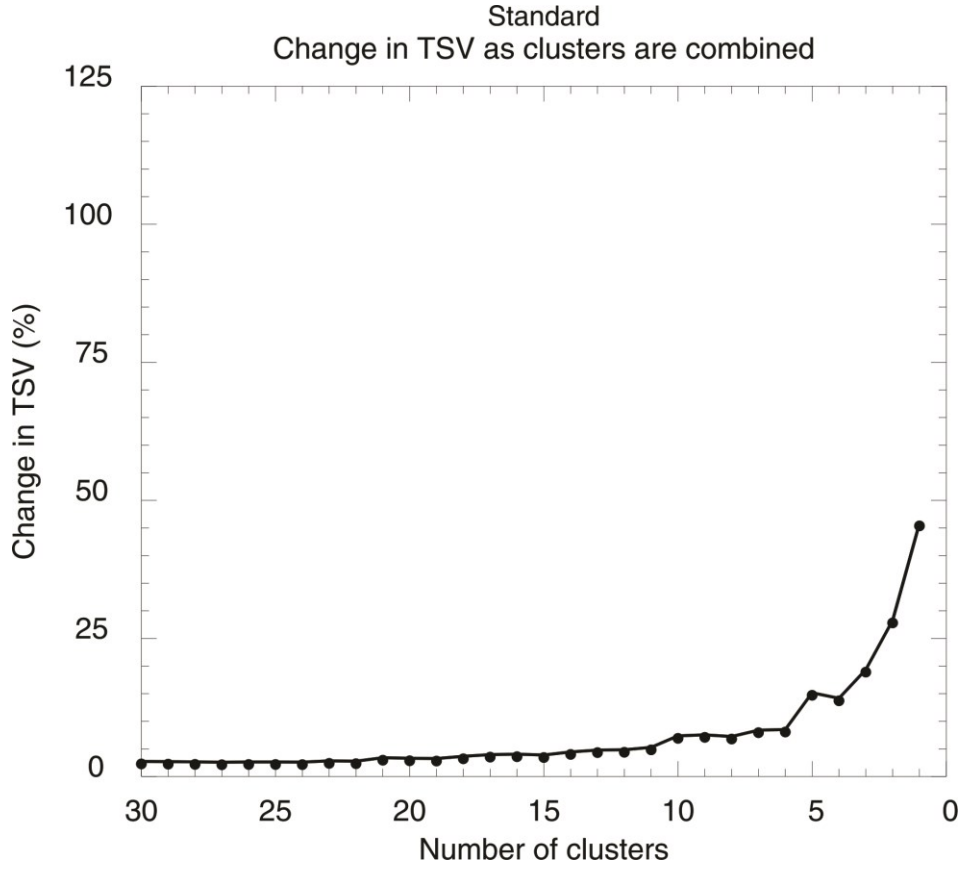

Figure 41: Total Spatial Variance produced from HYSPLIT. Once six clusters are used, the spatial variance with increasing clusters changes very little. However, whilst spatial similarity may be minimised, substantial meteorological differences often still exist.

NCEP/NCAR was chosen as it has been shown to give excellent results in the Ross Sea region (Sinclair et al., 2010; Markle et al., 2012). Further, Markle et al. (2012) found in a sensitivity test that ERA-Interim and ERA-40 gave similar results to NCEP/NCAR at both monthly and annual timescales. Spatial uncertainties limit the time span of the back trajectory (Schlosser et al., 2008; Scarchilli et al., 2011), but 5-day trajectories are generally sufficient for the identification of synoptic pathways (Dittmann et al., 2016).

5.3 Results & Discussion

A total of 20 clusters for 1986-2015 were subdivided further into five classifications based on region (Table 5). The trajectories were then plotted in ArcMap10.2 for clarity (Figure 42). All correlations and significance determinations are based on the same methodology presented on page 44.

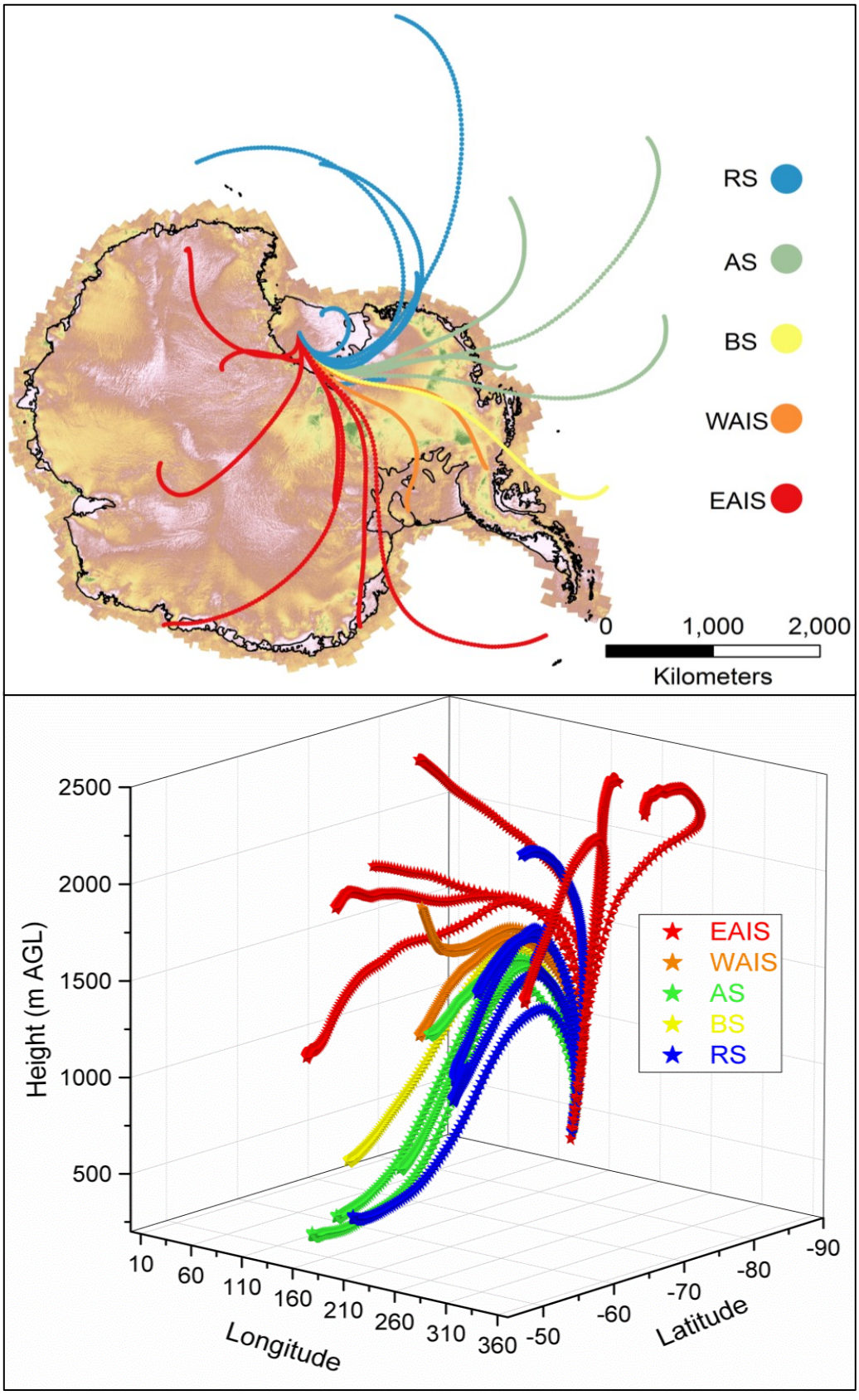

Figure 42: Top) mean trajectories from the 1986-2015 cluster analysis showing the pathways, colour coded to show the five sub-classification and Bottom) the mean trajectory altitudes over the course of the trajectory in meters above ground level. RS = Ross Sea, AS = Amundsen Sea, BS = Bellingshausen Sea, EAIS = East Antarctic Ice Sheet, WAIS = West Antarctic Ice Sheet

Table 5: Broad scale classifications and sub classifications & their associated frequencies over the 1986-2015 time-period

Classification	Sub-Classification	% of total
Oceanic (59%)	Ross Sea (RS)	39%
	Amundsen Sea (AS)	15%
	Bellingshausen Sea (BS)	5%
Continental (41%)	East Antarctic Ice Sheet (EAIS)	27%
	West Antarctic Ice Sheet (WAIS)	15%

The oceanic group accounted for 59% of all trajectories, most of which are fast moving, cyclonic flows originating in the Ross, Amundsen, and Bellingshausen Seas. There are two distinct cyclonic clusters that are clearly visible – those originating from the Ross Sea (RS), and those from the Amundsen Sea (AS). The RS trajectories are the most variable in terms of speed, with some slower moving trajectories confined by the RIS or nearby Marie Byrd Land. The majority however, originate to the north or north-west of the RIS, and traverse over Marie Byrd Land to the east of the ice shelf, before a northward flow toward the RS again. The AS and Bellingshausen Sea (BS) trajectories are also fast moving systems, with the AS trajectories often crossing over the Pine Island Bay sector before traversing the WAIS where they too, begin a northerly flow towards the RS.

The continental group accounted for 41% of all trajectories, with much higher altitudes than the oceanic group due to the height of the continent itself, and the anticyclonic nature of the air masses. The continental air masses are variable in both speed and nature, with some exhibiting typical anticyclonic features and some with typical cyclonic features.

It is worth noting that these results are quite similar to those of Markle et al. (2012), who found that oceanic and continental air masses accounted for 57.4% and 42.6% of all trajectories, respectively.

Both seasonal and annual variations in trajectory frequencies are also observed (Figure 43 & Figure 44). RS trajectories peak in January, and gradually decrease in frequency, with a marked decrease in September, before increasing again in October. AS trajectories exhibit slight bi-model peaks (May and September), with a minimum in January. Oceanic trajectories peak in April, and exhibit two other peaks in July and October, and naturally, continental air masses are simply the opposite of oceanic air masses, as the sum of both in any month is 100%. These seasonal variations are readily explained by the Semiannual Oscillation (SAO) (Van Loon, 1967), where during the spring and autumn, the circumpolar trough contracts towards the continent as a result of seasonal differences in temperature gradients between Antarctica and the mid latitudes. The results of the RS trajectories in particular, are remarkably different to the results of Markle et al. (2012). Despite having almost the same total frequencies for RS trajectories (38.2% compared to 39% for this study), their study revealed a peak in RS trajectories in April and a minima in December. This is likely a result of differing locations, slightly different model parameters and different manual classification techniques.

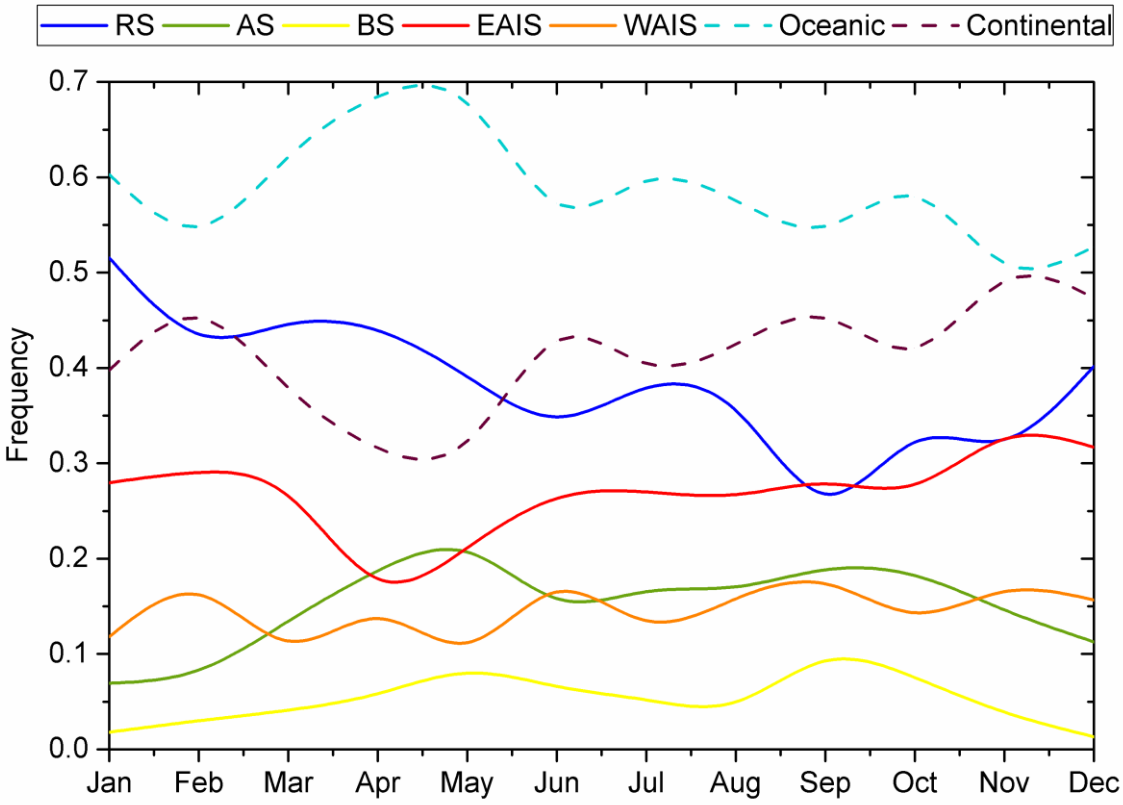

Figure 43: Monthly trajectory frequencies of all groups for the period 1986-2015

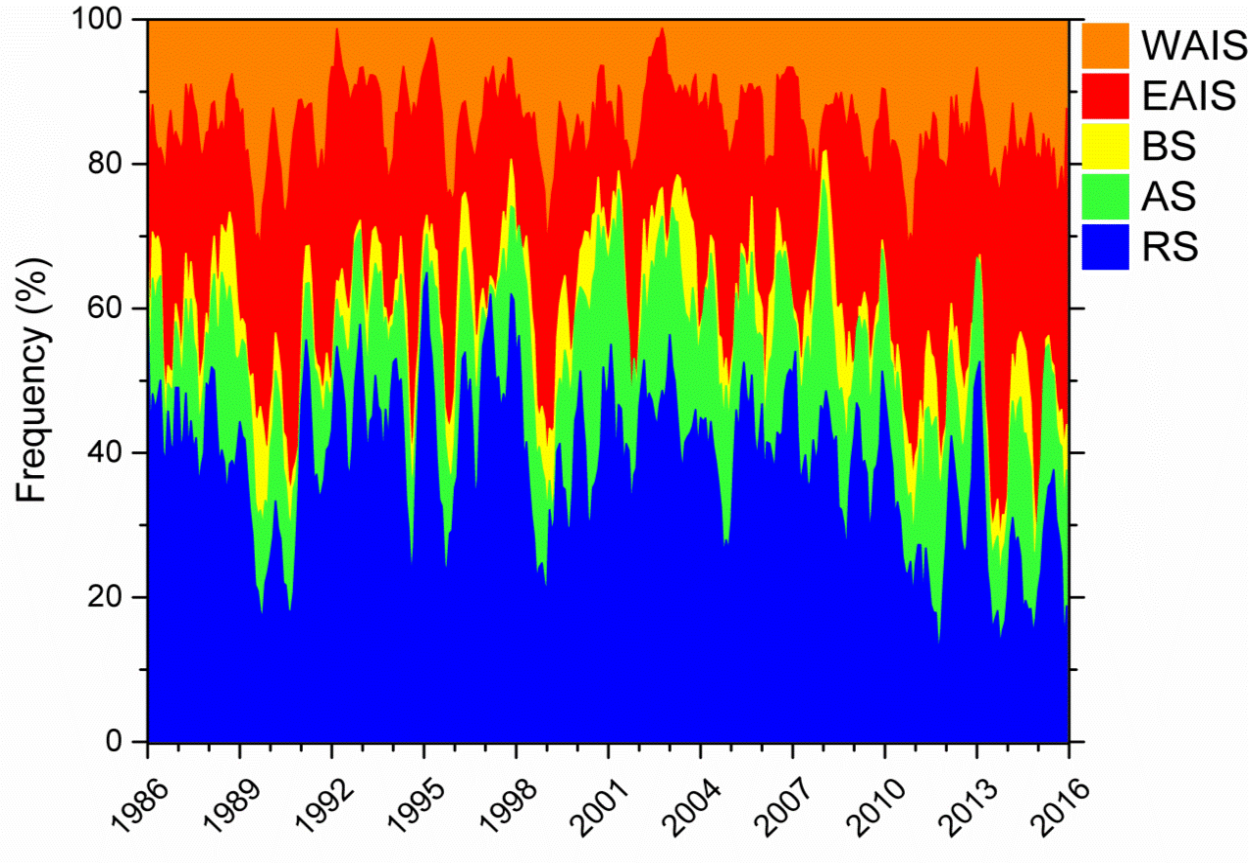

Figure 44: Stacked frequency plot of trajectory frequencies through time for the 1986-2015 period. To reduce noise, data were smoothed over a 3-month moving window.

Annually, there is much variation with some years showing substantially higher/lower frequencies of all trajectory types. Based on visual assessment, similar results were found by Markle et al. (2012), with general patterns in agreement in both data sets.

It was expected that the El Niño Southern Oscillation (ENSO), represented by the Southern Oscillation Index (SOI), would significantly influence accumulation rates; however, on an annual basis no relationship was found. This is due to the highly variable nature of the SOI, where annual averages are not necessarily representative. A threshold value for the SOI was also tested, where monthly values between -1 and +1 were removed, although this did not improve correlations.

Following Markle et al. (2012), by removing the mean annual cycles for each trajectory type, the multi-year variability is emphasized. The term, Non-Seasonal (hereafter NS), used synonymously with anomaly, refers to a time series with the monthly mean of all years 1986-2015 subtracted from each individual month.

Opposed to direct comparisons of the SOI and accumulation, monthly NS trajectories are compared with the monthly SOI index. As the aim of this study is to focus on climatological

controls on precipitation, continental air mass trajectories are not examined, as they are unlikely to deliver significant quantities of precipitation to the study site. A 5-month smoothing was applied to data due to the large variability exhibited, and to help account for the variable lag (typically ~3 months) of the SOI signal in Antarctica (e.g. Smith & Stearns, 1993; Fogt & Bromwich, 2006). A significant moderate negative correlation ($r=-0.433$, $p<0.05$) exists between the SOI and the NS RS trajectories (Figure 45), and a weak, but statistically significant ($r=0.275$, $p<0.05$) correlation exists between NS AS trajectories. No significant correlations between trajectories and the SAM were found, likely because the SAM is highly variable and acts on a predominately meridional shift that is far more zonally symmetric around the continent than the SOI, which displays a particularly focussed anomaly in the Pacific sector. A multivariate regression using both the SOI and SAM was also tested, but weaker relationships were found with trajectories that the SOI alone.

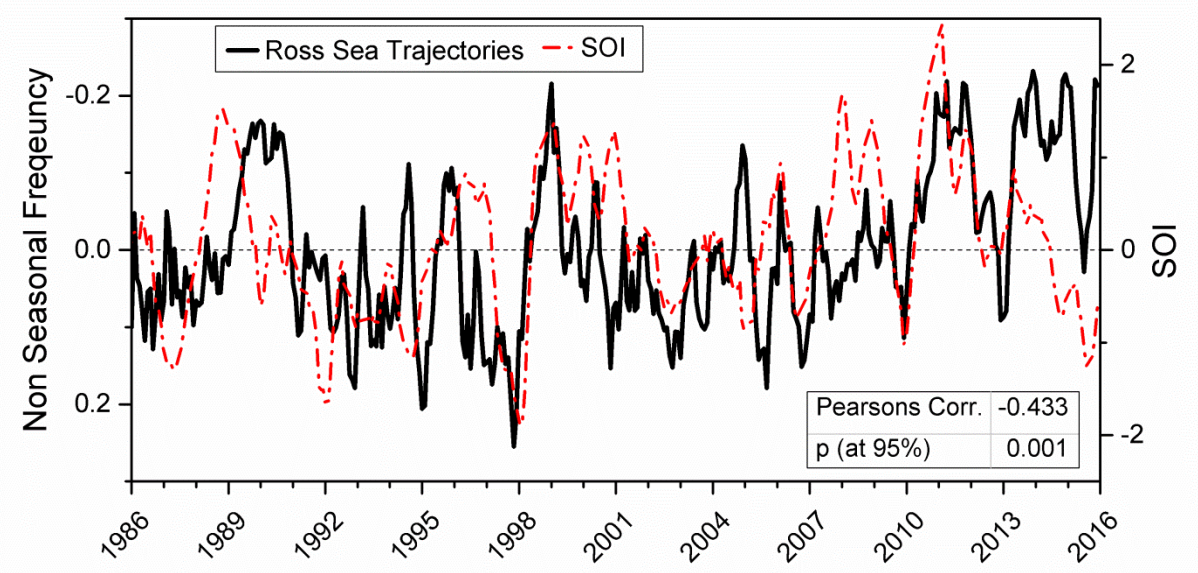

Figure 45: Monthly Non-Seasonal Ross Sea Trajectories and Southern Oscillation Index A 5-month smoothing is applied to data. Note the reversed x-axis for the Non-Seasonal Frequency. SOI data retrieved from https://www.ncdc.noaa.gov/teleconnections/enso/indicators/soi/.

Generally, there is good agreement with the frequency of RS trajectories and the SOI, although in some cases (e.g. the 1988-89 La Niña or the 2015 El Niño) there appears to be a lag in the ENSO signal, potentially due to the out of phase (positive) SAM which dampens the effect of ENSO teleconnections (Gregory & Noone, 2008). It is also important to remember that the Ross Sea is a climatological low-pressure centre, despite the phase of the SOI and natural variability in weather systems still influencing these results.

These results largely echo those found by Markle et al. (2012), which is not surprising given the similar location techniques used. Cohen et al. (2013) also found strong negative correlations between L-R (Low-Ross) conditions (refer to Figure 13 in section 2.1.2) and the SOI, except for the winter months. The negative correlation between RS trajectories and the SOI is explained by the influence of the ENSO on the pressure systems in the southern ocean, particularly the Amundsen Sea Low (Turner et al., 2013) (refer to section 2.1.1). During La Niña years (positive SOI) trajectories from the AS sector are more frequent and conversely, during El Niño years (negative SOI) trajectories from the RS sector are more frequent, associated with the weaker ASL centre and shift in the position of the low.

Whilst no link between annual accumulation and the annual SOI was found, a strong correlation ($r=0.63$, $p<0.01$) between annual NS RS trajectories and accumulation was found (Figure 46), implying that air masses originating from the Ross Sea deliver the majority of annual snowfall at HWDS2.

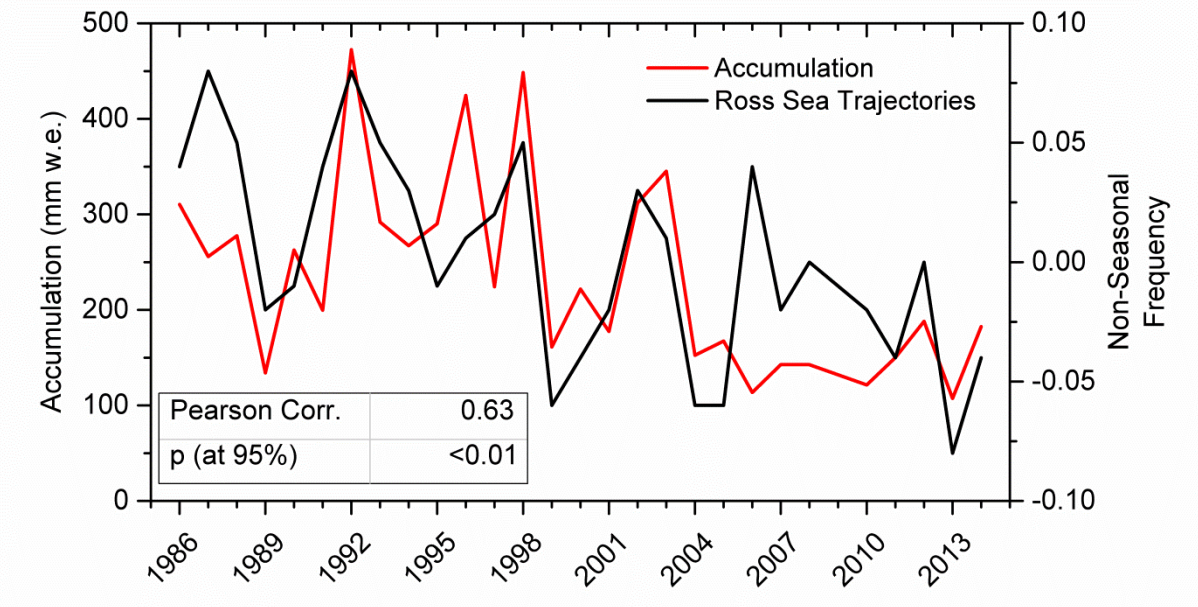

Figure 46: Annual accumulation and Ross Sea Non-Seasonal Trajectory frequencies.

It is perhaps not surprising that RS air masses deliver the most precipitation: these air masses are generally confined to the RIS due to the large topographic barrier of the Trans-Antarctic Mountains (TAMs). Similarly, as they do not traverse the WAIS, no topographic barrier exists to 'block' to the snowfall as would be the case with AS trajectories (i.e. King & Turner, 1997, page 110). Conversely, one of the reasons the RIS receives far less

accumulation than most of the Antarctic coast is *because* of the lack of topography, limiting precipitation induced by orographic lift (King & Turner, 1997).

In an attempt to confirm these findings, Lana Cohen (pers. comm. 2016) has kindly supplied synoptic classification data for the Ross Sea region (Cohen et al., 2013). A significant correlation ($r=0.416$, $p<0.05$) was found between annual accumulation and annual frequencies of type L-R synoptic class, supporting these results. Despite the issues associated with sub annual dating, as discussed in chapter 3, average monthly d-excess and snow accumulationvalues were strongly and moderately correlated with average monthly RS trajectory frequencies ($r=0.733$ and 0.390, respectively, $p<0.05$; Figure 47 & Figure 48)

The *d*-excess signal shows distinct seasonality that closely aligns with the RS trajectory frequencies. There are two potential drivers for this. One possibility is that RS trajectories in the summer travel greater distances, resulting in higher *d*-excess values; the other being the warmer summer temperatures resulting in lower relative humidity, which, in turn, leads to higher *d*-excess values. The *d*-excess was also weakly, but statistically significantly correlated ($r=0.288$, $p<0.05$) with the SAM, concurrent with the meridional shifts of pressure systems associated with changes in the SAM.

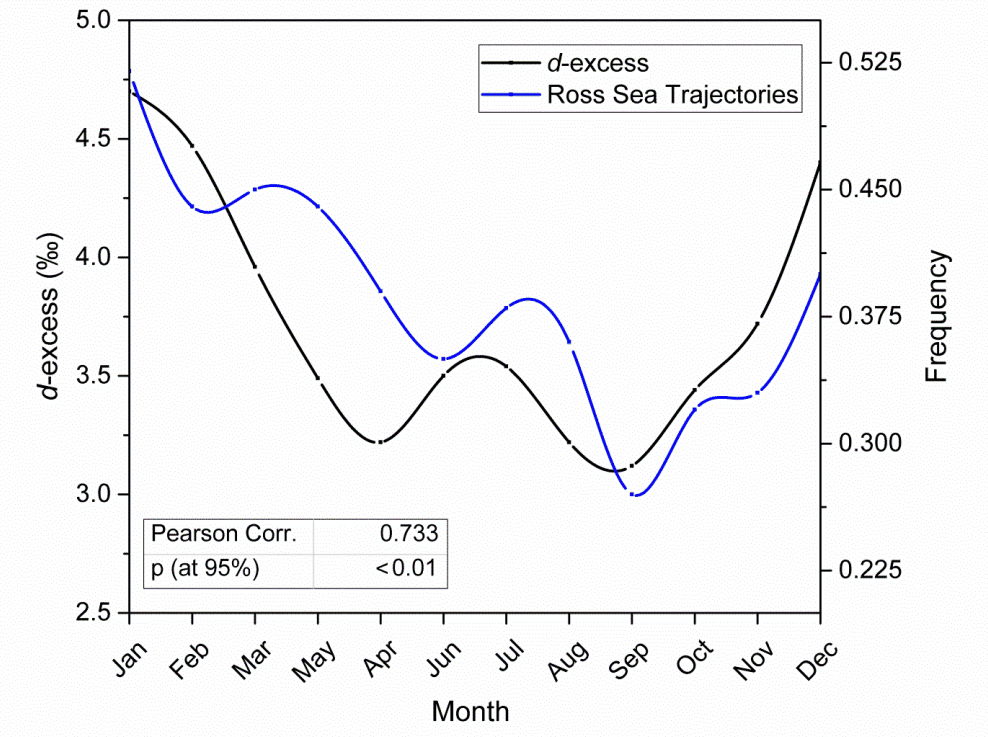

Figure 47: Average monthly *d*-excess values and average monthly Ross Sea Trajectory frequencies. The agreement between *d*-excess and trajectory frequencies further implies that most precipitation is delivered via air masses originating in the Ross Sea.

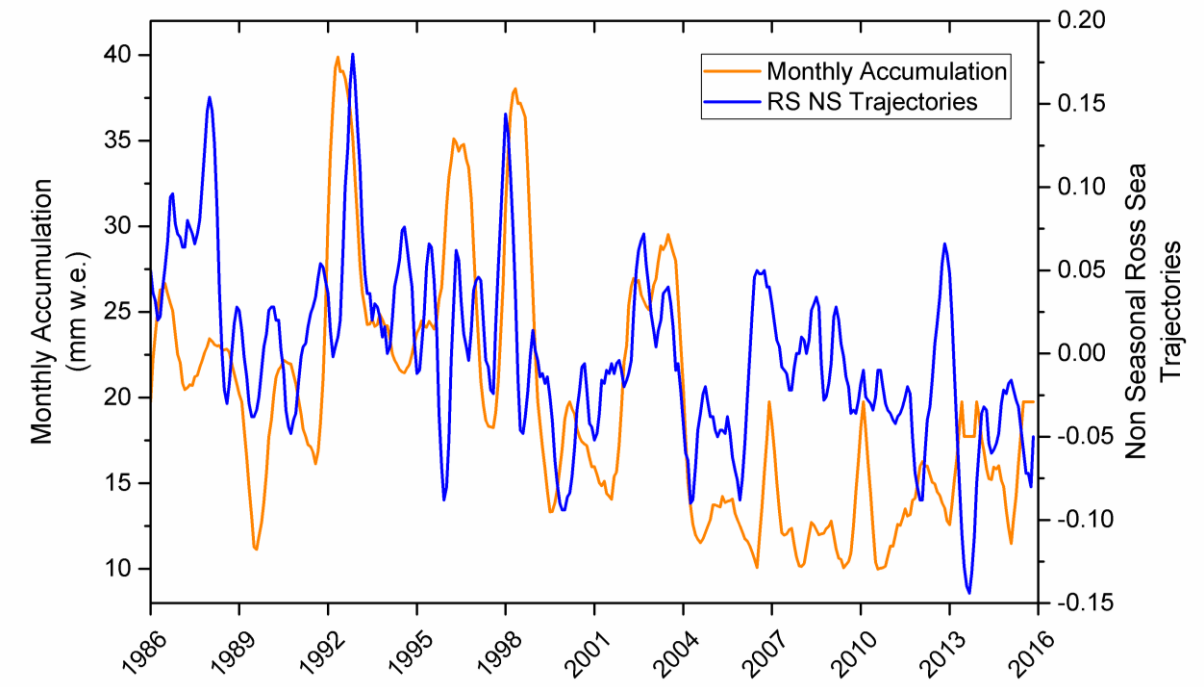

Figure 48: Monthly Non-Seasonal Ross Sea trajectories (blue) and monthly snow accumulation (orange). The relationship is stronger during more 'extreme' years. Both variables have a 5-month smoothing applied.

Due to its modulation of the ENSO, another potential driver of snowfall variability is the Interdecadal Pacific Oscillation (IPO) – a long-term oscillation of the Pacific Ocean (Salinger et al., 2001). During positive IPO phases, warm SST's dominate the North Pacific coast of North America, accompanied by colder SST's in the central North Pacific, and vice versa during negative phases. It has recently been shown by Meehl et al. (2016) that the IPO may influence Antarctic sea ice concentration, consistent with changes in other phenomena such as the ASL and 850hPa v-component winds that may influence precipitation regimes. A significant correlation ($r=0.45$, $p<0.05$) with accumulation and the IPO is observed, but as the IPO operates on 20-30 year time scales, the accumulation time series of 32 years is insufficient for any absolute certainty. A longer time series is required to be able to compare with full cycles of the IPO, which was in a negative phase 1946-1977.

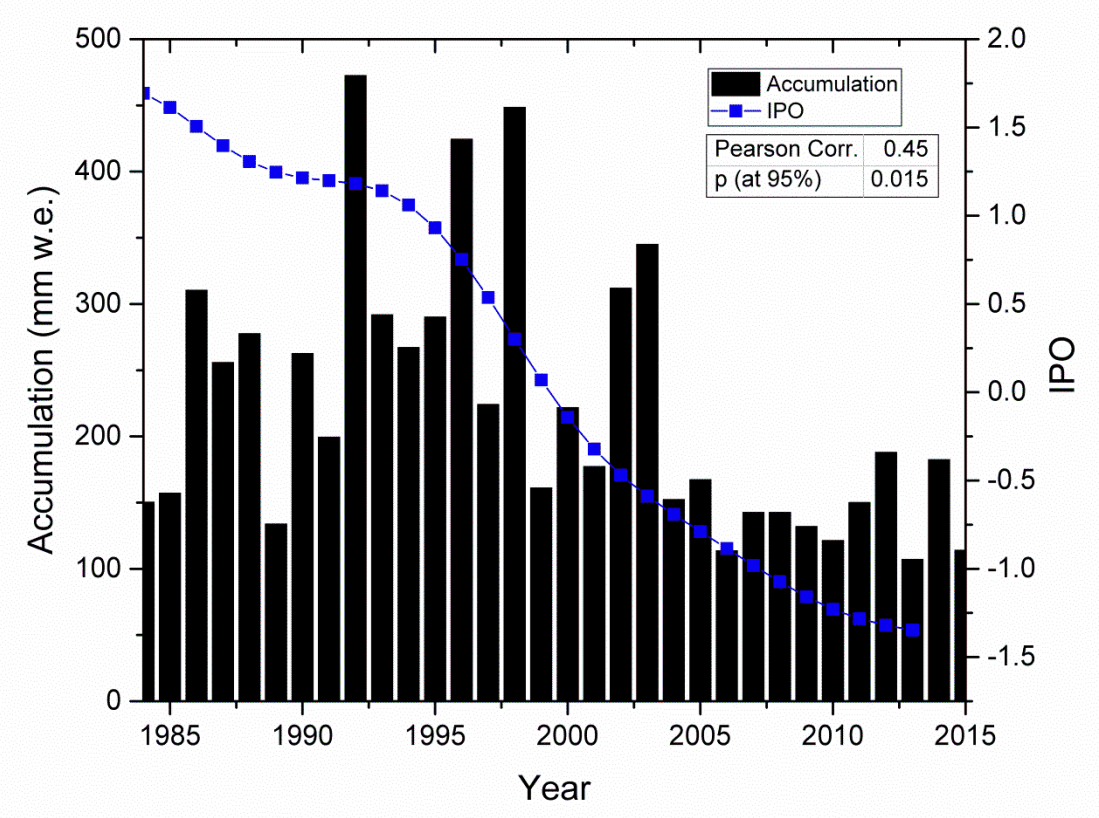

Figure 49: Annual accumulation and Interdecadal Pacific Oscillation for 1984-2015. IPO data (1984-2013) downloaded from https://data.govt.nz/dataset/show/4807

5.4 Summary

This chapter has identified the dominant synoptic pathways of air masses to HWDS2 by means of a back trajectory analysis using HYSPLIT. There is distinct seasonality of synoptic conditions, and significant year-to-year variability, much of which can be explained by the El Niño Southern Oscillation. The frequency of air masses originating from the Ross and Amundsen Seas appears to be largely influenced by the ENSO. The annual accumulation is not correlated to the annual SOI, but is strongly correlated to the annual Non-Seasonal Ross Sea trajectory frequencies. This result is supported with data from previous work in the region (Cohen et al., 2013), and the *d*-excess signal. There is evidence that the IPO may influence accumulation on the RIS, which is not surprising given its influence on the ENSO, however the time series is too short for any meaningful conclusions. The coarse spatial and temporal resolution of both NCEP reanalysis data and trajectory clustering, respectively, are potential limitations, thus it is suggested that future studies make use of multiple meteorological products (e.g. ERA-Interim) and higher temporal resolution clustering when possible. This approach is limited by the fact that a large proportion of precipitation is likely associated with mesoscale cyclones, blowing snow, and from isolated clouds that are well

removed from synoptic systems (King & Turner, 1997), which at this stage are not captured in climate models. Given the strong correlation of Ross Sea trajectories and accumulation, the use of back trajectories as a proxy for accumulation appears useful, however additional information such as the SOI and local conditions are required. Indeed, synoptic classification is inherently simplifying the complex processes associated with precipitation. A substantial proportion of the snow accumulation on the RIS is likely due to mesoscale storms and wind redistributed snow, neither of which can be represented by synoptic classifications. Further complicating is the influence of sea ice and other phenomena such as the Semiannual Oscillation and Antarctic Circumpolar Wave. Whilst synoptic classification aids in interpreting the dominant flow paths and the likely precipitation source regions, snow accumulation remains a complex strongly influenced by processes other than synoptic events.

6 SYNTHESIS, CONCLUSIONS & FUTURE WORK

Since the late 1970's, there have been no comprehensive surface mass balance studies on the Ross Ice Shelf, and available data has been collected over periods of only 1-2 years and are thus not representative of long term averages. With global atmospheric CO_2 having now surpassed 400ppm, the stability of the Ross Ice Shelf in a warming globe has been questioned, forming the basis of this research.

There is unequivocal evidence of global climate change (IPCC, 2014), and understanding how the Antarctic has responded, and will respond to this change is of paramount importance. There remain marked gaps in our knowledge of precipitation regimes in Antarctica, but as spatial and temporal coverage improves, so will our estimates of the Antarctic surface mass balance. The research presented in this thesis has explored the annual accumulation for a 32-year period at a site close to the middle of the Ross Ice Shelf, and the drivers behind spatial and temporal variations in accumulation have been investigated using a variety of techniques.

The future behaviour of the Ross Ice Shelf is critically important for the stability of the marine based West Antarctic Ice Sheet. The only way to predict future ice shelf and ice sheet behaviour is through the use of sophisticated modelling (Naish et al., 2009; Pollard & DeConto, 2009; Kuipers Munneke et al., 2014; Pollard et al., 2015; DeConto & Pollard, 2016). Accurate modelling, however, requires accurate input parameters such as net snow accumulation rates, which are atmospherically coupled to models in the form of regional

climate models (DeConto & Pollard, 2016). Past measurements and modelled accumulation rates for areas near HWDS of ~90-150mm w.e. yr^{-1} (Thomas et al., 1984; Arthern et al., 2006; Van de Berg et al., 2006; Dee et al., 2011; Favier et al., 2013; Van Wessem et al., 2014) were found to be underestimated, which in turn, may have important implications for the input parameters of ice shelf models. The RIS exhibits a strong gradient of snow accumulation, with a 'tongue' of low accumulation rates extending from the Siple Coast to the middle of the ice shelf (e.g. Figure 15, page 29), a result of the general atmospheric circulation of the region and the effect of the TAMs (Sinclair et al., 2010; Markle et al., 2012; Coggins et al., 2014). No gradient was resolved over the short distance of the GPR profiles used in this study, as small-scale topography dominated the variability. Thus, it becomes impossible to confirm if indeed such a large accumulation gradient exists and longer east-west profiles, coupled with an array of deeper dated firn cores/internal layers, are required.

Previous studies have shown marked impacts of SAM and the ENSO teleconnection in the Ross Sea/Ross Ice Shelf regions (Salinger et al., 2001; Bertler et al., 2004; Turner, 2004; Fogt & Bromwich, 2006; Stammerjohn et al., 2008; Markle et al., 2012; Cohen et al., 2013; Costanza et al., 2016). In terms of snow accumulation, the SAM and ENSO were expected to have significant impacts (Cohen et al., 2013), and storms from the Ross and Amundsen Seas were thought to deliver the majority of annual net snowfall (Sinclair et al., 2010; Markle et al., 2012; Cohen et al., 2013). In this study, however, no evidence of a SAM signal in annual net snow accumulation was found, but strong evidence of an ENSO signal through its modulation of cyclonic pathways in the Ross and Amundsen Seas was observed. Whilst storms from the Amundsen Sea sector likely contribute to annual net accumulation, this study has found that storms from the Ross Sea are more important for snowfall on the Ross Ice Shelf.

I have found that annual net snow accumulation is markedly higher than previously thought for our study site (chapter 3) and that spatial variability in snow accumulation is comparatively small and is influenced by flow features on the ice shelf (chapter 4). I have also found that air masses from the Ross Sea, modulated by the ENSO, likely deliver the majority of precipitation to HWDS2 (chapter 5). This research has provided findings that form the basis for future work on the Ross Ice Shelf with respect to measuring and monitoring snow accumulation. Specifically, this thesis has provided findings for the following questions:

1. What is the temporal variability of accumulation near our study site, and can atmospheric models accurately predict snow accumulation in this area?

Chapter 3 addresses this question through an analysis of a 16m firn core and a numerical assessment of RACMO2.3 and ERA-Interim climate models. The firn core analysis was based on identifying summer maxima and winter minima in the isotope signal, coupled with density data allowing for accurate dating and conversion into snow water equivalent per year. It was expected, based on previous measurements, that a 16m firn core would cover a time series as far back as the 1970's, however, this study found annual mean accumulation to be approximately twice that of previous studies at 222 mm w.e. yr^{-1}, resulting in a shorter time series of 32 years (1984-2015). Large annual variability was also observed, with a range of 365mm w.e., implying that the previous measurements taken over only 1-2 year periods might not have captured long-term accumulation rates during that period. A weak, yet statistically significant decreasing trend in annual accumulation was found, but is possibly a result of the large interannual variability exhibited and short time series. In order to confidently assess any trends, a longer time series is required in both future (monitoring) and past (deeper firn cores) directions. In this regard, a 5m deeper core (~20m) would likely allow for measurements at this location to overlap with those taken as part of the RIGGS project in the 1970's.

The stable isotope profile was highly variable, with some sections showing perfectly preserved seasonal signals and some showing very poorly resolved and anomalous signals. Unfortunately, due to the inability of accurate sub-annual dating, attributing these anomalies to any particular event was not possible. These anomalies served as a limitation to the technique, so a variety of additional techniques and 'guiding' methods were adopted. All techniques led to a similar result however, asserting a high degree of confidence to the findings of this study. Even if eight annual layers were 'missed' in this analysis (bringing the time series up to 40 years), average annual accumulation would still be ~175mm w.e. yr^{-1}. This is still considerably higher than previous estimates, from both in-situ measurements and model outputs. Further, snowpit/firn core stratigraphy exhibited no relationship to the isotope signal. A comprehensive snowpit analysis of snow morphology, temperature and density might provide useful stratigraphy information beyond visible observations. Making use of near-infrared photography of snowpit stratigraphy would also be insightful in identifying event-based layers (Tape et al., 2010), which may exhibit a relationship with δ or *d*-excess

values. As sub-annual dating was based on linear equidistance interpolations between summer and winter maxima and minima, the uncertainty is inherently high, posing a challenge for *d*-excess and anomaly interpretations. In this regard, major and trace element chemistry would be useful dating tools for use alongside a stable isotope profile (e.g. Legrand & Mayewski, 1997; Goktas et al., 2002; Vallelonga et al., 2004; Hur et al., 2007; Bull, 2009). Finally, real-time, event based precipitation sampling would be incredibly useful to ascertain a local δ-temperature relationship, aid in source region identification and intra-storm variability (e.g. Cohen, 2013), and to investigate post depositional modification of both the physical and chemical properties of snow.

Assuming that the firn core derived accumulation was accurate, the performance of climate models, RACMO2.3 and ERA-Interim, were numerically tested using the refined Index of Agreement (Willmott et al., 2012) which gives results on a 0-1 scale, where anything above ~0.5 represents decent model performance (Cai et al., 2000). Both were found to be poor predictors of snow accumulation in this area, with an Index of Agreement of 0.17. Whilst RACMO2.3 captured the overall patterns of snowfall reasonably well, it failed to accurately predict the magnitude of snow accumulation. The Ross Ice Shelf is known to have a complex accumulation regime, with windblown snow and mesoscale cyclones likely to contribute greatly to the annual SMB (Bromwich, 1988, 1991; Carrasco & Bromwich, 1994; Carrasco et al., 2003; Knuth et al., 2010; Sinclair et al., 2010; Cohen et al., 2013). Neither of these, however, are accurately captured in climate models, even with higher spatial resolution.

The work in chapter 3 demonstrated that mean annual net accumulation was estimated to be twice as high as from previous in-situ observations and model outputs. This has substantial implications for the overall mass balance of the Ross Ice Shelf, and more spatially and temporally comprehensive observations are required over the ice shelf to determine if these results are anomalous, or if there is indeed higher snowfall over the entire ice shelf. As a ground based study, the results from this analysis may also be used as a ground truth for airborne missions such as the NSF ROSETTA project. To expand the point measurement (core) to a wider area, the use of ground penetrating radar was incorporated which allowed for investigating the second research question:

2. What is the spatial variability of accumulation near our study site, and what are the drivers?

Chapter 4 investigates the question by an analysis of ~150km of ground penetrating radar profiles, satellite imagery, and ice shelf velocity. A 500MHz GPR was used to expand the point measurement to a wider region around the core site. Very few strong internal reflectors meant that the only isochronous reflector was at a depth of ~9m, which was dated to 18.25 years based on results from chapter 3. Due to the lack or major reflectors in the snow pack, future studies should pilot the use of 1000MHz radar – whilst this will reduce the penetration depth, it may help to resolve finer internal layers with more clarity. Conversely, if a deeper core is retrieved and dated, lower frequency radar (e.g. 400MHz) may be capable of resolving deeper internal layers (T. Scambos, *pers. comm.*, 2016). Two-way travel times were accurately converted to depth based on modelled density fit to empirical data thus the radar derived accumulation rates are accurate. Spatial variability was small compared to temporal variability to the same depth, with variabilities of <20mm w.e. and >300mm w.e., respectively, implying that spatial variability could not be responsible for anomalous years of high/low accumulation found in the core.

Spatial variability is related to surface features visible in satellite imagery that are in the order of 0.5-1km in width. Ice shelf velocity data provides evidence that the surface features are a result of differential flow, and appear to be traced as far back as the grounding line where the Shackleton and Liv glaciers flow into the ice shelf. A future investigation into the genesis and preservation of these flowlines would be useful, particularly investigating their changes through time. Spatial variability within the extent of this study region is likely due to non-climatic process, such as described above, and it is unlikely that spatial variability caused by flowlines and wind distributed snow has any major implications for the overall mass balance if averaged out over the entire ice shelf. Whilst the study site is in a region of a considerable snow accumulation gradient, there is no evidence suggesting that the eastern (western) region receives less (more) snowfall, which is not surprising given the east-west extent of only 30km. Future work involving GPR depends on the study goals; if the aim is to investigate finer scale variations in the SMB, then a denser grid of GPR profiles is necessary to avoid interpolations over large areas. However, as I have shown that temporal variations greatly exceed spatial variations, it seems intuitive to complete a broader scale study over a wider geographical extent to determine the large-scale spatial variability.

As spatial variation could not explain the huge temporal variability, an investigation into the climatological and meteorological controls on snow accumulation formed the third research question:

3. What are the main climatic drivers of temporal variability, and how does synoptic variability influence snow accumulation?

Through a back trajectory and cluster analysis for 1986-2015, as presented in chapter 5, the dominant synoptic pathways to HWDS2 were identified, along with temporal variations in these pathways. By spatially classifying 20 trajectory clusters, it was possible to determine the influence of the southern oscillation index on the monthly frequency of each trajectory, and the influence of annual trajectory frequencies and annual snow accumulation derived from the firn core. Distinct seasonal and annual variations in each cluster type were found, and the frequency of Ross Sea and Amundsen Sea air masses were modulated largely by the ENSO (represented by the SOI). This influence is explained through the impact of the ENSO on the intensity and location of the Amundsen Sea Low and pressure anomalies in the Ross Sea. Amundsen Sea trajectories were more frequent during La Niña years, where the low is substantially deeper. Conversely, Ross Sea trajectories were more frequent during El Niño years, and were found to be a significant driver of snow accumulation at HWDS2. Annual Non-Seasonal (i.e. anomalous) Ross Sea air mass trajectories were highly correlated with annual accumulation, providing evidence that the majority of precipitation at HWDS2 is sourced from the Ross Sea. The finding was supported by the average monthly *d*-excess record, which was significantly correlated Ross Sea trajectory frequencies, as well as a previous study from the Ross Sea region (Cohen et al., 2013). Synoptic classification inherently simplifies the complex processes associated with precipitation, thus future work could potentially make use of various, higher spatial resolution meteorological products (e.g. ERA-Interim), higher temporal resolution clustering techniques, and making use of a precipitation filter (i.e. only investigating trajectories that result in precipitation). Monitoring precipitation events in-situ and computing back trajectories for days of known snowfall would be an excellent method of unambiguously determining the dominant synoptic pathways resulting in snowfall. The use of back trajectory analyses as proxies for snow accumulation is indeed possible, and there is potential for the SOI to be used as a proxy for both trajectories and accumulation. The SAM showed no correlation with any trajectory type. The Interdecadal Pacific Oscillation also exhibited a significant correlation with

accumulation which is to be expected given its modulation of the ENSO, but as the IPO operates on 20-30 year time scales, a longer time series of accumulation is required for a meaningful comparison.

It must be stressed that the snow accumulation regime on the Ross Ice Shelf is incredibly complex, with intricate interactions between topography, katabatic winds, warm oceanic air, mesocyclones, and synoptic scale cyclones. Whilst this research has demonstrated that the magnitude net snow accumulation at HWDS2 is higher than previously believed, the exact drivers of exhibited spatiotemporal variations require further research. Significant proportions of snow accumulation are likely associated with mesoscale cyclones (Bromwich, 1991; Carrasco & Bromwich, 1994; Carrasco et al., 2003; Sinclair et al., 2010) and wind-blown snow (Bromwich, 1988; Knuth et al., 2010), neither of which were accounted for in this study.

This research has unambiguously shown that annual net accumulation at HWDS2 is higher than previous estimates. Given the importance of the Ross Ice Shelf, particularly in a warming world, this research has provided a justification for more a comprehensive investigation into snow accumulation across the entire ice shelf, which should form the basis of a future study.

7 REFERENCES

Agosta, C., Fettweis, X., & Datta, R. (2015). Evaluation of the CMIP5 models in the aim of regional modelling of the Antarctic surface mass balance. *The Cryosphere, 9*, 2311-2321. doi: 10.5194/tc-9-2311-2015

Alley, R., Bolzan, J., & Whillans, I. (1982). Polar firn densification and grain growth. *Annals of Glaciology, 3*, 7-11.

Allison, I., Alley, R., Fricker, H., Thomas, R., & Warner, R. (2009). Ice sheet mass balance and sea level. *Antarctic Science, 21*(05), 413-426. doi: 10.1017/S0954102009990137

Anderson, D. Z., Frisch, J. C., & Masser, C. S. (1984). Mirror reflectometer based on optical cavity decay time. *Applied optics, 23*(8), 1238-1245.

Arcone, S. (1996). High resolution of glacial ice stratigraphy: a ground-penetrating radar study of Pegasus Runway, McMurdo Station, Antarctica. *Geophysics, 61*(6), 1653-1663. doi: 10.1190/1.1444084

Arcone, S., Spikes, V., Hamilton, G., & Mayewski, P. (2004). Stratigraphic continuity in 400 MHz short-pulse radar profiles of firn in West Antarctica. *Annals of Glaciology, 39*(1), 195-200. doi: 10.1190/1.1444084

Arnason, B. (1981). Ice and Snow Hydrology. In J. R. Gat & R. Gonfiantini (Eds.), *Deuterium and Oxygen-18 in the Water Cycle* (pp. 143-175). Vienna: IAEA.

Arnaud, L., Barnola, J. M., & Duval, P. (2000). Physical modeling of the densification of snow/firn and ice in the upper part of polar ice sheets. *Annals of Glaciology, 26*, 39-44.

Arthern, R. J., Winebrenner, D. P., & Vaughan, D. G. (2006). Antarctic snow accumulation mapped using polarization of 4.3-cm wavelength microwave emission. *Journal of Geophysical Research: Atmospheres, 111*(D06). doi: 10.1029/2004JD005667

Benn, D., & Evans, D. (1998). *Glaciers and Glaciation*. London: Arnold.

Bennett, M., & Glasser, N. (2011). *Glacial geology: ice sheets and landforms*. West Sussex: John Wiley & Sons.

Bentley, C. R. (1984). The Ross Ice Shelf Geophysical and Glaciological Survey (RIGGS): introduction and summary of measurements performed *Antarctic Research Series, American Geophysical Union, 42*, 1-20.

Bentley, C. R., Clough, J. W., Jezek, K. C., & Shabtaie, S. (1979). Ice-thickness patterns and the dynamics of the Ross Ice Shelf, Antarctica. *Journal of Glaciology, 24*, 287-294. doi: 10.3198/1979JoG24-90-287-294

Berden, G., & Engeln, R. (2009). *Cavity Ring-Down Spectroscopy: Techniques and Applications*. Chichester: John Wiley & Sons.

Bertler, N., Barrett, P., Mayewski, P., Fogt, R., Kreutz, K., & Shulmeister, J. (2004). El Nino suppresses Antarctic warming. *Geophysical Research Letters, 31*(15). doi: 10.1029/2004GL020749

Bertler, N., Naish, T., Oerter, H., Kipfstuhl, S., Barrett, P., Mayewski, P., & Kreutz, K. (2006). The effects of joint ENSO-Antarctic oscillation forcing on the McMurdo Dry Valleys, Antarctica. *Antarctic Science, 18*(4), 507-514. doi: 10.1017/S0954102006000551

Brand, W., Coplen, T., Vogl, J., Rosner, M., & Prohaska, T. (2014). Assessment of international reference materials for isotope-ratio analysis (IUPAC Technical Report). *Pure and Applied Chemistry, 86*(3), 425-467. doi: 10.1515/pac-2013-1023

Bretherton, C. S., Widmann, M., Dymnikov, V. P., Wallace, J. M., & Bladé, I. (1999). The effective number of spatial degrees of freedom of a time-varying field. *Journal of Climate, 12*(7), 1990-2009. doi: 10.1175/1520-0442(1999)012%3C1990:TENOSD%3E2.0.CO;2

Bromwich, D. (1988). Snowfall in high southern latitudes. *Reviews of Geophysics, 26*(1), 149-168. doi: 10.1029/Rg026i001p00149

Bromwich, D. (1991). Mesoscale cyclogenesis over the southwestern Ross Sea linked to strong katabatic winds. *Monthly weather review, 119*(7), 1736-1753. doi: 10.1175/1520-0493(1991)119<1736:Mcotsr>2.0.Co;2

Bromwich, D., Carrasco, J., & Stearns, C. (1992). Satellite Observations of Katabatic-Wind Propagation for Great Distances across the Ross Ice Shelf. *Monthly weather review, 120*(9), 1940-1949. doi: 10.1175/1520-0493(1992)120<1940:SOOKWP>2.0.CO;2

Bromwich, D., Nicolas, J., & Monaghan, A. (2011). An assessment of precipitation changes over Antarctica and the Southern Ocean since 1989 in contemporary global reanalyses. *Journal of Climate, 24*(16), 4189-4209. doi: 10.1175/2011JCLI4074.1

Bull, J. (2009). *Stable isotope, major and trace element chemistry of modern snow from Evans Piedmont Glacier, Antarctica: insights into potential source regions and relationship of glaciochemistry to atmospheric circulation and vigour.* (MSc.), Victoria University of Wellington, Wellington.

Cai, X., Hourston, R., & Steyn, D. (2000). A numerical study of meteorological conditions during pacific '93. *Atmosphere-Ocean, 38*(3), 457-479. doi: 10.1080/07055900.2000.9649656

Calkin, P. E. (1995). Global Glacial Chronologies and Causes of Glaciation. In J. Menzies (Ed.), *Modern glacial environments: processes, dynamics, and sediments* (Vol. 1). Oxford: Butterworth-Heinemann Ltd.

Carrasco, J., & Bromwich, D. (1994). Climatological aspects of mesoscale cyclogenesis over the Ross Sea and Ross Ice Shelf regions of Antarctica. *Monthly weather review, 122*(11), 2405-2425. doi: 10.1175/1520-0493(1994)122<2405:CAOMCO>2.0.CO;2

Carrasco, J., Bromwich, D., & Monaghan, A. (2003). Distribution and Characteristics of Mesoscale Cyclones in the Antarctic: Ross Sea Eastward to the Weddell Sea. *Monthly weather review, 131*, 289-301. doi: 10.1175/1520-0493(2003)131<0289:DACOMC>2.0.CO;2

Catania, G., Hulbe, C., & Conway, H. (2010). Grounding-line basal melt rates determined using radar-derived internal stratigraphy. *Journal of Glaciology, 56*(197), 545-554. doi: 10.3189/002214310792447842

Catania, G., Hulbe, C., Conway, H., Scambos, T. A., & Raymond, C. (2012). Variability in the mass flux of the Ross ice streams, West Antarctica, over the last millennium. *Journal of Glaciology, 58*(210), 741-752. doi: 10.3189/2012JoG11J219

Christiansen, B. (2007). Atmospheric circulation regimes: Can cluster analysis provide the number? *Journal of Climate, 20*(10), 2229–2250. doi: 10.1175/JCLI4107.1

Church, J., Gregory, J., Huybrechts, P., Kuhn, M., Lambeck, K., Nhuan, M., . . . Woodworth, P. (2001). Changes in sea level. *Climate Change 2001: The Scientific Basis*, J. Houghtonet al., Eds., Cambridge University Press, 639–693.

Ciais, P., White, J., Jouzel, J., & Petit, J. (1995). The origin of present-day Antarctic precipitation from surface snow deuterium excess data. *Journal of Geophysical Research: Atmospheres, 100*(D9), 18917-18927. doi: 10.1029/95JD01169

Clausen, H., & Dansgaard, W. (1977). *Less surface accumulation on the Ross Ice Shelf than hitherto assumed*, in Oeschger, H., ed.,Proceedings UGGI Symposium on Isotopes and Impurities in Snow and Ice, Grenoble. *IAHS Publication*(118), 172.

Coggins, J. H. (2013). *Studies of the meteorology and climatology of Ross Island and theRoss Ice Shelf, Antarctica.* (PhD), University of Canterbury, Canterbury.

Coggins, J. H., McDonald, A. J., & Jolly, B. (2014). Synoptic climatology of the Ross Ice Shelf and Ross Sea region of Antarctica: k-means clustering and validation. *International journal of climatology, 34*(7), 2330-2348. doi: 10.1002/joc.3842

Cohen, L. (2013). *Atmospheric Variability and Precipitation in the Ross Sea Region, Antarctica.* (PhD), Victoria University of Wellington, Wellington.

Cohen, L., Dean, S., & Renwick, J. (2013). Synoptic weather types for the Ross Sea region, Antarctica. *Journal of Climate, 26*(2), 636-649. doi: 10.1175/Jcli-D-11-00690.1

Copland, L., & Sharp, M. (2001). Mapping thermal and hydrological conditions beneath a polythermal glacier with radio-echo sounding. *Journal of Glaciology, 47*(157), 232-242. doi: 10.3189/172756501781832377

Costanza, C. A., Lazzara, M. A., Keller, L. M., & Cassano, J. J. (2016). The surface climatology of the Ross Ice Shelf Antarctica. *International journal of climatology*, n/a-n/a. doi: 10.1002/joc.4681

Craig, H. (1961). Isotopic variations in meteoric waters. *Science, 133*(3465), 1702-1703.

Craig, H., & Gordon, L. (1965). Deuterium and oxygen-18 variations in the ocean and marine atmosphere, Stable Isotopes. in Oceanic Studies and Paleotemperatures *Lab. Geol. and Nuclear Sci., Pisa, Italy*, 9-130.

Crary, A., Robinson, E. S., Bennett, H. F., & Boyd, W. W. (1962). Glaciological regime of the Ross ice shelf. *Journal of Geophysical Research, 67*(7), 2791-2807.

Crawford, J., & Cohen, D. (2008). HYSPLIT back trajectories for potential source contribution function studies of trans boundary pollution episodes *Institute for Environmental Research Technical Note*.

Cuffey, K. M., & Paterson, W. S. B. (2010). *The physics of glaciers* (4 ed.). Amsterdam: Academic Press.

Daniels, D. J. (2004). *Ground penetrating radar* (2 ed. Vol. 1). London: Institution of Electrical Engineers.

Dansgaard, W. (1964). Stable isotopes in precipitation. *Tellus A, 16*(4), 436-468.

Dansgaard, W., Johnsen, S., Clausen, H., & Gundestrup, N. (1973). Stable Isotope Glaciology. *Meddelelser om Groenland, 197*(2).

De Angelis, H., & Skvarca, P. (2003). Glacier surge after ice shelf collapse. *Science, 299*(5612), 1560-1562. doi: 10.1126/science.1077987

DeConto, R. M., & Pollard, D. (2016). Contribution of Antarctica to past and future sea-level rise. *Nature, 531*(7596), 591-597. doi: 10.1038/nature17145

Dee, D. P., Uppala, S. M., Simmons, A. J., Berrisford, P., Poli, P., Kobayashi, S., . . . Vitart, F. (2011). The ERA-Interim reanalysis: configuration and performance of the data assimilation system. *Quarterly Journal of the Royal Meteorological Society, 137*(656), 553-597. doi: 10.1002/qj.828

Delaney, A., Arcone, S., O'Bannon, A., & Wright, A. (2004, 21-24 Jun). *Crevasse detection with GPR across the Ross Ice Shelf, Antarctica.* Paper presented at the Intemational Conference on Ground Penetrating Radar.

Déry, S. J., & Yau, M. (2002). Large-scale mass balance effects of blowing snow and surface sublimation. *Journal of Geophysical Research: Atmospheres, 107*(D23), ACL 8-1-ACL 8-17. doi: 10.1029/2001JD001251

Dittmann, A., Schlosser, E., Masson-Delmotte, V., Powers, J., Manning, K., Werner, M., & Fujita, K. (2016). Precipitation regime and stable isotopes at Dome Fuji, East Antarctica. *Atmospheric Chemistry and Physics Discussions, 16*, 6883-6900. doi: 10.5194/acp-16-6883-2016

Draxler, R. (1999). HYSPLIT4 User's Guide. NOAA Tech. Memo. ERL ARL-230, NOAA Air Resources Laboratory, Silver Spring, MD.: Md.

Dunse, T., Eisen, O., Helm, V., Rack, W., Steinhage, D., & Parry, V. (2008). Characteristics and small-scale variability of GPR signals and their relation to snow accumulation in Greenland's percolation zone. *Journal of Glaciology, 54*(185), 333-342. doi: 10.3189/002214308784886207

Eisen, O., Frezzotti, M., Genthon, C., Isaksson, E., Magand, O., Van den Broeke, M., . . . Kameda, T. (2008). Ground-based measurements of spatial and temporal variability of snow accumulation in East Antarctica. *Reviews of Geophysics, 46*(2). doi: 10.1029/2006rg000218

Ekaykin, A., Eberlein, L., Lipenkov, V., Popov, S., Scheinert, M., Schröder, L., & Turkeev, A. (2016). Non-climatic signal in ice core records: lessons from Antarctic megadunes. *The Cryosphere, 10*(3), 1217-1227. doi: 10.5194/tc-10-1217-2016

Ekaykin, A., Lipenkov, V., Barkov, N., Petit, J., & Masson-Delmotte, V. (2002). Spatial and temporal variability in isotope composition of recent snow in the vicinity of Vostok station, Antarctica: implications for ice-core record interpretation. *Annals of Glaciology, 35*(1), 181-186. doi: 10.3189/172756402781816726

Engeset, R., Sorteberg, H., & Udnaes, H. (2000). *Snow pillows: use and verification.* Paper presented at the Proceedings of the Fourth International Conference on Snow Engineering.

Faber, A. K., Vinther, B. M., Sjolte, J., & Pedersen, R. A. (2016). How does sea ice influence δ18O of Arctic precipitation? *Atmospheric Chemistry and Physics Discussions, 2016*, 1-22. doi: 10.5194/acp-2016-100

Fahnestock, M., Scambos, T., Bindschadler, R., & Kvaran, G. (2000). A millennium of variable ice flow recorded by the Ross Ice Shelf, Antarctica. *Journal of Glaciology, 46*(155), 652-664. doi: 10.3189/172756500781832693

Fassnacht, S. R. (2004). Estimating Alter-shielded gauge snowfall undercatch, snowpack sublimation, and blowing snow transport at six sites in the coterminous USA. *Hydrological Processes, 18*(18), 3481-3492. doi: 10.1002/hyp.5806

Favier, V., Agosta, C., Parouty, S., Durand, G., Delaygue, G., Gallée, H., . . . Krinner, G. (2013). An updated and quality controlled surface mass balance dataset for Antarctica. *The Cryosphere, 7*(2), 583-597. doi: 10.5194/tc-7-583-2013

Fernandoy, F., Meyer, H., Oerter, H., Wilhelms, F., Graf, W., & Schwander, J. (2010). Temporal and spatial variation of stable-isotope ratios and accumulation rates in the hinterland of Neumayer station, East Antarctica. *Journal of Glaciology, 56*(198), 673-687. doi: 10.3189/002214310793146296

Fernandoy, F., Meyer, H., & Tonelli, M. (2012). Stable water isotopes of precipitation and firn cores from the northern Antarctic Peninsula region as a proxy for climate reconstruction. *The Cryosphere, 6*(2), 313-330. doi: 10.5194/tc-6-313-2012

Fischer, H., Wagenbach, D., Laternser, M., & Haeberli, W. (1995). Glacio-meteorological and isotopic studies along the EGIG line, central Greenland. *Journal of Glaciology, 41*(139), 515-527. doi: 10.3198/1995JoG41-139-515-527

Fogt, R., & Bromwich, D. (2006). Decadal variability of the ENSO teleconnection to the high-latitude South Pacific governed by coupling with the Southern Annular Mode. *Journal of Climate, 19*(6), 979-997. doi: 10.1175/Jcli3671.1

Fretwell, P., Pritchard, H. D., Vaughan, D. G., Bamber, J., Barrand, N., Bell, R., . . . Casassa, G. (2013). Bedmap2: improved ice bed, surface and thickness datasets for Antarctica. *The Cryosphere, 7*(1), 375-393. doi: 10.5194/tc-7-375-2013

Frezzotti, M., Pourchet, M., Flora, O., Gandolfi, S., Gay, M., Urbini, S., . . . Proposito, M. (2004). New estimations of precipitation and surface sublimation in East Antarctica from snow accumulation measurements. *Climate Dynamics, 23*(7-8), 803-813. doi: 10.1007/s00382-004-0462-5

Frezzotti, M., Pourchet, M., Flora, O., Gandolfi, S., Gay, M., Urbini, S., . . . Proposito, M. (2005). Spatial and temporal variability of snow accumulation in East Antarctica from traverse data. *Journal of Glaciology, 51*(172), 113-124. doi: 10.3189/172756505781829502

Frieler, K., Clark, P., He, F., Buizert, C., Reese, R., Ligtenberg, S., . . . Levermann, A. (2015). Consistent evidence of increasing Antarctic accumulation with warming. *Nature Climate Change, 5*(4), 348-352. doi: 10.1038/nclimate2574

Froehlich, K., Gibson, J., & Aggarwal, P. (2001). *Deuterium excess in precipitation and its climatological significance.* Paper presented at the Study of environmental change using isotope techniques. International Atomic Energy Agency, Vienna.

Fudge, T. J., Markle, B. R., Cuffey, K. M., Buizert, C., Taylor, K. C., Steig, E. J., . . . Koutnik, M. (2016). Variable relationship between accumulation and temperature in West Antarctica for the past 31,000 years. *Geophysical Research Letters, 43*(8), 3795-3803. doi: 10.1002/2016GL068356

Fujita, K., & Abe, O. (2006). Stable isotopes in daily precipitation at Dome Fuji, East Antarctica. *Geophysical Research Letters, 33*(18), 1-4. doi: 10.1029/2006GL026936

Gat, J. R. (2005). Some Classical Concepts of Isotope Hydrology. In P. K. Aggarwal, J. R. Gat & K. F. Froehlich (Eds.), *Isotopes in the Water Cycle*. Dordrecht: Springer.

Gat, J. R. (2010). *Isotope hydrology: a study of the water cycle*. London: Imperial College Press.

Gat, J. R., & Carmi, I. (1970). Evolution of the isotopic composition of atmospheric waters in the Mediterranean Sea area. *Journal of Geophysical Research, 75*(15), 3039-3048. doi: 10.1029/JC075i015p03039

Gat, J. R., & Gonfiantini, R. (1981). *Stable isotope hydrology. Deuterium and oxygen-18 in the water cycle*. Vienna: International Atomic Energy Agency.

Genthon, C., & Krinner, G. (2001). Antarctic surface mass balance and systematic biases in general circulation models. *Journal of Geophysical Research: Atmospheres, 106*(D18), 20653-20664. doi: 10.1029/2001jd900136

Genthon, C., Six, D., Scarchilli, C., Ciardini, V., & Frezzotti, M. (2016). Meteorological and snow accumulation gradients across Dome C, East Antarctic plateau. *International journal of climatology, 36*(1), 455-466. doi: 10.1002/joc.4362

Giovinetto, M., & Zwally, H. (2000). Spatial distribution of net surface accumulation on the Antarctic ice sheet. *Annals of Glaciology, 31*(1), 171-178. doi: 10.3189/172756400781820200

Glasser, N., Jennings, S., Hambrey, M., & Hubbard, B. (2015). Origin and dynamic significance of longitudinal structures (" flow stripes") in the Antarctic Ice Sheet. *Earth Surface Dynamics, 3*(2), 239-249. doi: 10.5194/esurf-3-239-2015

Goktas, F., Fischer, H., Oerter, H., Weller, R., Sommer, S., & Miller, H. (2002). A glacio-chemical characterization of the new EPICA deep-drilling site on Amundsenisen, Dronning Maude Land. *Annals of Glaciology, 35*, 347-354.

Gong, D., & Wang, S. (1999). Definition of Antarctic Oscillation Index. *Geophysical Research Letters, 26*(4), 459-462. doi: 10.1029/1999gl900003

Gorodetskaya, I., Tsukernik, M., Claes, K., Ralph, M., Neff, W., & Van Lipzig, N. (2014). The role of atmospheric rivers in anomalous snow accumulation in East Antarctica. *Geophysical Research Letters, 41*(17), 6199-6206. doi: 10.1002/2014GL060881

Gregory, S., & Noone, D. (2008). Variability in the teleconnection between the El Niño–Southern Oscillation and West Antarctic climate deduced from West Antarctic ice core isotope records. *Journal of Geophysical Research: Atmospheres, 113*(D17). doi: 10.1029/2007JD009107

Hafner, W., Solorzano, N., & Jaffe, D. (2007). Analysis of rainfall and fine aerosol data using clustered trajectory analysis for National Park sites in the Western US. *Atmospheric Environment, 41*(14), 3071-3081. doi: 10.1016/j.atmosenv.2006.11.049

Hagen, J. O., & Reeh, N. (2004). Mass balance of the cryosphere. In J. L. Bamber & A. J. Payne (Eds.), *Mass Balance of the Cryosphere: Observations and Modelling Contemporary and Future changes.* (Vol. 1). Cambridge: Cambridge University Press.

Hanna, E., Navarro, F., Pattyn, F., Domingues, C., Fettweis, X., Ivins, E., . . . Tulaczyk, S. (2013). Ice-sheet mass balance and climate change. *Nature, 498*(7452), 51-59. doi: 10.1038/nature12238

Harper, J. T., & Bradford, J. H. (2003). Snow stratigraphy over a uniform depositional surface: spatial variability and measurement tools. *Cold Regions Science and Technology, 37*(3), 289-298. doi: 10.1016/S0165-232x(03)00071-5

Hawley, R. L., Courville, Z. R., Kehrl, L. M., Lutz, E. R., Osterberg, E. C., Overly, T. B., & Wong, G. J. (2014). Recent accumulation variability in northwest Greenland from ground-penetrating radar and shallow cores along the Greenland Inland Traverse. *Journal of Glaciology, 60*(220), 375-382. doi: 10.3189/2014JoG13J141

Heap, J. A., & Rundle, A. S. (1964). *Snow accumulation on the Ross Ice Shelf, Antarctica*.

Herbelin, J. M., & Mckay, J. A. (1981). Development of Laser Mirrors of Very High Reflectivity Using the Cavity-Attenuated Phase-Shift Method. *Applied optics, 20*(19), 3341-3344. doi: 10.1364/Ao.20.003341

Herron, M. M., & Langway, C. (1980). Firn densification: an empirical model. *Journal of Glaciology, 25*(93), 373-385. doi: 10.3198/1980JoG25-93-373-385

Hubbard, B., & Glasser, N. (2005). *Field techniques in glaciology and glacial geomorphology*. West Sussex: John Wiley & Sons.

Hughes, T. (1981). The Weak Underbelly of the West Antarctic Ice Sheet. *Journal of Glaciology, 27*(97), 518-525.

Humbert, A., & Steinhage, D. (2011). The evolution of the western rift area of the Fimbul Ice Shelf, Antarctica. *The Cryosphere, 5*(4), 931-944. doi: 10.5194/tc-5-931-2011

Hur, S., Cunde, X., Hong, S., Barbante, C., Gabrielli, P., Lee, K., . . . Ming, Y. (2007). Seasonal patterns of heavy metal deposition to the snow on Lambert Glacier basin, East Antarctica. *Atmospheric Environment, 41*, 8567-8578. doi: 10.1016/j.atmosenv.2007.07.012

Huybrechts, P., Steinhage, D., Wilhelms, F., & Bamber, J. (2000). Balance velocities and measured properties of the Antarctic ice sheet from a new compilation of gridded data for modelling. *Annals of Glaciology, 30*(1), 52-60. doi: 10.3189/172756400781820778

IPCC. (2001). Climate Change 2001: The Scientific Basis. Contribution of Working Group 1 to the Third Assessment Report of the Intergovernmental Panel on Climate Change , Cambridge Univ. Press, New York.

IPCC. (2014). Summary for Policymakers. In C. B. Field, V. R. Barros, D. J. Dokken, K. J. Mach, M. D. Mastrandrea, T. E. Bilir, M. Chatterjee, K. L. Ebi, Y. O. Estrada, R. C. Genova, B. Girma, E. S. Kissel, A. N. Levy, S. MacCracken, P. R. Mastrandrea & L. L. White (Eds.), *Climate Change 2014: Impacts, Adaptation, and Vulnerability. Part A: Global and Sectoral Aspects. Contribution of Working Group II to the Fifth Assessment Report of the Intergovernmental Panel on Climate Change* (pp. 1-32). Cambridge, United Kingdom, and New York, NY, USA: Cambridge University Press.

Johnsen, S. (1977). Stable isotope homogenization of polar firn and ice. *International Association of Hydrological Sciences Publication, 118*, 210-219.

Johnsen, S., Clausen, H., Cuffey, K., Hoffmann, G., Schwander, J., & Creyts, T. (2000). Diffusion of stable isotopes in polar firn and ice: the isotope effect in firn diffusion. *Physics of ice core records, 159*, 121-140.

Johnsen, S., Dansgaard, W., & White, J. (1989). The origin of Arctic precipitation under present and glacial conditions. *Tellus B, 41*(4), 452-468. doi: 10.1111/j.1600-0889.1989.tb00321.x

Jol, H. M. (2009). *Ground penetrating radar theory and applications*. Amsterdam, The Netherlands: Elsevier Science.

Joughin, I., Alley, R. B., & Holland, D. M. (2012). Ice-sheet response to oceanic forcing. *Science, 338*(6111), 1172-1176. doi: 10.1126/science.1226481

Jouzel, J., & Merlivat, L. (1982). Deuterium excess in an East Antarctic ice core suggests higher relative humidity at the oceanic surface during the last glacial maximum. *Nature, 299*(5885), 688-691. doi: 10.1038/299688a0

Jouzel, J., & Merlivat, L. (1984). Deuterium and oxygen 18 in precipitation: Modeling of the isotopic effects during snow formation. *Journal of Geophysical Research: Atmospheres, 89*(D7), 11749-11757. doi: 10.1029/JD089iD07p11749

Kalkstein, L., Tan, G., & Skindlov, J. (1987). An evaluation of three clustering procedures for use in synoptic climatological classification. *Journal of climate and applied meteorology, 26*(6), 717-730. doi: 10.1175/1520-0450(1987)026<0717:AEOTCP>2.0.CO;2

Kalnay, E., Kanamitsu, M., Kistler, R., Collins, W., Deaven, D., Gandin, L., . . . Joseph, D. (1996). The NCEP/NCAR 40-year reanalysis project. *Bulletin of the American Meteorological Society, 77*(3), 437-471. doi: 10.1175/1520-0477(1996)077<0437:Tnyrp>2.0.Co;2

Kerstel, E. R. T., Meijer, H.A.J. (2005). Optical Isotope Ratio Measurements in Hydrology. In P. K. Aggarwal, K. F. Froehlich & J. R. Gat (Eds.), *Isotopes in the water cycle*. Dodrecht: Springer.

Kidston, J., Renwick, J., & McGregor, J. (2009). Hemispheric-scale seasonality of the southern annular mode and impacts onthe climate of New Zealand. *Journal of Climate, 22*, 4759–4770.

King, J., & Turner, J. (1997). *Antarctic meteorology and climatology*. Cambridge: Cambridge University Press.

Klein, K. (2014). *Variability in dry Antarctic firn: Investigations on spatially distributed snow and firn samples from Dronning Maud Land, Antarctica.* (PhD), University of Bremen, Bremen.

Knuth, S. L., Tripoli, G. J., Thom, J. E., & Weidner, G. A. (2010). The Influence of Blowing Snow and Precipitation on Snow Depth Change across the Ross Ice Shelf and Ross Sea Regions of Antarctica. *Journal of Applied Meteorology and Climatology, 49*(6), 1306-1321. doi: 10.1175/2010JAMC2245.1

Kohler, J., Moore, J., Kennett, M., Engeset, R., & Elvehoy, H. (1997). Using ground-penetrating radar to image previous years' summer surfaces for mass-balance measurements. *Annals of Glaciology, 24*, 355-360.

Kotlyakov, V. (1966). *The Snow Cover of the Antarctic and Its Role in the Present Day Glaciation of the Continent*: Israel Program for scientific translations.

Kovacs, A., Gow, A. J., & Morey, R. M. (1995). The in-situ dielectric constant of polar firn revisited. *Cold Regions Science and Technology, 23*(3), 245-256.

Kruetzmann, N. (2013). *Analysis of Internal Boundaries and Transition Regions in Geophysical Systems with Advanced Processing Techniques.* (PhD Thesis), University of Canterbury, Christchurch.

Kruetzmann, N., Rack, W., McDonald, A., & George, S. (2011). Snow accumulation and compaction derived from GPR data near Ross Island, Antarctica. *The Cryosphere, 5*(2), 391-404.

Kuipers Munneke, P., Ligtenberg, S., Van den Broeke, M., & Vaughan, D. (2013). *Will Antarctic ice shelves survive atmospheric warming in the next two centuries?* Paper presented at the EGU General Assembly Conference Abstracts.

Kuipers Munneke, P., Ligtenberg, S., Van den Broeke, M., & Vaughan, D. (2014). Firn air depletion as a precursor of Antarctic ice-shelf collapse. *Journal of Glaciology, 60*(220), 205-214.

Kuramoto, T., Goto-Azuma, K., Hirabayashi, M., Miyake, T., Motoyama, H., Dahl-Jensen, D., & Steffensen, J. P. (2011). Seasonal variations of snow chemistry at NEEM, Greenland. *Annals of Glaciology, 52*(58), 193-200.

Legrand, M., & Mayewski, P. (1997). Glaciochemistry of polar ice cores: A review. *Reviews of Geophysics, 35*, 219-243. doi: 10.1029/96RG03527

Lenaerts, J., Van den Broeke, M., Van De Berg, W., Van Meijgaard, E., & Kuipers Munneke, P. (2012). A new, high-resolution surface mass balance map of Antarctica (1979–2010) based on regional atmospheric climate modeling. *Geophysical Research Letters, 39*(4). doi: 10.1029/2011gl050713

Lenaerts, J., Vizcaino, M., Fyke, J., Kampenhout, L., & Van Den Broeke, M. (2016). Present-day and future Antarctic ice sheet climate and surface mass balance in the Community Earth System Model. *Climate Dynamics*, 1-15. doi: 10.1007/s00382-015-2907-4

Linow, S. (2011). *Deriving Snow Accumulation Rates of Greenland and the Antarctic Ice Sheet from Microwave Remote Sensing Data.* (Doktor der Naturwissenschaften PhD), Universitat Bremen, Bremen.

Lythe, M. B., Vaughan, D. G., Lambrecht, A., Miller, H., Nixdorf, U., Oerter, H., . . . Huybrechts, P. (2001). BEDMAP: A new ice thickness and subglacial topographic model of Antarctica. *Journal of Geophysical Research, 335*(B6), 11335-11351. doi: 10.1029/2000jb900449

Maeno, N., & Ebinuma, T. (1983). Pressure sintering of ice and its implication to the densification of snow at polar glaciers and ice sheets. *Journal of Physical Chemistry, 87*(21), 4103-4110. doi: 10.1021/J100244a023

Magand, O., Genthon, C., Fily, M., Krinner, G., Picard, G., Frezzotti, M., & Ekaykin, A. A. (2007). An up-to-date quality-controlled surface mass balance data set for the 90°–180°E Antarctica sector and 1950–2005 period. *Journal of Geophysical Research: Atmospheres, 112*(D12), n/a-n/a. doi: 10.1029/2006JD007691

Majoube, M. (1971). Fractionnement en oxygene-18 et en deuterium entre l'eau et sa vapeur. *J. Chim. phys, 68*(7-8), 1423-1436.

Mariani, I. (2013). *Water Stable Isotopes in Alpine Ice Cores as Proxies for Temperature and Atmospheric Circulation.* (PhD), Universität Bern, Bern.

Markle, B., Bertler, N., Sinclair, K., & Sneed, S. (2012). Synoptic variability in the Ross Sea region, Antarctica, as seen from back-trajectory modeling and ice core analysis. *Journal of Geophysical Research: Atmospheres, 117*(D2). doi: 10.1029/2011jd016437

Marshall, G. (2003). Trends in the Southern Annular Mode from observations and reanalyses. *Journal of Climate, 16*(24), 4134-4143. doi: 10.1175/1520-0442(2003)016<4134:Titsam>2.0.Co;2

Marshall, G. (2007). Half-century seasonal relationships between the Southern Annular Mode and Antarctic temperatures. *International journal of climatology, 27*(3), 373-383. doi: 10.1002/joc.1407

Marshall, G., Orr, A., Van Lipzig, N., & King, J. (2006). The impact of a changing Southern Hemisphere Annular Mode on Antarctic Peninsula summer temperatures. *Journal of Climate, 19*(20), 5388-5404. doi: 10.1175/Jcli3844.1

Martín-Español, A., Zammit-Mangion, A., Clarke, P. J., Flament, T., Helm, V., King, M. A., . . . Schön, N. (2016). Spatial and temporal Antarctic Ice Sheet mass trends, glacio-isostatic adjustment and surface processes from a joint inversion of satellite altimeter, gravity and GPS data. *Journal of Geophysical Research: Earth Surface, 121*, 182–200. doi: 10.1002/2015JF003550

Masson-Delmotte, V., Hou, S., Ekaykin, A., Jouzel, J., Aristarain, A., Bernardo, R., . . . Falourd, S. (2008). A review of Antarctic surface snow isotopic composition: Observations, atmospheric circulation, and isotopic modeling*. *Journal of Climate, 21*(13), 3359-3387.

Mayewski, P., Meredith, M., Summerhayes, C., Turner, J., Worby, A., Barrett, P., . . . Naveira Garabato, A. (2009). State of the Antarctic and Southern Ocean climate system. *Reviews of Geophysics, 47*(1). doi: 10.1029/2007rg000231

Meehl, G., Arblaster, J., Bitz, C. M., Chung, C. T., & Teng, H. (2016). Antarctic sea-ice expansion between 2000 and 2014 driven by tropical Pacific decadal climate variability. *Nature Geoscience, advance online publication*. doi: 10.1038/ngeo2751

Meier, M. F. (1962). Proposed definitions for glacier mass budget terms. *Journal of Glaciology, 4*, 252-263.

Mercer, J. H. (1978). West Antarctic ice sheet and CO 2 greenhouse effect- A threat of disaster. *Nature, 271*(5643), 321-325.

Merlivat, L., & Jouzel, J. (1979). Global climatic interpretation of the deuterium-oxygen 18 relationship for precipitation. *Journal of Geophysical Research: Oceans, 84*(C8), 5029-5033. doi: 10.1029/Jc084ic08p05029

Monaghan, A., Bromwich, D., Fogt, R., Wang, S., Mayewski, P., Dixon, D., . . . Isaksson, E. (2006a). Insignificant change in Antarctic snowfall since the International Geophysical Year. *Science, 313*(5788), 827-831. doi: 10.1126/science.1128243

Monaghan, A., Bromwich, D., & Wang, S. (2006b). Recent trends in Antarctic snow accumulation from Polar MM5 simulations. *Philosophical Transactions of the Royal Society of London A: Mathematical, Physical and Engineering Sciences, 364*(1844), 1683-1708. doi: 10.1098/rsta.2006.1795

Morgan, V. I., Goodwin, I. D., Etheridge, D. M., & Wookey, C. W. (1991). Evidence from Antarctic Ice Cores for Recent Increases in Snow Accumulation. *Nature, 354*(6348), 58-60. doi: 10.1038/354058a0

Müller, K., Sinisalo, A., Anschütz, H., Hamran, S.-E., Hagen, J.-O., McConnel, J. R., & Pasteris, D. R. (2010). An 860 km surface mass-balance profile on the East Antarctic plateau derived by GPR. *Annals of Glaciology, 51*(55), 1-8. doi: 10.3189/172756410791392718

Naish, T., Powell, R., Levy, R., Wilson, G., Scherer, R., Talarico, F., . . . Wilson, T. (2009). Obliquity-paced Pliocene West Antarctic ice sheet oscillations. *Nature, 458*(7236), 322-328. doi: 10.1038/nature07867

Nikolaeva, L. M. (1958). The Ross Ice Shelf, Its Regime and Existence Conditions. – In: Sbornik "Problemy severa", No. 1. Moskva, Izd. AN SSSR. .

O'Keefe, A., & Deacon, D. A. (1988). Cavity ring-down optical spectrometer for absorption measurements using pulsed laser sources. *Review of Scientific Instruments, 59*(12), 2544-2551. doi: 10.1063/1.1139895

Pälli, A., Kohler, J., Isaksson, E., Moore, J., Pinglot, J., Pohjola, V., & Samuelsson, H. (2002). Spatial and temporal variability of snow accumulation using ground-penetrating radar and ice cores on a Svalbard glacier. *Journal of Glaciology, 48*(162), 417-424. doi: 10.3189/172756502781831205

Parish, T. R. (1984). A Numerical Study of Strong Katabatic Winds over Antarctica. *Monthly weather review, 112*(3), 545-554. doi: 10.1175/1520-0493(1984)112<0545:ANSOSK>2.0.CO;2

Parish, T. R., Cassano, J. J., & Seefeldt, M. W. (2006). Characteristics of the Ross Ice Shelf air stream as depicted in Antarctic Mesoscale Prediction System simulations. *Journal of Geophysical Research: Atmospheres, 111*(D12). doi: 10.1029/2005JD006185

Paul, J., & Saykally, R. (1997). Cavity Ringdown Laser Absorption Spectroscopy. *Analytical Chemistry, 69*(9), 287A-292A.

Persson, A. O. (2006). Hadley's principle: understanding and misunderstanding the trade winds. *History of meteorology, 3*, 17-42.

Pfahl, S., & Sodemann, H. (2014). What controls deuterium excess in global precipitation? *Climate of the Past, 10*(2), 771-781. doi: 10.5194/cp-10-771-2014

Phillpot, H., & Zillman, J. (1970). The surface temperature inversion over the Antarctic continent. *Journal of Geophysical Research, 75*, 4161-4169.

Picarro.com. (2016). *Technical Addendum*. Picarro. [online] Available at: http://www.picarro.com/technology/technical_addendum [Accessed 3 Feb. 2016].

Plewes, L. A., & Hubbard, B. (2001). A review of the use of radio-echo sounding in glaciology. *Progress in Physical Geography, 25*(2), 203-236. doi: 10.1177/030913330102500203

Pollard, D., & DeConto, R. M. (2009). Modelling West Antarctic ice sheet growth and collapse through the past five million years. *Nature, 458*(7236), 329-332. doi: 10.1038/nature07809

Pollard, D., DeConto, R. M., & Alley, R. (2015). Potential Antarctic Ice Sheet retreat driven by hydrofracturing and ice cliff failure. *Earth and Planetary Science Letters, 412*, 112-121. doi: 10.1016/j.epsl.2014.12.035

Previdi, M., & Polvani, L. (2016). Anthropogenic impact on Antarctic surface mass balance, currently masked by natural variability, to emerge by mid-century. *Environmental Research Letters, 11*(9), 094001. doi: 10.1088/1748-9326

Reijmer, C., & Van den Broeke, M. (2003). Temporal and spatial variability of the surface mass balance in Dronning Maud Land, Antarctica, as derived from automatic weather stations. *Journal of Glaciology, 49*(167), 512-520. doi: 10.3189/172756503781830494

Reijmer, C., Van Meijgaard, E., & Van den Broeke, M. (2005). Evaluation of temperature and wind over Antarctica in a Regional Atmospheric Climate Model using 1 year of automatic weather station data and upper air observations. *Journal of Geophysical Research: Atmospheres, 110*(D4). doi: 10.1029/2004jd005234

Riebeek, H. (2005). Paleoclimatology: the Oxygen Balance. Retrieved 10 September, 2015, from http://earthobservatory.nasa.gov/Features/Paleoclimatology_OxygenBalance/

Rignot, E. (2011). Ice Sheet Mass Balance. In V. P. Singh, P. Singh & U. K. Haritashya (Eds.), *Encyclopedia of Snow, Ice and Glaciers*. Dordrecht: Springer Netherlands.

Rignot, E., Bamber, J., Van den Broeke, M., Davis, C., Li, Y., Van De Berg, W., & Van Meijgaard, E. (2008). Recent Antarctic ice mass loss from radar interferometry and regional climate modelling. *Nature Geoscience, 1*(2), 106-110. doi: 10.1038/ngeo102

Rignot, E., Casassa, G., Gogineni, P., Krabill, W., Rivera, A., & Thomas, R. (2004). Accelerated ice discharge from the Antarctic Peninsula following the collapse of Larsen B ice shelf. *Geophysical Research Letters, 31*(18). doi: 10.1029/2004gl020697

Rignot, E., Jacobs, S., Mouginot, J., & Scheuchl, B. (2013). Ice-shelf melting around Antarctica. *Science, 341*(6143), 266-270. doi: 10.1126/science.1235798

Rignot, E., Mouginot, J., & Scheuchl, B. (2011a). Ice Flow of the Antarctic Ice Sheet. *Science, 333*(6048), 1427-1430. doi: 10.1126/science.1208336

Rignot, E., Mouginot, J., & Scheuchl, B. (2011b). MEaSUREs InSAR-Based Antarctica Ice Velocity Map. Ross Ice Shelf Subset. Boulder, Colorado USA: NASA National Snow and Ice Data Center Distributed Active Archive Center. . doi: 10.5067/MEASURES/CRYOSPHERE/nsidc-0484.001

Rignot, E., & Steffen, K. (2008). Channelized bottom melting and stability of floating ice shelves. *Geophysical Research Letters, 35*(2). doi: 10.1029/2007gl031765

Ritter, S. (2015). Global CO^2 Breaches 400 PPM. Retrieved 27.06.2015, from http://cen.acs.org/articles/93/i20/Global-CO2-Breaches-400-PPM.html%C3%82

Ritz, C., Agosta, C., Peyaud, V., Durand, G., Fettweis, X., Favier, V., & Gallée, H. (2015). *Modeling interactions between Antarctic Instability and Surface Mass Balance.* Paper presented at the EGU General Assembly Conference Abstracts.

Rockey, C., & Braaten, D. (1995). Characterization of polar cyclonic activity and relationship to observed snowfall events at McMurdo Station, Antarctica, In: Proceedings of the 4th conference on polar meteorol and oceanog. 15–20 Jan 1995. Dallas, Texas. AMS, Boston. pp 244–245.

Rotschky, G., Eisen, O., Wilhelms, F., Nixdorf, U., & Oerter, H. (2004). Spatial distribution of surface mass balance on Amundsenisen plateau, Antarctica, derived from ice-penetrating radar studies. *Annals of Glaciology, 39*(1), 265-270. doi: 10.3189/172756404781814618

Salinger, M. J., Renwick, J. A., & Mullan, A. B. (2001). Interdecadal Pacific Oscillation and South Pacific climate. *International journal of climatology, 21*(14), 1705-1721. doi: 10.1002/joc.691

Scambos, T., Bohlander, J., Shuman, C., & Skvarca, P. (2004). Glacier acceleration and thinning after ice shelf collapse in the Larsen B embayment, Antarctica. *Geophysical Research Letters, 31*(18). doi: 10.1029/2004gl020670

Scambos, T., & Shuman, C. (2016). Comment on 'Mass gains of the Antarctic ice sheet exceed losses' by H. J. Zwally and others. *Journal of Glaciology, 62*(233), 599-603. doi: 10.1017/jog.2016.59

Scarchilli, C., Frezzotti, M., & Ruti, P. (2011). Snow precipitation at four ice core sites in East Antarctica: provenance, seasonality and blocking factors. *Climate Dynamics, 37*(9-10), 2107-2125. doi: 10.1007/s00382-010-0946-4

Scherer, J., Paul, J., O'keefe, A., & Saykally, R. (1997). Cavity ringdown laser absorption spectroscopy: history, development, and application to pulsed molecular beams. *Chemical reviews, 97*(1), 25-52.

Schlosser, E., Anschütz, H., Isaksson, E., Martma, T., Divine, D., & Nøst, O.-A. (2012). Surface mass balance and stable oxygen isotope ratios from shallow firn cores on Fimbulisen, East Antarctica. *Annals of Glaciology, 53*(60), 70-78. doi: 10.3189/2012AoG60A102

Schlosser, E., & Oerter, H. (2002). Seasonal variations of accumulation and the isotope record in ice cores: a study with surface snow samples and firn cores from Neumayer station, Antarctica. *Annals of Glaciology, 35*(1), 97-101. doi: 10.3189/172756402781817374

Schlosser, E., Oerter, H., Masson-Delmotte, V., & Reijmer, C. (2008). Atmospheric influence on the deuterium excess signal in polar firn: implications for ice-core interpretation. *Journal of Glaciology, 54*(184), 117-124. doi: 10.3189/002214308784408991

Schoof, C. (2007). Ice sheet grounding line dynamics: Steady states, stability, and hysteresis. *Journal of Geophysical Research: Earth Surface, 112*(F3). doi: 10.1029/2006JF000664

Sharp, Z. (2007). *Principles of stable isotope geochemistry*. Upper Saddle River, N.J: Pearson/Prentice Hall.

Shepherd, A., Ivins, E., Geruo, A., Barletta, V., Bentley, M., Bettadpur, S., . . . Galin, N. (2012). A reconciled estimate of ice-sheet mass balance. *Science, 338*(6111), 1183-1189. doi: 10.1126/science.1228102

Shepherd, A., & Wingham, D. (2007). Recent sea-level contributions of the Antarctic and Greenland ice sheets. *Science, 315*(5818), 1529-1532. doi: 10.1126/science.1136776

Sinclair, K., Bertler, N., & Trompetter, W. (2010). Synoptic controls on precipitation pathways and snow delivery to high-accumulation ice core sites in the Ross Sea region, Antarctica. *Journal of Geophysical Research: Atmospheres, 115*(D22). doi: 10.1029/2010jd014383

Sinclair, K., Bertler, N., Trompetter, W., & Baisden, W. (2013). Seasonality of airmass pathways to coastal Antarctica: ramifications for interpreting high-resolution ice core records. *Journal of Climate, 26*(6), 2065-2076. doi: 10.1175/Jcli-D-12-00167.1

Singh, P., & Singh, V. P. (2001). *Snow and glacier hydrology* (Vol. 37). Dordrecht: Kluwer Academic Publishers.

Sinisalo, A., Anschütz, H., Aasen, A. T., Langley, K., von Deschwanden, A., Kohler, J., . . . Isaksson, E. (2013). Surface mass balance on Fimbul ice shelf, East Antarctica: Comparison of field measurements and large-scale studies. *Journal of Geophysical Research: Atmospheres, 118*(20), 11,625-611,635. doi: 10.1002/jgrd.50875

Smith, S., & Stearns, C. (1993). Antarctic pressure and temperature anomalies surrounding the minimum in the Southern Oscillation index. *Journal of Geophysical Research: Atmospheres, 98*(D7), 13071-13083. doi: 10.1029/92jd02157

Sold, L., Huss, M., Eichler, A., Schwikowski, M., & Hoelzle, M. (2015). Unlocking annual firn layer water equivalents from ground-penetrating radar data on an Alpine glacier. *The Cryosphere, 9*(3), 1075-1087. doi: 10.5194/tc-9-1075-2015

Spikes, V., Hamilton, G., Arcone, S., Kaspari, S., & Mayewski, P. (2004). Variability in accumulation rates from GPR profiling on the West Antarctic plateau. *Annals of Glaciology, 39*(1), 238-244. doi: 10.3189/172756404781814393

Stammerjohn, S., Martinson, D., Smith, R., Yuan, X., & Rind, D. (2008). Trends in Antarctic annual sea ice retreat and advance and their relation to El Niño–Southern Oscillation and Southern Annular Mode variability. *Journal of Geophysical Research: Oceans, 113*(C3). doi: 10.1029/2007JC004269

Stein, A., Draxler, R., Rolph, G., Stunder, B., Cohen, M., & Ngan, F. (2015). NOAA's HYSPLIT Atmospheric Transport and Dispersion Modeling System. *Bulletin of the American Meteorological Society, 96*(12), 2059-2077. doi: 10.1175/BAMS-D-14-00110.1

Stenni, B., Masson-Delmotte, V., Johnsen, S., Jouzel, J., Longinelli, A., Monnin, E., . . . Selmo, E. (2001). An oceanic cold reversal during the last deglaciation. *Science, 293*(5537), 2074-2077. doi: 10.1126/science.1059702

Stenni, B., Scarchilli, C., Masson-Delmotte, V., Schlosser, E., Ciardini, V., Dreossi, G., . . . Valt, M. (2016). Three-year monitoring of stable isotopes of precipitation at Concordia Station, East Antarctica. *The Cryosphere Discussions, 2016*, 1-30. doi: 10.5194/tc-2016-142

Stichler, W., & Schotterer, U. (2000). From accumulation to discharge: modification of stable isotopes during glacial and post-glacial processes. *Hydrological Processes, 14*(8), 1423-1438. doi: 10.1002/1099-1085(20000615)14:8<1423::Aid-Hyp991>3.0.Co;2-X

Tape, K., Rutter, N., Marshall, H., Essery, R., & Sturm, M. (2010). Recording microscale variations in snowpack layering using near-infrared photography. *Journal of Glaciology, 56*(195), 75-80. doi: 10.3189/002214310791190938

Telle, H., Ureņa, A., & Donovan, R. (2007). *Laser chemistry: spectroscopy, dynamics and applications*. West Sussex: John Wiley & Sons.

Thomas, R. H., MacAyeal, Eilers, & Gaylord. (1984). *Glaciological studies on the Ross Ice Shelf, Antarctica, 1973–1978*: Wiley Online Library.

Thomas, R. H., Rignot, E., Casassa, G., Kanagaratnam, P., Acuña, C., Akins, T., . . . Krabill, W. (2004). Accelerated sea-level rise from West Antarctica. *Science, 306*(5694), 255-258. doi: 10.1126/science.1099650

Town, M., Warren, S., Walden, V., & Waddington, E. (2008). Effect of atmospheric water vapor on modification of stable isotopes in near-surface snow on ice sheets. *Journal of Geophysical Research: Atmospheres, 113*(D24), n/a-n/a. doi: 10.1029/2008JD009852

Trusel, L., Frey, K., Das, S., Karnauskas, K., Kuipers Munneke, P., van Meijgaard, E., & van den Broeke, M. (2015). Divergent trajectories of Antarctic surface melt under two twenty-first-century climate scenarios. *Nature Geoscience*. doi: 10.1038/ngeo2563

Turner, J. (2004). The El Niño–Southern Oscillation and Antarctica. *International journal of climatology, 24*(1), 1-31. doi: 10.1002/joc.965

Turner, J., Connolley, W., Leonard, S., Marshall, G., & Vaughan, D. (1999). Spatial and temporal variability of net snow accumulation over the Antarctic from ECMWF re-analysis project data. *International journal of climatology, 19*(7), 697-724. doi: 10.1002/(Sici)1097-0088(19990615)19:7<697::Aid-Joc392>3.3.Co;2-V

Turner, J., Phillips, T., Hosking, J., Marshall, G., & Orr, A. (2013). The Amundsen Sea Low. *International journal of climatology, 33*(7), 1818-1829. doi: 10.1002/joc.3558

Unden, P., Rontu, L., Järvinen, H., Lynch, P., Calvo, J., Cats, G., . . . Garcia-Moya, J. A. (2002). HIRLAM-5 scientific documentation.

Vallelonga, P., Barbante, C., Cozzi, G., Gaspari, V., Candelone, J.-P., van de Velde, K., . . . Cescon, P. (2004). Elemental indicators of natural and anthropogenic aerosol inputs to Law Dome, Antarctica. *Annals of Glaciology, 39*(1), 169-174. doi: 10.3189/172756404781814483

Van de Berg, W., Van den Broeke, M., Reijmer, C., & Van Meijgaard, E. (2006). Reassessment of the Antarctic surface mass balance using calibrated output of a regional atmospheric climate model. *Journal of Geophysical Research: Atmospheres, 111*(D11). doi: 10.1029/2005JD006495

Van den Broeke, M. (1997). Spatial and temporal variation of sublimation on Antarctica: Results of a high-resolution general circulation model. *Journal of Geophysical Research: Atmospheres, 102*(D25), 29765-29777. doi: 10.1029/97JD01862

Van den Broeke, M., Reijmer, C., & van de Wal, R. (2004). A study of the surface mass balance in Dronning Maud Land, Antarctica, using automatic weather stations. *Journal of Glaciology, 50*(171), 565-582. doi: 10.3189/172756504781829756

Van den Broeke, M., Van de Berg, W., & Van Meijgaard, E. (2006). Snowfall in coastal West Antarctica much greater than previously assumed. *Geophysical Research Letters, 33*(2). doi: 10.1029/2005GL025239

van Lipzig, N. P., Meijgaard, E. v., & Oerlemans, J. (2002). The spatial and temporal variability of the surface mass balance in Antarctica: results from a regional atmospheric climate model. *International journal of climatology, 22*(10), 1197-1217. doi: 10.1002/joc.798

Van Loon, H. (1967). The half-yearly oscillations in middle and high southern latitudes and the coreless winter. *Journal of the Atmospheric Sciences, 24*(5), 472-486.

Van Meijgaard, E., Van Ulft, L., Van de Berg, W., Bosveld, F., Van den Hurk, B., Lenderink, G., & Siebesma, A. (2008). *The KNMI regional atmospheric climate model RACMO version 2.1*: Koninklijk Nederlands Meteorologisch Instituut.

Van Wessem, J., Reijmer, C., Morlighem, M., Mouginot, J., Rignot, E., Medley, B., . . . Bamber, J. (2014). Improved representation of East Antarctic surface mass balance in a regional atmospheric climate model. *Journal of Glaciology, 60*(222), 761-770. doi: 10.3189/2014JoG14J051

Vaughan, D. G., Bamber, J. L., Giovinetto, M., Russell, J., & Cooper, A. P. R. (1999a). Reassessment of net surface mass balance in Antarctica. *Journal of Climate, 12*(4), 933-946. doi: 10.1175/1520-0442(1999)012<0933:Ronsmb>2.0.Co;2

Vaughan, D. G., Comiso, J. C., Allison, I., Carrasco, J., Kaser, G., Kwok, R., . . . Ren, J. (2013). Observations: cryosphere. *Climate change*, 317-382. In: *Climate Change 2013: The Physical Science Basis. Contribution of Working Group I to the Fifth Assessment Report of the Intergovernmental Panel on Climate Change* [Stocker, T.F., D. Qin, G.-K. Plattner, M. Tignor, S.K. Allen, J. Boschung, A. Nauels, Y. Xia, V. Bex and P.M. Midgley (eds.)]. Cambridge University Press, Cambridge, United Kingdom and New York, NY, USA.

Vaughan, D. G., Corr, H. F., Doake, C. S., & Waddington, E. D. (1999b). Distortion of isochronous layers in ice revealed by ground-penetrating radar. *Nature, 398*(6725), 323-326. doi: 10.1038/18653

Verfaillie, D., Fily, M., Le Meur, E., Magand, O., Jourdain, B., Arnaud, L., & Favier, V. (2012). Snow accumulation variability derived from radar and firn core data along a 600 km transect in Adelie Land, East Antarctic plateau. *The Cryosphere, 6*(6), 1345-1358. doi: 10.5194/tc-6-1345-2012

Vickers, W. W. (1958). On Snow Accumulation and Meteorologic Observation. Preliminary Reports of the Antarctic and Northern Hemisphere Glaciology Programs. Group III. . IGY Glaciological Report Series No. 1. (Amer. Geogr. Soc., IGY World Data Centre).

Vimeux, F., Masson, V., Jouzel, J., Stievenard, M., & Petit, J. (1999). Glacial–interglacial changes in ocean surface conditions in the Southern Hemisphere. *Nature, 398*(6726), 410-413. doi: 10.1038/18860

Vogler, D. E. (2005). *Open-path and fiber-based cavity ringdown spectroscopy.* (PhD), Swiss Federal Institute of Technology, Zurich.

Wade, F. A. (1937). Northeastern Borderlands of the Ross Sea: Glaciological Studies in King Edward VII Land and Northwestern Marie Byrd Land. *Geographical Review*, 584-597.

Wang, Y., Ding, M., Van Wessem, J., Schlosser, E., Altnau, S., Van den Broeke, M., . . . Wang, J. (2016). A comparison of Antarctic Ice Sheet surface mass balance from atmospheric climate models and in situ observations. *Journal of Climate, 29*(2016), 5317-5337. doi: 10.1175/Jcli-D-15-0642.1

Wheeler, M., Newman, S., Orr-Ewing, A., & Ashfold, M. (1998). Cavity ring-down spectroscopy. *Journal of the Chemical Society, Faraday Transactions, 94*(3), 337-351.

Willmott, C., Robeson, S., & Matsuura, K. (2012). A refined index of model performance. *International journal of climatology, 32*(13), 2088-2094. doi: 10.1002/joc.2419

Winkelmann, R., Levermann, A., Martin, M., & Frieler, K. (2012). Increased future ice discharge from Antarctica owing to higher snowfall. *Nature, 492*(7428), 239-242. doi: 10.1038/nature11616

Zumberge, J. H. (1958). Preliminary Report on the Ross Ice Shelf Deformation Project. Preliminary Reports of the Antarctic and Northern Hemisphere Glaciology Programs.- Group IV. IGY Glaciological Report Series No. 1. (Amer. Geogr. Soc., IGY World Data Centre A). Trans Amer. Geophys. Union, Vol. 39, No. 4. 1959. (IGY Bulletin, No. 14).

Zwally, H., Li, J., Robbins, J., Saba, J., Yi, D., & Brenner, A. (2015). Mass gains of the Antarctic ice sheet exceed losses. *Journal of Glaciology, 61*(230), 1019-1036. doi: 10.3189/2015JoG15J071

8 APPENDICES

APPENDIX 1: STABLE ISOTOPES OF HYDROGEN AND OXYGEN

The stable isotopes of hydrogen and oxygen are useful for paleoclimatology research by examining the ratio of the heavy and light molecules in marine sediments, ice cores or fossils (Dansgaard, 1964; Gat & Gonfiantini, 1981; Riebeek, 2005; Cuffey & Paterson, 2010). Like all elements, oxygen is made up of a nucleus of protons and neutrons and is surrounded by a cloud of electrons. All oxygen atoms have 8 electrons and a nucleus with 8 protons and up to 10 neutrons. As seen in Figure 41 the 'light' ($\delta^{16}O$) isotope of oxygen consists of 8 neutrons within the nucleus, whereas the 'heavy' ($\delta^{18}O$) (12.5% heavier than $\delta^{16}O$), consists of 10 neutrons. Oxygen also exists as $\delta^{17}O$, where the nucleus consists of 8 protons and 9 neutrons. The geochemistry of $\delta^{17}O$ mimics that of $\delta^{18}O$, but as $\delta^{18}O$ is 5.5 times more abundant, it is usually not considered separately; although this is changing as analytical methods improve. Thus, further information on $\delta^{17}O$ is limited. The isotopic composition of $\delta^{16}O$, $\delta^{17}O$, and $\delta^{18}O$ in the Earth's atmosphere is 99.759%, 0.0307%, and 0.204% (or, approximately one heavy isotope for every 500 light isotopes), and the relative atomic masses are 15.9949, 16.9991, and 17.9991, respectively.

There are three isotopes of the element hydrogen: protium (H), deuterium (D), and tritium, each consisting of one proton, one electron and up to 2 neutrons (1 for deuterium and 2 for tritium) (Figure 50). Tritium is however, unstable and has a half-life of 12.32yrs, and will not be discussed further.

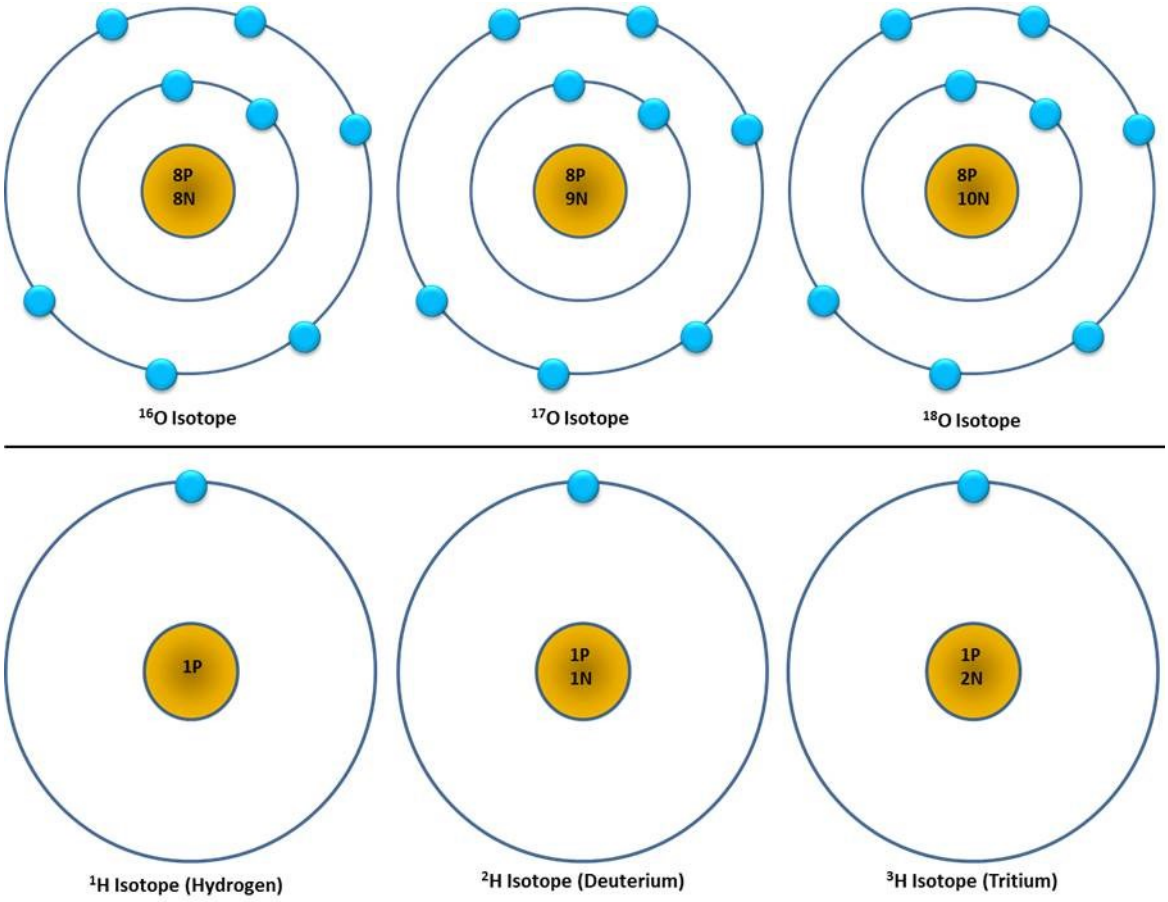

Figure 50: Stable oxygen isotopes (top) and hydrogen isotopes (bottom).

The combination of oxygen and hydrogen isotopes leaves the possibility for nine configurations of water, of which $H_2{}^{16}O$, $H_2{}^{18}O$, and $HD^{16}O$ are the most common. At equilibrium, water vapour in the atmosphere contains 10% less $\delta^{18}O$ and 100% less $\delta^{2}H$ than ocean water (Calkin, 1995). Oxygen isotopes are more commonly used for paleoclimate and surface mass balance studies than hydrogen isotopes, as hydrogen isotopes are less abundant in nature and more difficult to measure in the laboratory (Calkin, 1995), although as technology has improved this has changed.

i. Basic Overview

Analysing the isotopic composition ($\delta^{18}O$ and $\delta^{2}H$) of a firn core is common method for identifying seasonal and annual layers of snowfall (Eisen et al., 2008). For practical purposes, absolute concentrations of hydrogen and oxygen isotopes are seldom used. Instead, the ratio of one isotope relative to the other in a given compound is measured against a reference ratio, usually V-SMOW (Vienna Standard Mean Ocean Water). The ratios of $^{18}O/^{16}O$ and D/H of

water or ice are measured as $\delta^{18}O$ and $\delta^{2}H$ and are defined in equation 8.1, where δ is either $\delta^{18}O$ or $\delta^{2}H$ (Cuffey & Paterson, 2010).

$$\delta = \left[\frac{R - R_{SMOW}}{R_{SMOW}}\right] \times 1000 \qquad 8.1$$

where R = the abundance ratio of δ_{light} / δ_{heavy} in the sample, compared to R_{SMOW}, the standard ratio. Equation 8.1 gives results in units of parts per thousand (‰, or per-mille).

Global atmospheric circulation depletes heavy isotope containing waters from air masses in high altitudes and latitudes (Cuffey & Paterson, 2010). The light $H_2{}^{16}O$ has a vapour pressure approximately 10% (100‰) higher than HDO and approximately 1% (10‰) higher than $H_2{}^{18}O$ (Calkin, 1995). Therefore, the heavy molecules of HDO and $H_2{}^{18}O$ evaporate less readily and condensate more rapidly from the vapour than the lighter $H_2{}^{16}O$.

The simplest model of atmospheric circulation includes Hadley and Ferrel Cells. From the tropics, warm, moist air is transferred in Hadley Cells towards approximately 30°S/N, where Ferrel Cells drive air circulation towards the poles. Ferrel Cells carry evaporated subtropical ocean water, (relatively) rich in HDO and $H_2{}^{18}O$, towards the polar regions. As these heavier isotopes are preferentially removed, precipitates that occur in progressively cooler regions are gradually more negative in HDO and $H_2{}^{18}O$, as can be seen in figure 51 (Calkin, 1995; Singh & Singh, 2001; Cuffey & Paterson, 2010). In the winter months, the heavier isotopes are lost to precipitation earlier in the atmospheric cycle, leading to less of them reaching the polar regions. This effect is known as distillation and is discussed in more detail in section ii.

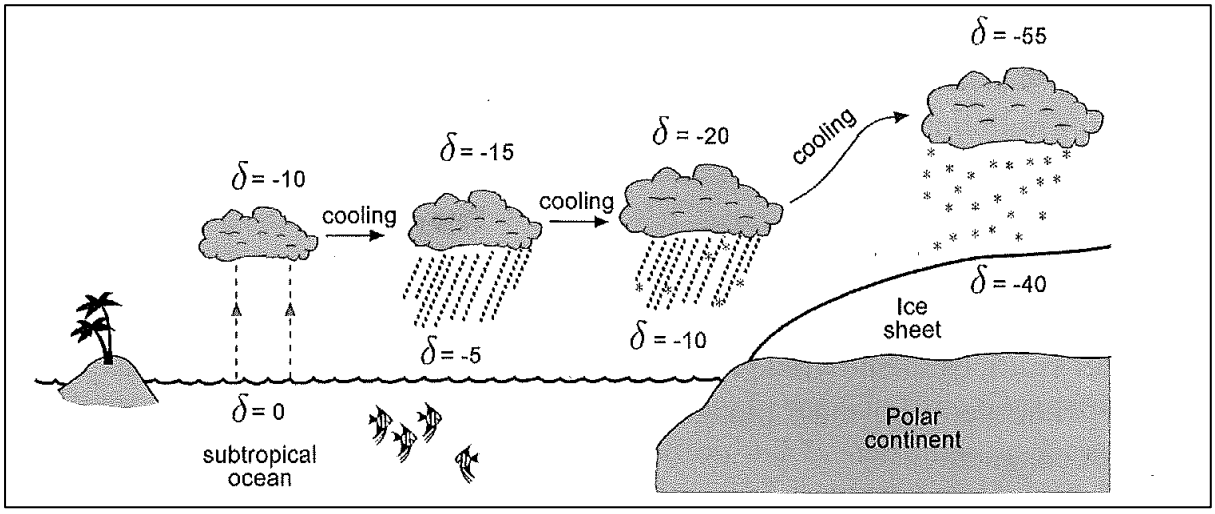

Figure 51: Schematic of moisture transport from mid to high latitudes and the associated change in δ for the air mass and precipitation (Cuffey & Paterson, 2010).

ii. Fractionation Theory & Rayleigh Distillation

The partition of isotopes between two substances or two phases of the same substance with different isotope ratios is called *isotope fractionation*. The dominate phenomena resulting in isotope fractionations are (Sharp, 2007):

- Equilibrium isotope distribution (i.e. isotope exchange reactions)
- Kinetic processes, which depend mostly on differences in reaction rates of isotopic molecules

The equilibrium isotope effects can be expressed quantitatively as the constants of an exchange reaction:

$$K = \frac{\left(\frac{A_2}{A_1}\right)^a}{\left(\frac{B_2}{B_1}\right)^b} \qquad 8.2$$

where species A and B contain either the light or heavy isotope 1 or 2, respectively. Equation 8.2 suggests equilibrium, that is, the forward and backward rates of reaction are equal. In isotope studies, the equilibrium factor, or fractionation factor, α, is referred to rather than *K*.

$$\alpha_{A-B} = \frac{R_A}{R_B} \qquad 8.3$$

where R = the ratio of the heavy isotope to the lighter isotope (i.e., $^{2}H/^{1}H$, $^{18}O/^{16}O$) in compounds *A* and *B* (liquid and vapour in this instance). α is often close to 1 and is unitless.

The deviation of α from 1 is a measure of the isotope equilibrium effect, and is dependent on temperature and phase state. For $^{18}O/^{16}O$ fractionation, based on Earth temperatures, α ranges from 1.008 to 1.025 (Gat & Gonfiantini, 1981; Cuffey & Paterson, 2010). For example, the fractionation factor α of the water-vapour transition at 20°C is 1.0098 for ^{18}O; meaning that the liquid water is slightly enriched in heavier molecules, whilst at 0°C, the fractionation factor is 1.0117 indicating the influence of temperature (Majoube, 1971).

Although for a homogenous body of water the rate $R_B = R_A = \alpha$, the rate varies for the different isotopes of water that coincide in each of the liquid and vapour phases. $H_2{}^{16}O$ has the highest rate and preferentially enters the vapour phase. As mentioned previously, the vapour pressures of the isotopes differ, thus, for water, the higher the mass numbers of the isotope, the lower the equilibrium vapour pressure. For this reason, in a condensate, $H_2{}^{18}O$ is

enriched, and in vapour, $H_2{}^{16}O$ is enriched, or: $H_2{}^{18}O/\ H_2{}^{16}O\ _{(l)} < H_2{}^{18}O/\ H_2{}^{16}O\ _{(v)}$ (Gat & Gonfiantini, 1981) .

As an air mass cools and loses moisture via condensation, isotopic fractionation occurs, known as *Rayleigh distillation*, which describes the isotopic ratio of an air mass at each stage where condensation is removed and vapour is removed.

In a parcel of air, n_o moles of light water and n_j moles of heavy water are present. The isotopic ratio of the vapour (R_v) = n_j / n_o. As a condensate (R_p) forms, its isotopic ratio is offset from R_v slightly:

$$R_p = \alpha R_v, or, 1 + \delta_p = \alpha\,[1 + \delta_v] \qquad 8.4$$

By, definition, $1 + \delta_v = R_v / R_s$, with R_s being the standard ratio, α the fractionation factor as described previously.

During condensation, the amount of vapour removed from the parcel of air, dn_o and dn_j, are related by $dn_j = R_p dn_o = \alpha R_v dn_o$. As ($R_v$) = n_j / n_o, we get equation 8.5:

$$\frac{dn_j}{n_j} = \alpha \frac{dn_o}{n_o} \qquad 8.5$$

Particularly important for the sensitivity of isotopes in snowfall is the increase of α at low temperatures, illustrating how cooler air masses lose their heavy isotopes faster than warmer air masses. A more important factor for the sensitivity of isotopes in snowfall is the temperature dependence of air mass moisture content at middle and high latitudes (Cuffey & Paterson, 2010).

Precipitation events from an air mass continuously deplete clouds of the heavier $H_2{}^{18}O$ and HDO, a phenomenon known as the rainout effect (Dansgaard, 1964). This effect is particularly apparent over large continents as the clouds are not replenished from evaporation. The arrangement of rainout and equilibrium fractionation is described by Rayleigh Distillation. The isotopic composition of water vapour changes once condensation has occurred, and from the definition (R_v) = n_j / n_o, differentiation gives (second equality from eq. 8.5):

$$\frac{dR_v}{R_v} = \frac{dn_j}{n_j} - \frac{dn_o}{n_o} = [\alpha - 1] \qquad 8.6$$

Changes in the isotopic composition of vapour and condensate covary, because $R_p = \alpha R_v$, then $dR_p = R_v d\alpha + \alpha dR_v$, changes in isotopic compositions of vapour and condensate co-vary. Dividing through by αR_v, and using equation 8.4 and the definition of δ, shows that:

$$\frac{d\delta_p}{1+\delta_p} = \frac{d\alpha}{\alpha} + \frac{dR_v}{R_v} \qquad 8.7$$

The relative abundances of $H_2{}^{16}O$, $H_2{}^{18}O$, and $HD^{16}O$ are 0.9977:0.0020:0.0003 (Dansgaard, 1964; Cuffey & Paterson, 2010). Thus, as the abundance of light water greatly exceeds that of the heavy water ($n_o >> n_j$), it can be said that the total quantity of the water vapour ≈ the quantity of the light water species. Let W be the total moles of water vapour in the air parcel. Assuming that $W \approx n_o$:

$$\frac{d\delta_p}{1+\delta_p} = \frac{d\alpha}{\alpha} + [\alpha - 1]\frac{dW}{W} \qquad 8.8$$

Equation 8.8 explains how the δ value of the condensate decreases as the air mass loses water. As an approximation, α is replaced with its mean value, $\bar{\alpha}$. Integration of equation 8.8 between initial and subsequent values of vapour content (W_o and W, respectively) and composition (δ_{po} and δ_p, respectively), gives the Rayleigh Distillation relation:

$$\delta_p = \left[1 + \delta_{po}\right]\left[\frac{W}{W_o}\right]^{\bar{\alpha}-1} - 1 \qquad 8.9$$

Distillation increases abruptly as W/W_0 approaches zero. For example, in a scenario with an $\bar{\alpha}$ value of 1.1 for δ^2H and an initial δ^2H =0, decreasing the water vapour content from $0.9W_0$, to $0.5W_0$, to $0.1W_0$, reduces the condensates δ^2H to approximately -10‰, -70‰ and -200‰ respectively (Cuffey & Paterson, 2010).

The formation of precipitation is determined by the cooling of saturated air, therefore a reduction of W depends on temperature. The gas law states that the amount of water vapour in a given parcel of air is directly proportional to the saturation pressure ($\underline{e_s}$) and inversely proportional to the total pressure (P). e_s is approximated from an exponential function as it varies only with temperature. e_s is therefore $\propto exp\ (-\Lambda/T)$, for Kelvin temperature (T), and Λ≈5400KK/6150K over water/ice, respectively. Overall, following on from equation 8.9, a change from the initial temperature and pressure of condensation (T_0, P_o respectively) to the final temperature and pressure (T, P, respectively), results in a final isotopic value of precipitation is given by:

$$1 + \delta_p = \left[1 + \delta_{po}\right]\left[\frac{P_o}{P}\right]^{\bar{\alpha}^{-1}} \exp\left(-\Lambda\left[\bar{\alpha} - 1\right]\frac{[T_o - T]}{TT_o}\right) \qquad 8.10$$

The temperature decrease from T_o to T removes many of the heavy isotopes from the air mass. This is why δ values in precipitation are more negative in the winter compared to summer. In addition, as the temperature is lowered even further, the lighter isotopes will begin to condensate more readily, increasing the ratio of light to heavy molecules.

iii. Kinetic effects and evaporation

The above description of Rayleigh Distillation assumes thermodynamic equilibrium. Both equilibrium and kinetic effects occur when water is evaporated from the sea surface.

The kinetic energy of a molecule is based on temperature:

$$kT = \frac{1}{2}mv^2 \qquad 8.11$$

where k = Boltzmann constant, T = temperature (in kelvin), m = molecular mass, and v = average molecular velocity. Accordingly, molecules with a higher mass have a higher molecular velocity at a specific temperature. Because of this, molecules that are more massive have a lower diffusion velocity and lower chemical reactivity (due to lower collision frequency). Lighter elements are thus more sensitive to isotopic fractionation as the heavier molecules have higher binding energies. That is to say, the heavier isotopes will preferentially be in a phase with stronger bonds (solid > liquid > vapour). Vibrational energy is required to break the stronger bond of a heavy isotope with its carrying molecule, and is provided by temperature. At lower temperatures, the differences in binding energies between isotopic molecules are larger, and in theory, at very high temperatures, there is no fractionation, i.e. when there is more energy (temperature) there is less discrimination between the heavy and light molecules. Most fractionation of water occurs during physical processes, such as precipitation or evaporation events. As these phase changes are reversible, with sufficient time these phase changes will reach equilibrium. Kinetic effects at the formation of liquid cloud drops are usually negligible and dominated by equilibrium processes, however kinetic effects are particularly important during evaporation.

If a turbulent atmosphere continuously transports away the evaporated water, the phase change cannot reach equilibrium and is forced towards one side of the reaction. As seawater

evaporation occurs at the thin boundary layer at the interface of the seawater and atmosphere, the isotopic composition of the evaporating water vapour flux depends on the local meteorological conditions. In addition to wind, temperature, and humidity conditions, the sea surface-atmosphere exchange is affected by the isotope ratio of the pre-existing vapour in the marine boundary layer. At the sea-atmosphere interface, a thin (micrometers thick) layer exists at 100% saturation, where equilibrium conditions dominate. Between this layer and the turbulent atmosphere, a transition zone exists where molecular diffusion dominates the transport process (Craig & Gordon, 1965). If the relative humidity above the ocean surface decreases, larger diffusion takes place, thus increasing the kinetic fractionation and vice versa in highly humid, turbulent conditions. Therefore, the total isotopic fractionation should take into account both equilibrium conditions and fractionation effects. Principally, Rayleigh equations can still be used providing they are based on the appropriate fractionation factors. For evaporation, values for α are dependent on the kinetic effect and are usually estimated by equation 8.12 (Merlivat & Jouzel, 1979):

$$\alpha = \frac{1 - c\mathcal{H}}{1 - c}\alpha_{eq} \qquad 8.12$$

where α_{eq} denotes the equilibrium fractionation factor, $\mathcal{H}$ the relative humidity above the sea surface and c a constant dependent on wind speed and the diffusivities of water molecules in air.

Given that water isotope hydrology incorporates kinetic and equilibrium processes, fractionation is often referred to as non-equilibrium fractionation and Rayleigh distillation, termed Rayleigh-type processes (Gat, 2005). Non-equilibrium may also occur in mixed phase clouds (where the three phases of water coexist). Here, water vapour is deposited onto the ice crystals and liquid is removed by evaporation. Kinetic fractionation occurs in both the vapour deposition and liquid evaporation changes, in both cases leaving the initial phase more enriched in the heavier isotopes (Jouzel & Merlivat, 1984). As the equilibrium fractionation factor is lower for $H_2{}^{18}O$, variations in δ^2H concentrations are proportionally less affected by kinetic effects than for $\delta^{18}O$. Sub-cloud effects may impose a significant change in the isotopic composition of the precipitation, although for snowflakes this effect is negligible due to the low molecular diffusion of ice (Gat, 2010).

iv. The Global Meteoric Water Line (GMWL) and the *d*-excess parameter

A linear relationship exists between δ^2H and $\delta^{18}O$, a relationship known as the Global Meteoric Water Line (GMWL). Craig (1961) plotted δ^2H and $\delta^{18}O$ values against each other (Figure 18), and was the first to discover the GMWL: $\delta^2H = 8 \times \delta^{18}O + d$, where *d,* deuterium excess*,* is ≈10‰ in in the majority of meteoric waters on Earth (Sharp, 2007).

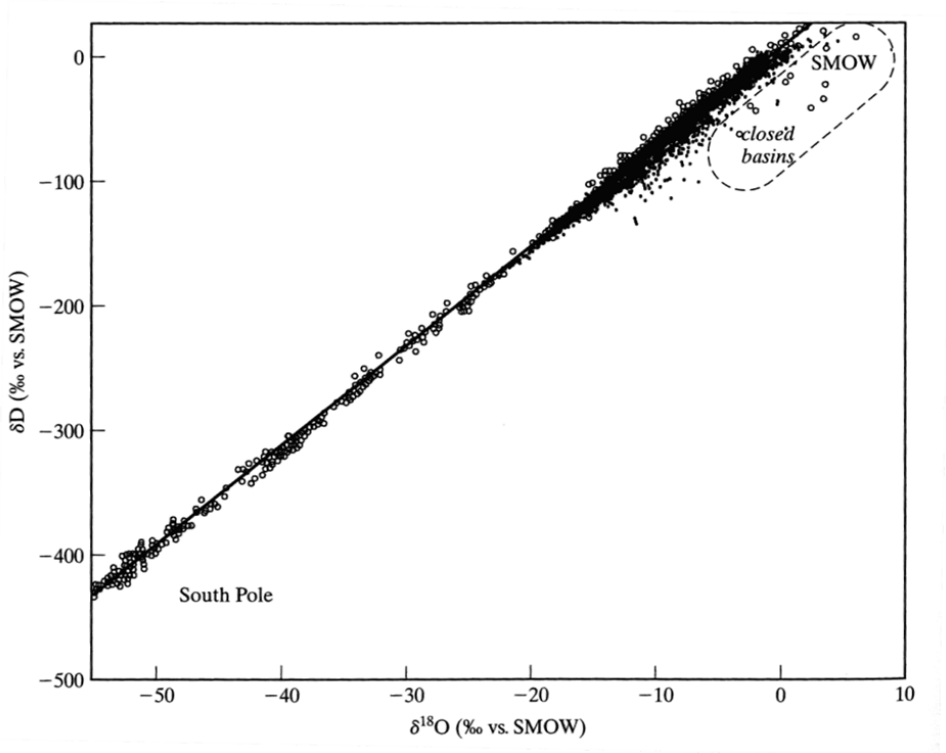

Figure 52: Global Meteoric Water Line. Originally produced by Craig (1961), adapted from Sharp (2007).

The GMWL is a linear relationship that represents the average meteoric water lines from all over the world, but all regions on earth have their own local meteoric water lines (LMWL).

The intercept, *d*, or deuterium excess, is defined as:

$$d = \delta D - 8 \times \delta^{18}O \qquad 8.13$$

The *d*-excess parameter explains the deviation from equilibrium conditions and is thus an indicator for kinetic fractionation. *d*-excess increases with an increase in the moisture deficit, 1- *h*, at the site of evaporation, where *h* is the relative humidity at the surface temperature of

the water (Sharp, 2007). The *d*-excess of 10‰ in the GMWL corresponds to an average RH over the oceans of 81%, with global mean RH being around 10% lower in winter than summer. In arid regions where strong evaporation occurs, kinetic fractionation effects are much stronger leading to much larger *d*-excess values. Perhaps the most well-known example of this is the case of the eastern basin of the Mediterranean region, where *d*-excess values of >18‰ have been observed (Gat & Carmi, 1970). As condensation can be assumed to take place at equilibrium, it seems reasonable to assume that the *d*--excess parameter would be a good proxy for the moisture source conditions, such as temperature and humidity at the site of evaporation. For example, Johnsen et al. (1989) found that the *d*-excess values in Greenland precipitation implied that the moisture source was from the subtropical part of the North Atlantic Ocean. Past studies have related the variability of the *d*-excess in polar regions to changes in sea surface temperature (e.g. Vimeux et al., 1999; Stenni et al., 2001). Other studies suggest that relative humidity is the main driver for *d*-excess (e.g. Jouzel & Merlivat, 1982; Pfahl & Sodemann, 2014). With respect to Antarctic snow, the *d*-excess provides useful insight into the source location of the precipitation, although this varies with location. Higher *d*-excess values are commonly associated with precipitation originating from air masses that travel further inland or across the continent and vice versa. At interior Antarctic locations, a negative correlation is generally observed between δ^2H or $\delta^{18}O$ and *d*-excess (Froehlich et al., 2001; Masson-Delmotte et al., 2008), but positive correlations between δ^2H or $\delta^{18}O$ and *d*-excess are commonly observed at Antarctic coastal sites (Ciais et al., 1995; Schlosser et al., 2008). As the source of precipitation on the RIS is thought to come from both the Ross and Amundsen seas, interpretation of *d*-excess records may prove difficult without knowledge of snowfall timing. For example, precipitation originating from the Amundsen Sea often traverses the WAIS which would lead to high *d*-excess values and more negative δ values, whilst precipitation from the Ross Sea would yield lower *d*-excess values and less negative δ values.

APPENDIX 2: WAVELENGTH-SCANNED CAVITY RING DOWN SPECTROSCOPY (WS-CRDS)

The use of WS-CRDS is an excellent method for measuring water isotopes, allowing for real time, continuous measurements. WS-CRDS instruments (commonly Picarro branded) are widely used within the ice core community, and this study has made use of a Picarro L1102-i instrument.

i. Introduction & History

Spectroscopy in general is defined as the measurement of the outcomes of the interaction of a light wave with matter (Telle et al., 2007). Most absorption techniques encompass measuring a tiny change in the total transmitted intensity of a light source through an absorbing medium. Single pass absorption techniques often lead to a high background condition that is proportional to the intensity of the light source that restricts sensitivity (Telle et al., 2007), a problem that is overcome by the use of WS-CRDS. WS-CRDS is independent of the initial light intensity which translates to improved sensitivities due to the removal of signal dependence on shot to shot light intensity variability (Wheeler et al., 1998). WS-CRDS was developed by O'Keefe and Deacon (1988) with the aim of improving the sensitivity of the conventional absorption techniques available for measurements of trace compounds. There is now a wide range of applications for WS-CRDS, from environmental, industrial, bio-pharmaceutical and even security (Vogler, 2005).

The idea of CRDS was conceived in the early 1980's with the knowledge that mirror reflectivity could be precisely and accurately determined by quantifying the phase shift of a continuous wave laser exiting a cavity between two mirrors (Scherer et al., 1997), known as the CAPS (cavity attenuated phase shift) method (Herbelin & Mckay, 1981). The major difference between CAPS and CRDS is with the CAPS method, the photon lifetime in the cavity is not measured directly, and is instead calculated from the shift in the phase angle. This makes the sensitivity of the CAPS method approximately two orders of magnitude worse than CRDS due to the inconsistency characteristic of making the phase shift measurement. The CAPS method was only developed for characterising mirror reflectivities, but paved the way for all subsequent developments that led to the current CRDS technique (Scherer et al., 1997). As mirror reflectivity approached unity, it became more and more

difficult to measure reflectivity, as it is practically impossible to measure the minute light intensity difference before and after reflection from a mirror (Berden & Engeln, 2009). Further developments (Anderson et al., 1984) made use of a technique that was capable of measuring the photo lifetime in the cavity by directly switching off a continuous wave laser and monitoring the decay of light intensity over time, known as ring-down time. This led to greater sensitivity and lower error. For example, with a ring-down error of 1% using mirrors with a 99.995% reflectivity, the uncertainty of the absorption determination is $\sim 5*10^{-7}$ compared with $\sim 4*10^{-6}$ with phase angle uncertainly of 1% using the same mirrors. O'Keefe and Deacon (1988) showed that an instrument that by using an instrument designed to measure mirror reflectivity, it was possible to faint visible absorptions of air due to the highly forbidden (i.e. extremely unlikely) transitions of molecular oxygen (Berden & Engeln, 2009). This paved way for CRDS as it is known today, capable of making ultrasensitive (mole fractions down to parts per trillion) direct absorption measurements (Telle et al., 2007), and is explained in detail in section ii.

ii. Principles of the WS-CRDS Technique

WS-CRDS exploits infrared (IR) or near-infrared (NIR) CW lasers, as this frequency shows a large number of highly characteristic rotational-vibrational transitions for gas phase water (Kerstel, 2005; Mariani, 2013), and CW waves allow for increased sensitivity (Berden & Engeln, 2009). Nearly all gas-phase molecules have unique IR or NIR absorption spectrums, consisting of a series of narrow, sharp lines with each at a characteristic wavelength (Figure 53). Each of the sharp spectral absorption lines is due to the laser exciting vibrations and rotations in the gas phase molecules. The frequency of the vibrations depends on the exact mass of the atoms in each isotopologue, therefore, the concentration of any species can be measured by the height of a specific absorption peak, or, the strength of the absorption (Picarro.com, 2016).

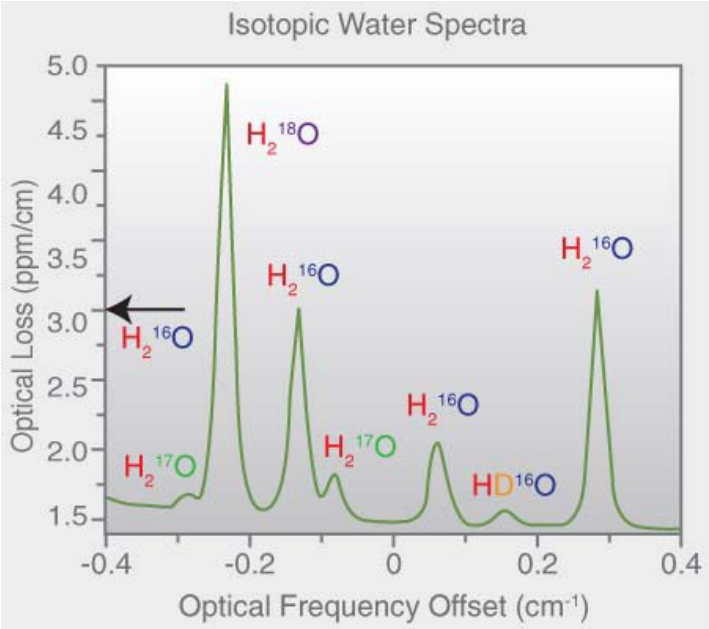

Figure 53: An example of spectral absorption lines of hydrogen isotopologues. Each isotopologue has its own characteristic peak. From www.picarro.com

An IR laser that is tuned to water molecule absorption wavelengths is shot into an optical cavity that contains two or more highly reflective mirrors (R≥ 0.999). This light is directed onto the input mirror of the cavity, of which most is reflected off the highly reflective mirror. As the mirror is not a perfect reflector, some of the light (<0.1%) is transmitted through into the cavity. When the photodetector signal reaches a threshold (i.e. when there is sufficient light in the cavity) the continuous wave (CW) laser is abruptly switched off. This small amount of light then bounces off the mirrors continuously (up to 100,000 times) and becomes 'trapped' in the cavity for up to a few microseconds, depending on the reflectivity of the mirrors. Small amounts of light transmit out through the exit mirror, where an extremely sensitive photodetector monitors the leakage of light. As the light decreases by a constant percentage, the detector sees an exponential decay of light, i.e. 'ringing down' towards zero (Telle et al., 2007). The extremely long path length of the laser light (>20km) gives rise to the very high sensitivity.

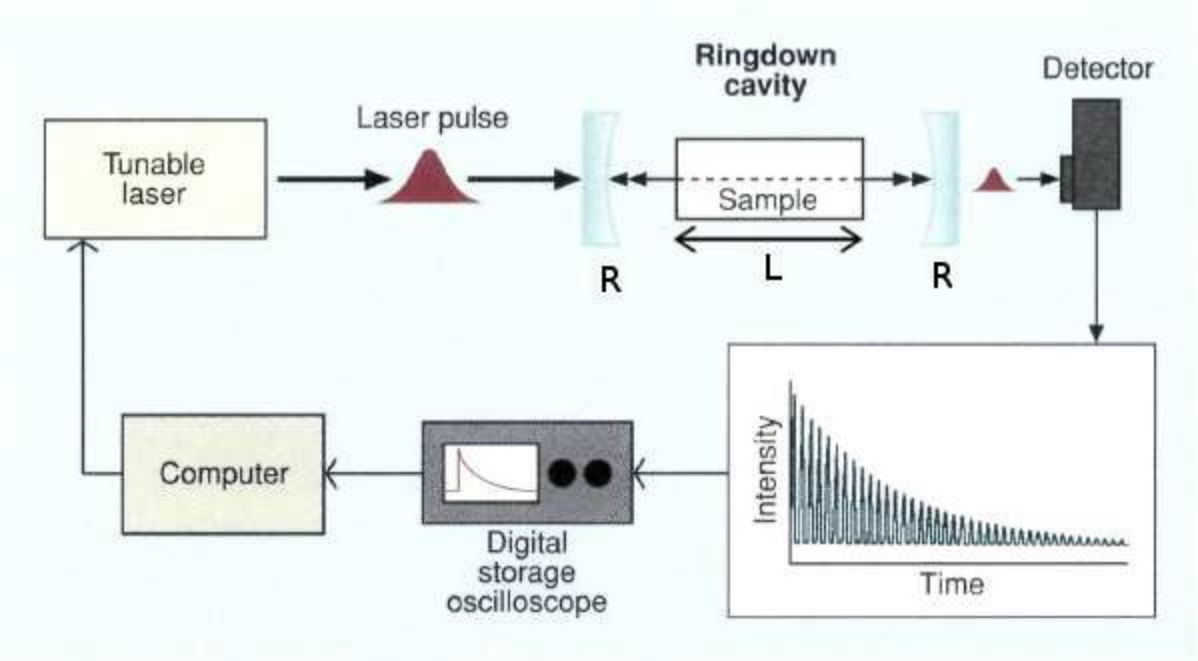

Figure 54: Schematic diagram of a typical CRDS set –up, with a cavity length, L, and two highly reflective mirrors, R. From: Paul and Saykally (1997).

If an additional gas species capable of absorbing laser light enters the cavity, a second mechanism of light loss is introduced. This therefore accelerates the ringdown speed compared to an 'empty' cavity (Figure 55). For example, if a gas has an absorption of 1ppm per pass, a resultant increase of 63% of the total loss per pass and 38% decrease in ringdown time would be observed (Berden & Engeln, 2009).

The use of WS-CRDS is advantageous to conventional spectrometers, as it measures decay rates of light intensity, opposed to absolute transmitted or absorbed light intensity. This removes the dependency on initial light intensity and sample-to-sample variations of light intensity. The result is sensitivity and precisions typically around <0.1‰ for $\delta^{18}O$ and <1‰ for $\delta^{2}H$.

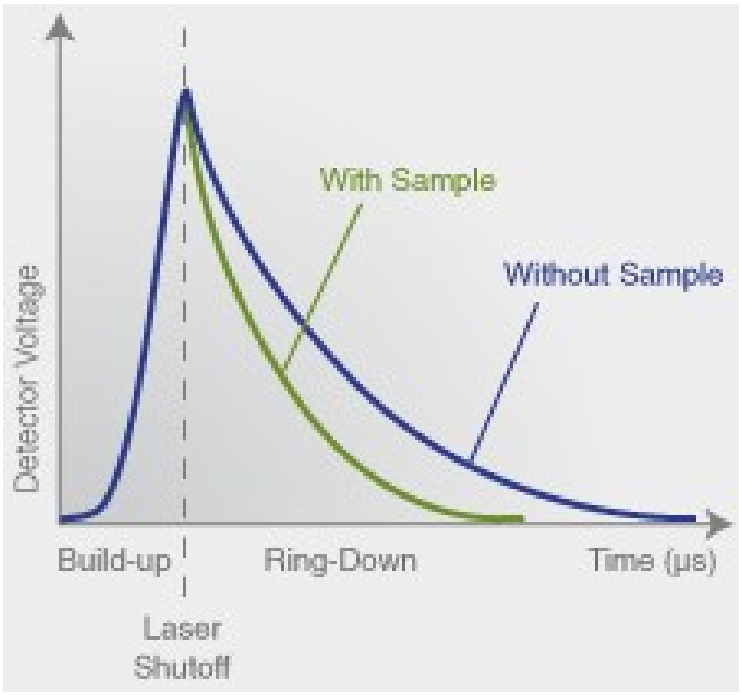

Figure 55: Light intensity as a function of time in a CRDS system, with and without a sample present in the cavity, illustrating how absorption by the gas is rendered into a time measurement. From www.picarro.com.

The physical basis of absorption spectroscopy techniques rely on the Lambert-Beer law (eq. 8.14) which states that the intensity of light travelling through a medium is attenuated due to the interaction with the medium and is characterised by a decreasing exponential function (Telle et al., 2007). The rate of absorption depends on the path length and the sample (medium) concentration:

$$A = ln\left(\frac{I_o}{I}\right) = \sigma L_{abs} N \qquad 8.14$$

Where A is the absorbance, I_o is the initial light intensity, I is the transmitted light intensity, σ is the absorption cross section, L_{abs} is the path length of the light through the absorber and N is the number density of absorber molecules. As mentioned in section i, most conventional absorption techniques are not sufficiently sensitive when measuring extremely low concentrations. WS-CRDS overcomes this limitation by increasing the path length drastically (effective path lengths of up to 20 kilometres) (Picarro.com, 2016).

If the only loss process for light is leakage through the mirrors, the ringdown is characterised by

$$I = I_0\, exp\left(\frac{-t}{\tau_0}\right), with = \frac{t_r}{2(1-R)} = \frac{L_{opt}}{c(1-R)} \qquad 8.15$$

where t_r is the roundtrip time for light in the cavity, R is the reflectivity of the mirrors, L_{opt} is the distance between the two or more mirrors, c is the speed of light in a vacuum ($\approx 3 \times 10^8 \frac{m}{s}$) and τ_0 is the 1/e (~36.8%) decay time of the light, or, the ringdown lifetime.

If an absorber is present in the cavity, equation 8.15 must be modified to account for its presence:

$$I = I_0\, exp\left(-\frac{t}{\tau}\right), with \frac{1}{\tau} = \frac{1}{\tau_0} + (\sigma L_{abs} N)\left(\frac{c}{L_{opt}}\right) \qquad 8.16$$

where L_{abs} is the path length of the absorber and τ is the 1/e decay time for light in the presence of the absorber. The absorbance can then be calculated

$$A = \frac{L_{opt}}{c}\left(\frac{1}{\tau} - \frac{1}{\tau_0}\right) \qquad 8.17$$

Equation 8.17 is suitable for comparisons of a cavity with absorbers present (with ringdown time τ) to a cavity without absorbers present, or, in a reference state (with ringdown time τ_0).

APPENDIX 3: RAW STABLE ISOTOPE & DENSITY DATA

Sample No.	Depth	Density (kg m^{-3}, from site C)	$\delta^{18}O$ (‰ V-SMOW)	$\delta^{2}H$ (‰ V-SMOW)	d-excess
1	0.03	485.58	-32.82	-261.64	0.89
2	0.06	408.55	-37.32	-295.78	2.79
3	0.09	381.76	-38.68	-305.83	3.64
4	0.12	348.27	-38.63	-305.57	3.50
5	0.15	415.25	-38.57	-304.50	4.09
6	0.18	418.60	-37.07	-293.32	3.26
7	0.21	365.02	-33.16	-258.39	6.93
8	0.24	344.93	-26.79	-202.46	11.87
9	0.27	294.69	-24.30	-187.25	7.11
10	0.3	341.58	-22.15	-173.24	3.94
11	0.33	375.07	-24.44	-194.50	1.05
12	0.36	354.97	-25.65	-202.88	2.30
13	0.39	425.30	-26.35	-208.26	2.57
14	0.42	314.79	-27.83	-218.45	4.15
15	0.45	368.37	-30.63	-241.17	3.87
16	0.48	418.60	-32.63	-258.57	2.45
17	0.51	351.62	-34.27	-269.07	5.07
18	0.54	334.88	-34.60	-271.37	5.40
19	0.57	324.83	-34.35	-270.40	4.39
20	0.6	331.53	-33.64	-264.33	4.81
21	0.63	344.93	-32.52	-254.53	5.62
22	0.66	328.18	-32.13	-248.78	8.27
23	0.69	425.30	-31.18	-243.51	5.89
24	0.72	365.02	-30.04	-235.37	4.97
25	0.75	247.81	-28.84	-223.55	7.16
26	0.78	251.16	-27.18	-210.54	6.89
27	0.81	227.72	-26.11	-201.79	7.12
28	0.84	294.69	-26.03	-202.12	6.08
29	0.87	351.62	-26.16	-206.24	3.07
30	0.9	328.18	-28.24	-224.29	1.65
31	0.93	341.58	-30.70	-245.89	-0.30
32	0.96	277.95	-33.02	-264.78	-0.65
33	0.99	308.09	-34.51	-276.70	-0.64
34	1.02	421.95	-34.80	-277.20	1.16
35	1.05	358.32	-33.51	-266.46	1.64
36	1.08	294.69	-30.77	-239.56	6.58
37	1.11	405.20	-27.55	-210.65	9.72
38	1.15	364.18	-24.53	-184.33	11.94
39	1.18	341.58	-28.33	-219.53	7.13
40	1.21	344.93	-24.75	-194.46	3.56

41	1.24	318.14	-25.60	-201.18	3.60
42	1.27	241.11	-26.72	-211.47	2.31
43	1.3	224.37	-27.63	-219.06	1.95
44	1.33	354.97	-28.23	-222.14	3.72
45	1.36	321.48	-28.42	-222.49	4.88
46	1.39	344.93	-28.36	-219.17	7.73
47	1.42	361.67	-28.20	-219.95	5.67
48	1.45	321.48	-28.12	-219.24	5.75
49	1.48	274.60	-28.14	-217.30	7.85
50	1.51	284.65	-27.90	-215.24	8.00
51	1.54	257.86	-28.06	-216.12	8.39
52	1.57	321.48	-28.41	-219.48	7.82
53	1.6	365.02	-28.92	-225.71	5.64
54	1.64	421.95	-28.44	-223.93	3.60
55	1.67	207.63	-27.15	-214.86	2.37
56	1.7	401.86	-26.55	-207.45	4.97
57	1.73	418.60	-25.30	-198.88	3.52
58	1.76	365.02	-25.60	-201.45	3.39
59	1.79	167.44	-26.77	-208.07	6.10
60	1.82	334.88	-28.20	-220.53	5.09
61	1.85	304.74	-29.86	-235.34	3.56
62	1.88	358.32	-31.12	-247.41	1.52
63	1.91	368.37	-31.50	-250.50	1.54
64	1.94	381.76	-31.18	-245.79	3.62
65	1.97	344.93	-30.62	-243.52	1.40
66	2	308.09	-29.39	-229.73	5.36
67	2.03	288.00	-28.18	-221.15	4.32
68	2.06	298.04	-26.98	-214.72	1.11
69	2.09	294.69	-26.81	-210.26	4.23
70	2.12	334.88	-26.53	-209.17	3.09
71	2.15	274.60	-26.27	-206.88	3.31
72	2.18	294.69	-26.10	-204.52	4.24
73	2.21	288.00	-26.17	-203.84	5.55
74	2.24	304.74	-26.50	-206.84	5.18
75	2.26	371.72	-27.23	-214.37	3.46
76	2.29	321.48	-28.84	-227.86	2.85
77	2.32	351.62	-30.16	-240.15	1.14
78	2.35	351.62	-31.07	-249.87	-1.34
79	2.38	338.23	-32.14	-257.94	-0.82
80	2.41	294.69	-32.33	-259.37	-0.74
81	2.44	385.11	-31.85	-253.73	1.09
82	2.47	381.76	-30.82	-245.73	0.84
83	2.51	381.76	-29.78	-235.94	2.33
84	2.54	274.60	-29.47	-228.99	6.79

85	2.57	284.65	-29.47	-227.84	7.89
86	2.6	321.48	-29.56	-230.97	5.48
87	2.63	277.95	-29.70	-234.14	3.49
88	2.66	244.46	-29.88	-235.52	3.54
89	2.69	304.74	-29.90	-235.18	4.05
90	2.72	304.74	-29.46	-231.61	4.03
91	2.75	277.95	-29.06	-225.53	6.93
92	2.78	318.14	-28.34	-220.02	6.72
93	2.8	361.67	-27.80	-215.38	6.99
94	2.83	264.55	-30.22	-238.58	3.19
95	2.86	221.02	-29.94	-235.21	4.34
96	2.89	281.30	-29.76	-234.09	4.02
97	2.92	251.16	-29.16	-227.41	5.86
98	2.95	314.79	-28.23	-221.57	4.29
99	2.98	371.72	-28.22	-220.35	5.43
100	3.01	405.20	-28.03	-218.98	5.29
101	3.04	354.97	-29.31	-229.44	5.01
102	3.07	375.07	-29.39	-231.28	3.81
103	3.1	398.51	-29.33	-229.70	4.91
104	3.13	368.37	-29.39	-230.06	5.03
105	3.16	365.02	-29.26	-229.63	4.42
106	3.19	358.32	-28.35	-219.04	7.78
107	3.22	354.97	-28.80	-223.94	6.45
108	3.25	381.76	-29.91	-234.05	5.25
109	3.28	361.67	-30.83	-242.56	4.07
110	3.31	405.20	-31.62	-249.04	3.95
111	3.34	254.51	-32.24	-253.39	4.53
112	3.37	308.09	-32.86	-257.46	5.39
113	3.4	288.00	-33.35	-262.54	4.29
114	3.43	331.53	-33.67	-266.65	2.68
115	3.46	301.39	-33.93	-268.15	3.29
116	3.49	221.02	-33.53	-265.45	2.81
117	3.52	381.76	-33.03	-261.65	2.55
118	3.55	408.55	-32.42	-255.53	3.82
119	3.58	385.11	-32.13	-254.27	2.78
120	3.61	298.04	-31.93	-253.47	1.98
121	3.64	395.16	-31.87	-253.62	1.35
122	3.67	398.51	-31.87	-252.37	2.61
123	3.7	385.11	-31.45	-249.66	1.97
124	3.73	341.58	-30.86	-244.81	2.06
125	3.76	415.25	-30.08	-238.08	2.58
126	3.79	391.81	-29.46	-231.55	4.09
127	3.82	281.30	-28.60	-225.32	3.49
128	3.84	311.44	-28.63	-225.82	3.22

129	3.87	294.69	-29.33	-231.45	3.16
130	3.9	284.65	-30.06	-238.50	2.00
131	3.93	314.79	-30.43	-241.44	2.00
132	3.96	405.20	-30.68	-242.05	3.38
133	3.99	321.48	-30.49	-240.43	3.49
134	4.02	318.14	-30.23	-236.32	5.53
135	4.05	391.81	-29.76	-231.47	6.64
136	4.08	438.69	-29.23	-227.42	6.39
137	4.11	452.09	-28.96	-224.64	7.03
138	4.14	358.32	-28.73	-223.57	6.27
139	4.17	334.88	-28.68	-224.70	4.74
140	4.2	388.46	-28.89	-227.79	3.32
141	4.23	431.99	-28.74	-230.46	-0.54
142	4.26	391.81	-29.65	-237.70	-0.47
143	4.29	368.37	-30.26	-240.44	1.64
144	4.32	338.23	-30.39	-241.72	1.40
145	4.35	358.32	-30.35	-241.74	1.06
146	4.38	391.81	-30.26	-240.40	1.69
147	4.41	421.95	-29.70	-236.18	1.45
148	4.44	381.76	-29.22	-232.13	1.61
149	4.46	442.04	-28.77	-228.80	1.36
150	4.49	371.72	-28.24	-224.92	1.02
151	4.52	361.67	-28.09	-222.89	1.86
152	4.55	358.32	-27.76	-221.09	0.96
153	4.58	385.11	-27.60	-219.91	0.86
154	4.61	375.07	-27.78	-220.75	1.45
155	4.64	385.11	-28.96	-227.95	3.72
156	4.67	398.51	-29.21	-231.29	2.36
157	4.7	328.18	-29.70	-235.40	2.23
158	4.73	365.02	-30.12	-238.10	2.88
159	4.76	378.41	-30.32	-239.61	2.95
160	4.79	428.65	-30.07	-239.54	1.04
161	4.82	452.09	-29.68	-237.20	0.28
162	4.85	421.95	-29.65	-234.28	2.96
163	4.88	351.62	-28.88	-228.65	2.38
164	4.91	405.20	-28.29	-223.23	3.11
165	4.94	354.97	-27.96	-219.83	3.88
166	4.97	435.34	-27.35	-215.69	3.12
167	5	418.60	-27.74	-219.62	2.26
168	5.03	428.65	-28.13	-222.60	2.47
169	5.06	421.95	-28.46	-225.32	2.38
170	5.09	411.90	-29.30	-232.92	1.47
171	5.12	391.81	-29.93	-238.10	1.36
172	5.15	431.99	-30.51	-242.17	1.91

173	5.18	442.04	-31.05	-245.54	2.83
174	5.22	391.81	-31.56	-249.04	3.48
175	5.25	298.04	-32.19	-254.07	3.45
176	5.28	388.46	-32.17	-254.14	3.23
177	5.31	418.60	-33.20	-262.35	3.29
178	5.34	435.34	-33.91	-267.58	3.70
179	5.37	445.39	-34.34	-272.00	2.70
180	5.4	405.20	-34.60	-275.39	1.38
181	5.43	435.34	-34.76	-275.37	2.67
182	5.46	421.95	-34.46	-273.94	1.71
183	5.49	388.46	-34.48	-273.78	2.04
184	5.52	385.11	-34.25	-271.96	2.03
185	5.55	405.20	-34.02	-268.83	3.33
186	5.58	415.25	-33.77	-266.80	3.37
187	5.61	425.30	-32.97	-262.51	1.28
188	5.64	431.99	-32.64	-257.76	3.34
189	5.67	445.39	-31.78	-251.17	3.09
190	5.7	398.51	-30.56	-240.95	3.53
191	5.73	375.07	-29.41	-232.99	2.26
192	5.76	344.93	-28.74	-223.73	6.19
193	5.79	401.86	-27.80	-216.36	6.00
194	5.82	368.37	-27.25	-213.33	4.66
195	5.85	348.27	-27.56	-214.37	6.08
196	5.88	375.07	-27.82	-218.10	4.44
197	5.91	368.37	-28.48	-223.32	4.54
198	5.94	351.62	-29.10	-229.01	3.78
199	5.97	388.46	-29.89	-235.48	3.66
200	6	458.79	-30.51	-240.96	3.12
201	6.03	401.86	-30.93	-244.49	2.93
202	6.06	435.34	-30.87	-243.66	3.28
203	6.09	462.13	-30.98	-244.09	3.73
204	6.12	455.44	-30.98	-242.92	4.90
205	6.15	509.02	-30.99	-242.57	5.33
206	6.18	445.39	-31.31	-245.13	5.32
207	6.21	415.25	-31.79	-250.63	3.71
208	6.24	401.86	-32.24	-255.03	2.92
209	6.27	385.11	-32.49	-258.87	1.04
210	6.305	453.52	-32.52	-260.23	-0.08
211	6.335	452.09	-32.41	-258.06	1.21
212	6.365	468.83	-31.42	-250.01	1.39
213	6.395	448.74	-30.34	-240.44	2.29
214	6.435	527.44	-29.03	-229.60	2.62
215	6.465	361.67	-27.49	-214.48	5.42
216	6.495	428.65	-25.83	-200.84	5.77

217	6.525	408.55	-25.22	-194.68	7.08
218	6.555	395.16	-24.99	-193.93	6.00
219	6.58	466.15	-26.99	-215.44	0.48
220	6.61	442.04	-27.20	-217.25	0.34
221	6.64	415.25	-27.46	-219.83	-0.18
222	6.67	438.69	-27.56	-220.95	-0.49
223	6.7	425.30	-27.65	-222.25	-1.08
224	6.715	375.07	-28.29	-225.28	1.06
225	6.745	401.86	-28.10	-224.12	0.71
226	6.775	375.07	-28.08	-222.77	1.90
227	6.805	368.37	-27.78	-220.24	1.96
228	6.835	445.39	-27.58	-218.88	1.73
229	6.865	438.69	-27.34	-217.34	1.37
230	6.895	425.30	-27.14	-215.40	1.72
231	6.925	395.16	-27.16	-215.14	2.13
232	6.955	368.37	-27.02	-215.78	0.37
233	6.985	395.16	-27.19	-214.45	3.06
234	7.015	398.51	-27.38	-215.94	3.08
235	7.045	381.76	-27.48	-218.87	0.95
236	7.075	425.30	-27.93	-224.19	-0.74
237	7.105	485.58	-28.13	-227.23	-2.21
238	7.135	381.76	-29.27	-233.29	0.87
239	7.165	354.97	-29.84	-239.47	-0.77
240	7.195	398.51	-30.61	-244.89	-0.05
241	7.225	435.34	-31.14	-249.26	-0.10
242	7.255	468.83	-31.27	-248.13	2.06
243	7.285	448.74	-31.01	-245.64	2.41
244	7.315	452.09	-30.79	-243.20	3.10
245	7.345	375.07	-31.10	-244.03	4.74
246	7.375	452.09	-30.65	-238.83	6.37
247	7.405	418.60	-30.02	-236.88	3.29
248	7.445	489.76	-30.35	-235.52	7.28
249	7.475	408.55	-30.08	-235.85	4.83
250	7.505	455.44	-29.83	-234.74	3.91
251	7.535	438.69	-30.31	-236.08	6.41
252	7.565	442.04	-30.38	-236.44	6.61
253	7.595	442.04	-30.54	-237.04	7.28
254	7.625	455.44	-30.60	-238.51	6.29
255	7.655	445.39	-31.01	-240.95	7.11
256	7.685	458.79	-30.98	-242.30	5.52
257	7.715	431.99	-30.90	-243.11	4.08
258	7.745	425.30	-31.02	-244.00	4.13
259	7.775	448.74	-31.13	-243.19	5.83
260	7.805	435.34	-31.02	-243.16	4.98

261	7.835	428.65	-30.90	-242.63	4.55
262	7.865	519.06	-30.62	-240.88	4.08
263	7.895	505.67	-30.75	-241.82	4.17
264	7.925	445.39	-30.79	-241.61	4.69
265	7.955	421.95	-30.86	-242.77	4.10
266	7.98	494.28	-30.98	-244.34	3.48
267	8.01	415.25	-31.10	-244.32	4.45
268	8.04	448.74	-31.17	-244.36	4.97
269	8.07	431.99	-31.16	-243.89	5.36
270	8.1	458.79	-31.22	-243.37	6.35
271	8.13	448.74	-31.32	-244.41	6.11
272	8.16	448.74	-31.35	-245.99	4.77
273	8.19	442.04	-31.59	-247.76	4.99
274	8.22	438.69	-31.63	-250.15	2.92
275	8.235	569.30	-31.76	-249.46	4.64
276	8.265	445.39	-31.82	-249.96	4.62
277	8.295	428.65	-31.33	-247.60	3.01
278	8.325	435.34	-31.48	-247.54	4.33
279	8.355	418.60	-31.24	-245.79	4.09
280	8.385	448.74	-31.25	-245.90	4.06
281	8.415	438.69	-31.20	-247.24	2.32
282	8.445	455.44	-31.24	-249.19	0.69
283	8.475	431.99	-31.29	-250.19	0.09
284	8.505	458.79	-30.95	-248.96	-1.38
285	8.535	452.09	-30.77	-246.91	-0.76
286	8.565	525.76	-30.17	-241.50	-0.13
287	8.595	498.97	-29.45	-235.07	0.50
288	8.625	498.97	-28.81	-230.99	-0.50
289	8.655	468.83	-27.93	-222.90	0.58
290	8.685	442.04	-27.26	-216.72	1.35
291	8.715	428.65	-26.82	-213.13	1.44
292	8.745	405.20	-26.59	-210.30	2.44
293	8.775	415.25	-26.23	-206.84	3.03
294	8.805	415.25	-26.34	-206.46	4.29
295	8.835	411.90	-26.27	-206.27	3.92
296	8.865	425.30	-26.24	-205.72	4.24
297	8.895	448.74	-26.19	-207.07	2.48
298	8.92	482.23	-26.49	-207.92	4.02
299	8.95	401.86	-26.28	-206.98	3.26
300	8.98	442.04	-26.69	-210.05	3.48
301	8.997	437.31	-26.62	-208.64	4.34
302	9.017	381.76	-26.59	-209.60	3.15
303	9.037	462.13	-26.86	-210.19	4.69
304	9.057	426.97	-27.09	-212.25	4.46

305	9.077	442.04	-27.25	-213.92	4.06
306	9.097	401.86	-27.35	-214.71	4.07
307	9.117	431.99	-27.54	-216.14	4.15
308	9.137	416.93	-27.59	-216.51	4.18
309	9.157	457.11	-27.54	-216.67	3.62
310	9.177	487.25	-27.60	-216.94	3.83
311	9.197	482.23	-27.57	-216.68	3.85
312	9.217	507.34	-27.25	-213.90	4.08
313	9.237	502.32	-27.07	-211.70	4.85
314	9.257	492.27	-26.80	-208.64	5.77
315	9.277	487.25	-26.44	-205.57	5.98
316	9.297	507.34	-26.11	-202.76	6.16
317	9.317	512.37	-25.73	-200.47	5.35
318	9.337	482.23	-25.57	-199.21	5.34
319	9.357	416.93	-25.61	-199.24	5.62
320	9.377	517.39	-25.60	-199.92	4.86
321	9.397	542.51	-25.54	-200.00	4.30
322	9.417	502.32	-25.75	-202.31	3.66
323	9.437	502.32	-25.74	-202.70	3.20
324	9.457	517.39	-25.89	-204.07	3.02
325	9.477	406.88	-26.13	-206.41	2.67
326	9.497	426.97	-26.35	-207.71	3.11
327	9.517	492.27	-26.50	-209.02	3.00
328	9.537	477.20	-26.50	-209.86	2.16
329	9.557	482.23	-26.77	-211.61	2.56
330	9.59	484.05	-26.61	-210.59	2.31
331	9.61	406.88	-27.44	-217.42	2.08
332	9.63	457.11	-27.53	-218.16	2.09
333	9.65	401.86	-28.25	-224.46	1.56
334	9.67	452.09	-28.69	-227.99	1.53
335	9.69	431.99	-29.10	-230.28	2.50
336	9.71	472.18	-29.70	-234.96	2.68
337	9.73	452.09	-29.95	-238.08	1.54
338	9.75	472.18	-30.61	-242.32	2.55
339	9.77	507.34	-31.03	-245.88	2.33
340	9.79	452.09	-31.39	-248.79	2.37
341	9.81	447.06	-31.74	-251.33	2.61
342	9.83	447.06	-31.56	-251.70	0.81
343	9.85	447.06	-32.22	-255.72	2.04
344	9.87	482.23	-32.32	-256.35	2.21
345	9.89	467.16	-32.09	-255.13	1.59
346	9.91	462.13	-32.31	-256.89	1.59
347	9.93	462.13	-32.00	-254.91	1.10
348	9.95	442.04	-32.18	-255.66	1.78

349	9.97	452.09	-32.28	-256.00	2.24
350	9.99	457.11	-31.96	-253.92	1.76
351	10.02	495.62	-31.53	-250.53	1.74
352	10.035	535.81	-31.71	-249.02	4.69
353	10.055	542.51	-30.72	-244.52	1.23
354	10.075	497.30	-30.93	-244.83	2.59
355	10.095	431.99	-30.70	-243.33	2.26
356	10.115	477.20	-30.70	-240.74	4.85
357	10.135	502.32	-30.45	-238.69	4.91
358	10.155	452.09	-30.28	-236.72	5.53
359	10.175	492.27	-30.01	-234.10	6.00
360	10.195	502.32	-29.80	-233.15	5.28
361	10.215	431.99	-29.58	-231.34	5.27
362	10.235	517.39	-29.38	-230.12	4.89
363	10.255	497.30	-29.11	-228.26	4.60
364	10.275	512.37	-29.11	-228.93	3.94
365	10.295	517.39	-29.16	-229.39	3.88
366	10.315	497.30	-29.17	-230.24	3.10
367	10.335	462.13	-29.25	-231.16	2.82
368	10.355	487.25	-29.37	-232.18	2.75
369	10.375	517.39	-29.60	-233.58	3.26
370	10.395	567.62	-29.76	-235.53	2.58
371	10.415	542.51	-29.87	-237.40	1.58
372	10.435	492.27	-30.21	-239.33	2.36
373	10.455	502.32	-30.41	-241.13	2.16
374	10.465	482.23	-30.68	-242.62	2.81
375	10.485	512.37	-30.59	-242.97	1.75
376	10.505	517.39	-30.65	-242.22	2.97
377	10.525	512.37	-30.76	-243.63	2.43
378	10.545	542.51	-30.88	-244.14	2.88
379	10.565	502.32	-30.69	-242.92	2.59
380	10.585	552.55	-30.71	-242.48	3.19
381	10.605	502.32	-30.37	-241.05	1.90
382	10.625	502.32	-30.07	-239.71	0.87
383	10.645	497.30	-30.32	-239.51	3.05
384	10.665	492.27	-29.82	-236.35	2.24
385	10.685	547.53	-29.50	-234.36	1.60
386	10.705	507.34	-29.62	-232.97	4.03
387	10.725	502.32	-29.03	-229.28	2.93
388	10.745	467.16	-29.14	-227.77	5.33
389	10.765	497.30	-28.83	-225.10	5.54
390	10.785	502.32	-28.59	-222.67	6.06
391	10.805	502.32	-28.40	-221.65	5.56
392	10.825	512.37	-28.07	-219.36	5.23

393	10.845	542.51	-29.02	-223.57	8.57
394	10.865	527.44	-29.16	-228.11	5.15
395	10.885	537.48	-29.37	-231.52	3.41
396	10.905	542.51	-29.75	-234.80	3.24
397	10.925	497.30	-30.15	-239.26	1.95
398	10.945	542.51	-30.51	-242.64	1.44
399	10.965	532.46	-30.64	-244.75	0.37
400	10.985	512.37	-30.91	-246.79	0.47
401	11.005	532.46	-30.42	-245.36	-2.00
402	11.025	522.41	-30.49	-244.05	-0.13
403	11.045	512.37	-30.27	-240.90	1.27
404	11.065	542.51	-29.87	-235.35	3.63
405	11.085	562.60	-29.10	-228.64	4.14
406	11.11	530.45	-28.49	-222.50	5.43
407	11.13	537.48	-27.74	-216.29	5.59
408	11.15	522.41	-27.99	-217.60	6.35
409	11.17	462.13	-26.48	-208.07	3.74
410	11.19	527.44	-26.09	-201.61	7.07
411	11.21	492.27	-25.74	-197.91	7.98
412	11.23	532.46	-25.42	-195.16	8.19
413	11.25	562.60	-25.25	-193.58	8.42
414	11.27	577.67	-24.98	-192.38	7.47
415	11.29	497.30	-24.88	-191.41	7.65
416	11.31	547.53	-24.85	-190.51	8.30
417	11.33	527.44	-24.70	-189.61	8.02
418	11.35	547.53	-24.89	-190.07	9.06
419	11.37	507.34	-24.98	-190.63	9.22
420	11.39	502.32	-25.26	-192.21	9.86
421	11.41	562.60	-25.49	-194.50	9.41
422	11.43	527.44	-25.90	-198.15	9.02
423	11.45	527.44	-26.41	-202.78	8.53
424	11.47	547.53	-27.61	-212.82	8.03
425	11.49	482.23	-27.07	-208.71	7.85
426	11.51	602.78	-28.22	-218.67	7.11
427	11.53	386.79	-28.90	-225.03	6.17
428	11.55	617.85	-29.67	-231.63	5.76
429	11.57	426.97	-30.18	-236.56	4.89
430	11.59	517.39	-30.27	-237.69	4.48
431	11.61	532.46	-30.74	-241.75	4.16
432	11.63	567.62	-30.85	-242.64	4.15
433	11.65	512.37	-30.82	-243.06	3.49
434	11.67	502.32	-30.66	-241.03	4.25
435	11.69	522.41	-30.42	-238.95	4.42
436	11.71	537.48	-29.98	-235.11	4.76

437	11.73	547.53	-29.56	-231.75	4.69
438	11.75	552.55	-29.07	-227.79	4.75
439	11.77	562.60	-28.66	-224.07	5.21
440	11.79	552.55	-28.26	-220.89	5.21
441	11.81	467.16	-27.75	-216.19	5.77
442	11.83	567.62	-27.34	-213.79	4.91
443	11.85	492.27	-26.92	-209.81	5.55
444	11.87	452.09	-26.57	-207.77	4.80
445	11.89	467.16	-25.99	-203.51	4.38
446	11.91	512.37	-26.08	-203.99	4.61
447	11.93	552.55	-26.90	-209.03	6.18
448	11.95	587.71	-26.75	-207.72	6.29
449	11.97	532.46	-26.85	-210.29	4.54
450	11.99	542.51	-27.14	-211.22	5.89
451	12.01	507.34	-27.22	-213.10	4.65
452	12.03	572.64	-27.34	-214.64	4.06
453	12.06	475.53	-28.00	-219.91	4.09
454	12.08	386.79	-28.29	-223.88	2.46
455	12.1	507.34	-29.09	-226.40	6.30
456	12.12	497.30	-29.23	-228.47	5.35
457	12.14	542.51	-29.58	-230.59	6.01
458	12.16	582.69	-29.61	-232.13	4.79
459	12.18	537.48	-29.85	-232.83	6.00
460	12.2	391.81	-29.85	-232.65	6.18
461	12.22	527.44	-30.23	-234.02	7.83
462	12.24	376.74	-30.25	-235.22	6.79
463	12.26	527.44	-30.43	-240.28	3.16
464	12.28	562.60	-30.62	-238.89	6.07
465	12.3	492.27	-30.66	-241.19	4.07
466	12.32	527.44	-31.05	-243.74	4.67
467	12.34	552.55	-31.23	-244.51	5.30
468	12.36	567.62	-31.42	-245.96	5.44
469	12.38	552.55	-31.46	-246.30	5.42
470	12.4	532.46	-31.48	-246.62	5.26
471	12.42	622.88	-31.42	-246.10	5.30
472	12.44	572.64	-31.25	-244.61	5.36
473	12.46	552.55	-31.15	-243.39	5.78
474	12.48	527.44	-31.20	-242.88	6.69
475	12.5	552.55	-31.10	-242.66	6.11
476	12.52	517.39	-31.08	-242.56	6.05
477	12.54	577.67	-31.04	-242.22	6.07
478	12.56	567.62	-30.99	-242.37	5.53
479	12.58	582.69	-30.92	-242.09	5.25
480	12.6	562.60	-30.91	-242.34	4.92

481	12.62	477.20	-30.79	-240.71	5.60
482	12.64	567.62	-30.70	-240.82	4.77
483	12.66	522.41	-30.15	-237.94	3.27
484	12.68	487.25	-30.03	-235.91	4.35
485	12.7	522.41	-29.64	-233.34	3.81
486	12.72	562.60	-29.48	-232.37	3.48
487	12.74	537.48	-29.52	-231.16	4.97
488	12.76	557.57	-29.39	-230.47	4.62
489	12.78	572.64	-29.28	-229.63	4.58
490	12.8	582.69	-29.27	-230.38	3.76
491	12.82	391.81	-29.35	-230.95	3.82
492	12.84	492.27	-29.33	-231.33	3.29
493	12.86	492.27	-29.43	-232.04	3.37
494	12.88	487.25	-29.55	-233.53	2.83
495	12.9	547.53	-29.79	-235.10	3.26
496	12.92	507.34	-29.88	-236.04	3.03
497	12.94	452.09	-29.97	-236.83	2.96
498	12.96	607.81	-30.15	-238.04	3.17
499	12.98	577.67	-30.24	-238.65	3.28
500	13	512.37	-29.85	-240.06	-1.23
501	13.02	527.44	-30.39	-241.15	1.98
502	13.04	552.55	-30.17	-239.48	1.89
503	13.06	562.60	-30.22	-239.20	2.58
504	13.08	567.62	-30.15	-238.62	2.60
505	13.1	572.64	-30.04	-237.23	3.11
506	13.12	482.23	-30.03	-236.63	3.61
507	13.14	552.55	-30.02	-235.93	4.25
508	13.16	507.34	-29.88	-235.56	3.50
509	13.18	542.51	-30.10	-236.48	4.34
510	13.2	492.27	-30.02	-237.04	3.14
511	13.22	562.60	-30.09	-237.89	2.85
512	13.24	577.67	-30.13	-238.73	2.33
513	13.26	562.60	-30.19	-238.88	2.66
514	13.28	582.69	-30.12	-238.52	2.46
515	13.3	557.57	-29.90	-237.77	1.45
516	13.32	512.37	-29.89	-236.70	2.45
517	13.34	502.32	-29.97	-236.62	3.16
518	13.36	562.60	-29.70	-235.50	2.13
519	13.38	532.46	-29.26	-232.96	1.10
520	13.4	562.60	-29.35	-231.71	3.06
521	13.42	542.51	-29.09	-229.65	3.05
522	13.445	534.47	-28.88	-227.77	3.26
523	13.465	447.06	-28.61	-225.80	3.08
524	13.485	597.76	-28.67	-225.15	4.22

525	13.505	592.74	-28.44	-223.88	3.65
526	13.525	562.60	-28.33	-223.15	3.51
527	13.545	592.74	-28.26	-222.51	3.59
528	13.565	487.25	-28.31	-222.31	4.19
529	13.585	542.51	-28.53	-223.21	5.04
530	13.605	467.16	-28.46	-223.72	3.97
531	13.625	512.37	-28.06	-222.19	2.32
532	13.645	572.64	-28.40	-221.44	5.78
533	13.665	597.76	-28.47	-223.59	4.18
534	13.685	507.34	-28.53	-224.20	4.05
535	13.705	582.69	-28.62	-224.95	4.02
536	13.725	522.41	-28.70	-225.38	4.23
537	13.745	572.64	-28.79	-226.12	4.20
538	13.765	572.64	-28.78	-226.75	3.49
539	13.785	542.51	-28.77	-226.86	3.30
540	13.805	562.60	-28.84	-227.49	3.22
541	13.825	557.57	-28.89	-227.79	3.32
542	13.855	505.67	-28.84	-228.50	2.23
543	13.875	416.93	-28.73	-228.11	1.71
544	13.895	502.32	-28.91	-227.93	3.32
545	13.915	542.51	-28.87	-228.29	2.67
546	13.935	547.53	-28.83	-228.21	2.46
547	13.955	562.60	-28.99	-228.58	3.34
548	13.975	622.88	-29.15	-229.27	3.92
549	13.995	557.57	-29.18	-229.93	3.49
550	14.015	567.62	-29.30	-230.45	3.92
551	14.035	597.76	-29.29	-230.76	3.54
552	14.055	587.71	-29.47	-231.89	3.83
553	14.075	542.51	-29.60	-232.79	3.97
554	14.095	532.46	-29.60	-233.56	3.20
555	14.115	537.48	-29.69	-233.37	4.18
556	14.135	577.67	-29.76	-234.12	3.99
557	14.155	562.60	-29.90	-235.18	4.05
558	14.175	572.64	-29.95	-236.12	3.50
559	14.205	512.37	-29.96	-235.99	3.71
560	14.225	552.55	-30.00	-236.47	3.55
561	14.245	537.48	-29.92	-236.13	3.25
562	14.265	527.44	-29.83	-235.10	3.57
563	14.285	512.37	-29.92	-235.80	3.58
564	14.305	482.23	-29.87	-235.31	3.67
565	14.325	537.48	-29.69	-234.17	3.37
566	14.345	587.71	-29.83	-234.15	4.52
567	14.365	492.27	-29.86	-233.72	5.19
568	14.385	431.99	-29.86	-233.68	5.22

569	14.405	542.51	-29.84	-233.57	5.18
570	14.425	577.67	-29.91	-234.22	5.09
571	14.445	577.68	-29.93	-234.36	5.11
572	14.465	547.53	-30.19	-236.07	5.46
573	14.485	527.44	-30.27	-237.26	4.91
574	14.505	497.30	-30.46	-238.50	5.18
575	14.525	557.57	-30.47	-239.03	4.73
576	14.545	512.37	-30.53	-239.30	4.93
577	14.565	577.67	-30.25	-238.20	3.81
578	14.585	517.39	-30.19	-237.50	4.03
579	14.605	487.25	-29.92	-234.97	4.42
580	14.625	582.69	-29.53	-231.08	5.13
581	14.645	567.62	-29.34	-229.63	5.06
582	14.665	376.74	-29.11	-226.87	5.99
583	14.685	582.69	-28.79	-224.36	5.96
584	14.705	572.64	-28.76	-224.31	5.77
585	14.725	562.60	-28.40	-221.72	5.49
586	14.745	537.48	-28.17	-220.42	4.96
587	14.765	462.13	-27.74	-218.10	3.78
588	14.785	502.32	-28.01	-219.53	4.59
589	14.805	542.51	-27.84	-218.80	3.88
590	14.825	612.83	-27.76	-218.42	3.62
591	14.845	401.86	-27.76	-218.75	3.30
592	14.865	527.44	-27.65	-218.31	2.86
593	14.885	582.69	-27.44	-217.06	2.44
594	14.905	562.60	-27.57	-217.27	3.27
595	14.925	406.88	-27.56	-217.55	2.90
596	14.945	406.88	-27.60	-217.74	3.03
597	14.965	547.53	-27.51	-216.26	3.79
598	14.985	587.71	-27.93	-220.10	3.37
599	15.005	572.64	-27.92	-220.28	3.12
600	15.025	557.57	-28.07	-221.62	2.97
601	15.045	537.48	-28.27	-223.31	2.87
602	15.065	557.57	-28.50	-225.36	2.65
603	15.085	562.60	-28.71	-226.95	2.73
604	15.105	607.81	-28.89	-227.79	3.32
605	15.125	592.74	-29.12	-229.85	3.09
606	15.145	487.25	-29.24	-231.24	2.66
607	15.165	587.71	-29.45	-233.31	2.26
608	15.185	587.71	-29.60	-234.51	2.33
609	15.205	587.71	-29.70	-235.39	2.24
610	15.225	592.74	-29.80	-236.95	1.48
611	15.245	587.71	-29.88	-237.70	1.36
612	15.265	602.78	-29.84	-238.20	0.55

613	15.285	607.81	-29.80	-237.64	0.79
614	15.305	512.37	-29.62	-236.01	0.99
615	15.32	542.51	-29.52	-234.68	1.45
616	15.34	517.39	-29.23	-232.08	1.74
617	15.36	647.99	-29.14	-231.25	1.86
618	15.38	552.55	-29.03	-230.14	2.09
619	15.4	577.67	-28.57	-226.24	2.33
620	15.42	547.53	-28.09	-222.66	2.09
621	15.44	617.85	-27.72	-218.89	2.84
622	15.46	572.64	-28.17	-220.88	4.51
623	15.48	567.62	-27.94	-220.53	3.03
624	15.5	562.60	-27.94	-220.33	3.22
625	15.52	562.60	-27.92	-219.90	3.49
626	15.54	562.60	-27.99	-219.95	4.00
627	15.56	522.41	-28.02	-218.77	5.36
628	15.58	552.55	-27.79	-218.15	4.13
629	15.6	612.83	-27.87	-218.61	4.39
630	15.62	542.51	-27.86	-218.01	4.91
631	15.635	475.53	-27.85	-217.63	5.21
632	15.655	602.78	-27.82	-217.71	4.81
633	15.675	607.81	-27.71	-216.98	4.67
634	15.695	612.83	-27.81	-217.05	5.39
635	15.715	617.85	-27.45	-215.63	3.94
636	15.735	592.74	-27.79	-217.09	5.20
637	15.755	582.69	-27.85	-218.03	4.73
638	15.775	622.88	-27.78	-218.04	4.16
639	15.795	512.37	-27.89	-218.73	4.43
640	15.815	607.81	-28.02	-220.37	3.82
641	15.835	572.64	-27.92	-220.17	3.22
642	15.855	572.64	-27.58	-217.59	3.02
643	15.875	612.83	-27.46	-216.24	3.42
644	15.895	572.64	-27.22	-213.56	4.19
645	15.915	647.99	-26.90	-211.15	4.06
646	15.935	472.18	-26.28	-207.93	2.34
647	15.955	472.18	-26.46	-206.98	4.72
648	15.975	678.13	-26.29	-205.70	4.66
649	15.985	571.47	-26.16	-204.57	4.75
650	15.995	612.81	-25.94	-202.94	4.55